SAPP XXIII

23rd Symposium on Application of Plasma Processes

Book of Contributed Papers

Virtual Meeting
4th and 5th February, 2021

Edited by V. Medvecká, P. Papp, J. Országh, Š. Matejčík

Book of Contributed Papers: 23rd Symposium on Application of Plasma Processes, 4th and 5th February 2021.

Virtual meeting for PhD. and Master Students organised by Department of Experimental Physics, Faculty of Mathematics, Physics and Informatics, Comenius University in Bratislava and Society for Plasma Research and Applications.

Editors: V. Medvecká, P. Papp, J. Országh, Š. Matejčík

Publisher: Department of Experimental Physics, Faculty of Mathematics, Physics and Informatics, Comenius University in Bratislava; Society for Plasma Research and Applications in cooperation with Library and Publishing Centre CU, Bratislava, Slovakia

Issued: February 2021, Bratislava, first issue

ISBN: 978-80-8147-101-8

Number of pages: 93

URL: http://neon.dpp.fmph.uniba.sk/sapp/

Foreword

Dear SAPP participants, colleagues, friends,

For the first time in its 46-year long history the Symposium on Applications of Plasma Processes was held online without the possibility to meet personally. For the SAPP community it is a major setback since the spirit of SAPP is not only in excellent science but also in personal contact and in friendship spiced with leisure activities in beautiful nature. Thanks to SAPP many of us has built strong international network of colleagues supporting our scientific results and careers. Since we would like to broaden the community and offer similar experience to younger colleagues, we decided to assign all oral presentation slots to young scientists. Another reason was their need to present the work in situation when due to the world-wide COVID-19 pandemic many conferences and meetings are postponed or cancelled. On the other hand, this crisis pushed us in exploring new possibilities. Thanks to modern technology and internet accessibility around the world it was possible to organize such a nice event even though travelling is very limited. It also made SAPP accessible to participants who would not be able to attend even if there were no travel restrictions. We believe this experience will guide us to organizing partially hybrid meetings in the future which will join the good of both worlds. They will provide the personal contact that we miss so much to majority and allow somewhat limited participation to those who are unable to travel due to various reasons.

With such a positive outlook we would like to express our gratitude to all of you for the participation and we are looking forward to meeting you in the future.

SAPP XXIII LOC

Local Organizers

Department of Experimental Physics
Faculty of Mathematics, Physics and Informatics
Comenius University in Bratislava
Mlynská dolina F2
842 48 Bratislava, Slovakia
URL: http://www.fmph.uniba.sk/
Tel.: +421 2 602 95 686
Fax: +421 2 654 29 980

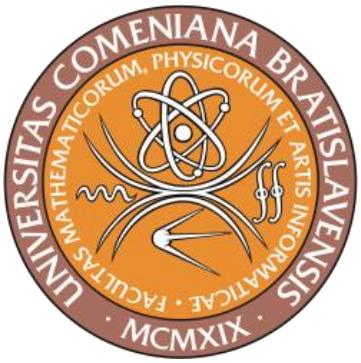

Society for plasma research and applications
Faculty of Mathematics, Physics and Informatics
Comenius University Bratislava
Mlynská dolina F2
842 48 Bratislava, Slovakia
E-mail: spvap@neon.dpp.fmph.uniba.sk
Tel.: +421 2 602 95 686

SPVAP

Local Organizing Committee

Štefan Matejčík (chair)
Peter Papp
Juraj Országh
Veronika Medvecká

International Scientific Committee

23rd Symposium on Application of Plasma Processes

Prof. J. Benedikt	Christian-Albrechts-University, Kiel, Germany
Dr. R. Brandenburg	INP, Greifswald, Germany
Dr. Z. Donkó	Hungarian Academy of Sciences, Budapest, Hungary
Dr. T. Field	Queen's University, Belfast, United Kingdom
Prof. S. Hamaguchi	Osaka University, Japan
Prof. F. Krčma	Brno University of Technology, Brno, Czech Republic
Prof. N. Mason	University of Kent, United Kingdom
Prof. Š. Matejčík	Comenius University in Bratislava, Slovakia
Prof. J. Pawlat	University of Technology, Lublin, Poland
Prof. M. Radmilović-Radjenović	Institute of Physics, Belgrade, Serbia
Prof. P. Scheier	Leopold-Franzens University, Innsbruck, Austria

Reading Committee

Dr. Z. Donkó	Hungarian Academy of Sciences, Budapest, Hungary
Dr. T. Field	Queen's University, Belfast, United Kingdom
Prof. F. Krčma	Brno University of Technology, Brno, Czech Republic
Prof. Š. Matejčík	Comenius University in Bratislava, Slovakia
Prof. M. Radmilović-Radjenović	Institute of Physics, Belgrade, Serbia

Content

Chairman of the session: Zoltán Donkó

AN EFFICIENT GPU IMPLEMENTATION OF A 1D PARTICLE-IN-CELL/MONTE CARLO COLLISIONS METHOD FOR MODELLING RADIO-FREQUENCY DISCHARGES

Ján Ďurian[1], Štefan Matejčík[1], Zoltán Donkó[2], Peter Hartmann[2]

[1]*Department of Experimental Physics, Faculty of Mathematics, Physics and Informatics, Comenius University in Bratislava, Slovakia*
[2]*Wigner Research Centre for Physics, Budapest, Hungary*

E-mail: durian5@uniba.sk

We present a new OpenCL-based GPU implementation of the one-dimensional Particle-in-Cell/Monte Carlo Collisions (PIC/MCC) method for simulations of capacitively coupled plasmas. We adapted the method to fully utilize the GPU parallelism, achieving significant speedups of up to 37x compared to classic CPU implementations. The accuracy of the code was tested with a set of four benchmarks. The results show that our code is accurate, proving that GPUs are a valuable asset in PIC/MCC modelling of plasmas.

1. Introduction

Particle-in-Cell represents a family of numerical methods which separates modelling of the time-evolution of plasma into two separate steps. In the first step we trace individual particles in a continuous phase space, while in the second step we evaluate particle distribution and electric fields on a discrete, static mesh, also referred to as the grid [1]. In order to make them able to describe collisional plasmas, these methods were later extended with a Monte Carlo Collisions model, forming what is now known as Particle-in-Cell/Monte Carlo Collisions (PIC/MCC) approach [2] [3].

Since we're tracking every individual particle[1] in phase space, PIC/MCC models require vast computing resources. This prompts extensive research for optimizing the implementations of PIC/MCC models, as well as using specialized hardware such as the General-Purpose Graphics Processing Units (GPGPU; referred to as GPU in this paper) which excel in parallel computing.

The PIC/MCC method traditionally consists of six fundamental components connected in the main simulation loop (see figure 1):

- **Assign particle charges to grid points** – computing the particle distributions on the static grid by interpolating their positions.
- **Solve the Poisson equation** – solving for electric potential created by the electrodes and the particles and finding the electric field.
- **Compute particle forces from the electric field** – computing the forces exerted on the particles by interpolating of the electric field onto the particles.
- **Move particles in space** – moving the particles in the electric field formed by outside electrodes and the particles themselves.
- **Add/Remove particles at boundaries** – removing particles that left the simulation boundaries, and adding new ones if effects like the secondary emission are present.
- **Execute collisions, add/remove particles** – modelling plasma kinetics with elastic and excitation, as well ionization collisions utilizing Monte Carlo methods, which rely on random number generation.

[1] Superparticles in PIC/MCC

In this paper, we present an efficient GPU implementation of a one-dimensional PIC/MCC model based on the OpenCL 2.0 platform. First, we will briefly discuss our parallelization strategy for each of the basic PIC components. Then, we'll take a closer look at the Poisson solver on the GPU. Finally, we'll present four benchmark simulations and analyze the numerical as well as the performance results we've obtained with our code.

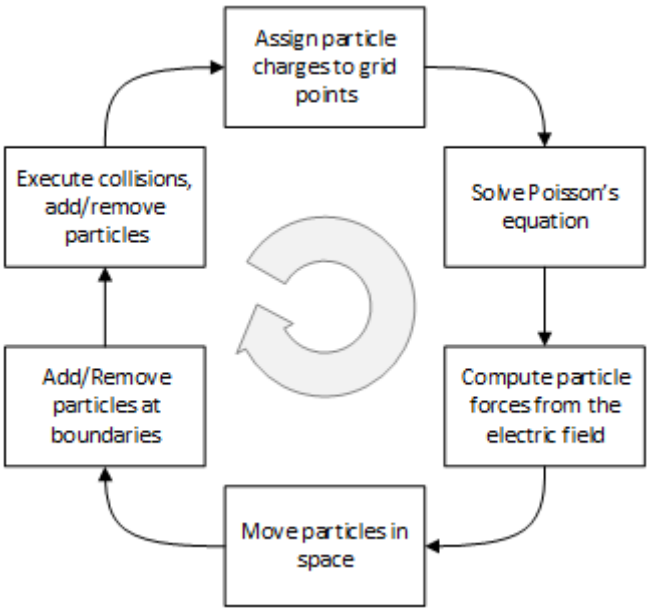

Figure 1 - The basic PIC/MCC cycle

2. Parallelization strategy for our PIC/MCC GPU implementation

GPUs are massively parallel hardware, that is, they're capable of executing thousands of threads in parallel at one time. For parallelization purposes, it is best if the threads each access their own set of data without colliding with other threads. Knowing this, it is needed to find a way to split the workload contained in PIC/MCC sufficiently to utilize the GPU's vast computing resources.

As we already mentioned, in PIC/MCC we track the motion of every particle. Since at the time of moving the particles don't interact with each other, we're able to map one thread to process one particle in the simulation while the threads access only data related to their assigned particle. In our code, we used exactly this approach. In typical 1D PIC/MCC simulations there's between 100 to 500 thousand particles per species present, which provides sufficient parallelism for GPU hardware.

Issues arise with the particle-to-grid interpolations. Thousands of threads are processing particles, while there's only one computational grid with up to 512 grid points to which the particle densities are interpolated. Multiple threads therefore access the same grid data, and their access must be serialized using atomic operations. This creates a performance bottleneck; however, the GPU memory is fast enough to be able to hide this latency at least partially.

Most of the fundamental components of the PIC/MCC method is executed directly on the particles. This allowed us to effectively combine the basic components of the main simulation loop in our GPU implementation into merely three steps – (i) advancing the particles (computing forces, moving, colliding particles and interpolating the density distribution), (ii) solving the Poisson equation to obtain the electric potential and (iii) computing the new electric field.

To reduce the memory overhead, we perform particle removal at the boundaries only once per a couple hundred time steps. To determine which particles are inactive we use a bookkeeping system. If a particle leaves the simulation boundaries, its "inactive" flag is raised, marking it for removal at the next particle removal operation.

In the following section we'll discuss our implementations of a 1D Poisson solver on GPUs.

3. 1D Poisson solver on GPU

One of the outstanding issues of developing a 1D PIC/MCC code that runs entirely on the GPU is solving the one-dimensional Poisson equation in an efficient way. Classic CPU implementations use the efficient Thomas algorithm with a numerical complexity of O(n) [4] [5]. However, the Thomas algorithm is inherently serial, which makes it unsuitable for parallel hardware like GPUs. That's why we looked for a different approach in our GPU implementation.

The Poisson equation is given as

$$\Delta\varphi = -\frac{\rho}{\varepsilon_0} \tag{1}$$

where φ is the electric potential, ρ is the electric charge distribution in phase space and ε_0 is the permittivity of vacuum. Transforming (1) into the Discrete Poisson Equation

$$\frac{-\varphi_{j-1} + 2\varphi_j - \varphi_{j+1}}{\Delta x^2} = -\frac{\rho_j}{\varepsilon_0} \tag{2}$$

we're able to obtain the solution by solving a set of linear equations which can be collectively written in the matrix form

$$A_{ij}\varphi_j = -\frac{\rho_j}{\varepsilon_0} \tag{3}$$

where A is the tridiagonal symmetric matrix of the system, and ρ_j is the charge density at the j-th grid point. The solution is obtained by inverting the coefficient matrix A:

$$\varphi_j = -A_{ij}^{-1}\frac{\rho_j}{\varepsilon_0} \tag{4}$$

This allows us to solve the Poisson equation using a matrix-vector multiplication operation, which has many efficient implementations on GPUs. Moreover, the inverse matrix A^{-1} is constant, therefore we only need to precompute it once at the start of the simulation using

$$A_{ij}^{-1} = B_{ij} = \begin{cases} -\dfrac{(j+1)(N-j)}{N-1} \\ B_{ji} \end{cases} \tag{5}$$

Boundary conditions are the time-dependent potentials imposed by the electrodes of the system.

4. Benchmark simulations and results

To validate our GPU implementation of PIC/MCC we used a set of four benchmark cases modelling low-pressure radio-frequency (RF) discharges in Helium, first published by Turner et al. [6]. These cases model a system with plane-parallel electrodes connected to a RF source, which drives the plasma with a sinusoidal waveform with a given frequency and amplitude. All physical and numerical parameters are listed in Table 1.

Our model assumes electron-neutral and ion-neutral collisions. Electron-neutral collisions are modelled using a set of cross-sections known as Biagi 7.1 [7], which consists of cross sections for (i) elastic momentum transfer, (ii) singlet excitation, (iii) triplet excitation and (iv) ionization. We assume isotropic scattering in all types of processes. Ion-neutral collisions are modelled using cross-sections proposed by Phelps [8], which approximates anisotropic scattering using an isotropic scattering component complemented by a backscattering component, both in the center-of-mass frame. Therefore, in total our model assumes 4 electron-neutral, and 2 ion-neutral collision types.

		Case			
		1	2	3	4
Physical parameters:					
Electrode distance	$L\ [cm]$	6,7	6,7	6,7	6,7
Gas pressure	$p\ [Pa]$	4	13,33	40	133,3
Gas temperature	$T\ [K]$	300	300	300	300
Voltage amplitude	$V\ [V]$	450	200	150	120
Voltage frequency	$f\ [MHz]$	13,56	13,56	13,56	13,56
Numerical parameters:					
Number of grid points	N	128	256	512	512
Time steps per RF cycle	N_t	400	800	1600	3200
Total steps computed	N_s	512 000	4 096 000	8 192 000	49 152 000
Particle weight factor	W	26 172	52 344	52 344	78 515
Target convergence parameters:					
Number of electrons	Ne	12 300	57 000	138 700	161 600
Number of ions	Ni	19 300	60 200	142 300	164 500
Peak ion density	$n_i[10^{15}\ m^3]$	0,14	0,828	1,81	2,57

Table 1 - Benchmark parameters

The results of our simulation are shown in Figure 2. Here, we compared the time-averaged ion density distribution with those provided with the benchmark [6]. Our results show a good match in the shape of the final distributions, although our peak values differ slightly especially in cases 2 and 3, as detailed in Table 2.

	Peak ion density [10^{15} m^{-3}]		
Case	Our code	Benchmark	Diff.
1	0.140	0.140	0.0%
2	0.850	0.828	+2.7%
3	1.83	1.81	+1.1%
4	2.58	2.57	+0.4%

Table 2 - Comparison of peak ion densities as computed by our code and the benchmark

However, small differences in the results among different implementations are to be expected, especially the GPU-based ones. The source of these differences comes down to details like the precision of the floating-point numbers used in the code itself. We have seen the accuracy improve slightly by using double-precision floating-point numbers for collision evaluation and the field solver. However, GPUs are optimized for single-precision operations, and using single-precision floating-point numbers wherever possible is crucial for good performance in GPU-based implementations of PIC/MCC. The speed gained at the slight loss of accuracy is an acceptable trade-off.

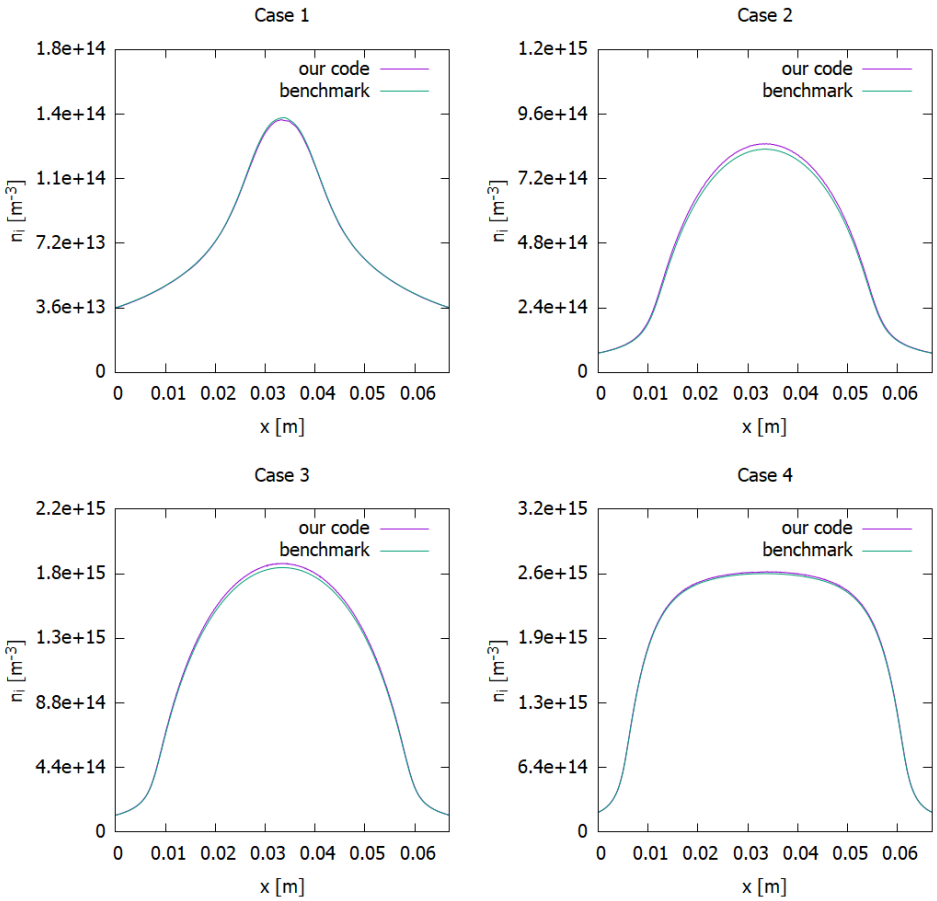

Figure 2 - Comparison of ion density distribution with the benchmarks.

5. Performance results

We performed the benchmarks on two different GPUs supporting OpenCL 2.0; AMD Radeon Pro WX 9100 and AMD Radeon VII. We measured the execution time per 100 RF voltage cycles as well as the total execution time required for the particle counts to converge to a steady state.

Case	WX 9100	Radeon VII
1	3.12s	1.83s
2	10.54s	6.16s
3	41.94s	25.89s
4	88.11s	50.80s

Case	WX 9100	Radeon VII
1	39s	23s
2	8m 59s	5m 15s
3	35m 48s	22m 6s
4	6h 8m	3h 32m

Table 3 - Performance measurements of our code on the AMD Radeon Pro WX 9100 and AMD Radeon VII GPUs. (Left) Execution time per 100 RF cycles; (Right) Execution time until particle count convergence.

Case	CPU time	Speedup
1	18.7s	6x - 10x
2	131.9s	12x - 21x
3	700.4s	16x - 27x
4	1902s	21x - 37x

Table 4 - Speedup achieved with our GPU code as compared with Xeon Scalable Gold 6132 from the benchmarks. The lower range of the speedup is for the Radeon Pro WX 9100, the upper range is for the Radeon VII.

On both GPUs we achieved a substantial performance improvement compared to the CPU performance from the benchmarks, with the speedups ranging from 6x for Case 1 to 37x for Case 4. These results show that GPUs are more efficient with larger-scale simulations, as the higher particle counts allow us to better exploit the GPU's parallelism.

6. Conclusion

In this paper we presented a new GPU-accelerated PIC/MCC code based on the OpenCL 2.0 platform. We discussed the parallelization strategy employed in our code, as well as a way to efficiently solve the one-dimensional Poisson equation as a tridiagonal system on the GPU. We verified the accuracy of our code by benchmarking it against a set of four simulation cases specified by Turner et al. [6], and we discussed the simulation and performance results we've obtained.

We found that our results are in a good match with the benchmarks, with some minor differences. These differences come down to details such as using single-precision or double-precision floating-point numbers in the code. In our code, we opted for using single-precision numbers wherever possible to maximize the performance of the code on GPUs.

With our new code we achieved significant performance speedups compared to CPU execution times, ranging from 6x for smaller-scale simulations to 37x for larger-scale simulations. Our results show that GPUs perform more efficiently with higher particle counts, as that allows for better utilization of the parallel nature of the GPU hardware. This allows us to obtain accurate results within minutes to hours of time, making modelling of capacitively coupled plasmas much more time and cost efficient with GPU implementations of the PIC/MCC method.

7. Acknowledgments

This work was supported by the Slovak Research and Development Agency. Project No.APVV-19-0386. Financing of this work was by the Slovak Grant Agency VEGA1/0733/17. This project has received funding from the European Union's Horizon 2020 research and innovation programme under grant agreement No 692335.

8. References

[1] Y. N. Grigoryev, V. A. Vshivkov and M. P. Fedoruk, Numerical "Particle-in-Cell" Methods, Utrecht: VSP BV, 2002.

[2] C. K. Birdsall, "Particle-in-Cell charged-particle simulations, plus Monte Carlo collisions with neutral atoms, PIC-MCC," *IEEE Transactions on Plasma Science*, vol. 19, no. 2, pp. 65-84, 1991.

[3] V. Vahedi and M. Surendra, "A Monte Carlo collision model for particle-in-cell method: applications to argon and oxygen discharges," *Computer Physics Communications*, vol. 87, no. 1-2, pp. 179-198, 1995.

[4] G. Lapenta, "Kinetic Plasma Simulation: Particle In Cell Method," in *XII Carolus Magnus Summer School in Plasma and Fusion Energy Physics*, Leuven, 2015.

[5] W. Hong-Yu, S. Peng, J. Wei, Z. Jie and X. Bai-Song, "Implicit electrostatic particle-in-cell/Monte Carlo simulation for the magnetized plasma: Algorithms and application in gas-inductive breakdown," *Chinese Physics B*, no. 24, 2015.

[6] M. M. Turner, A. Derzsi, Z. Donkó, D. Eremin, S. J. Kelly, T. Lafleur and T. Mussenbrock, "Simulation benchmarks for low-pressure plasmas," *Phys. Plasmas*, vol. 20, no. 1, pp. 1-11, 2013.

[7] S. F. Biagi, "Cross Section Compilation, version 7.1, 2004," [Online]. Available: http://www.lxcat.net.

[8] A. V. Phelps, *J. Appl. Phys.*, vol. 76, p. 747, 1994.

MOLECULAR DYNAMICS STUDY OF ION SCATTERING ON SILICON AND SILICON DIOXIDE

Charisse Marie D. Cagomoc[1], Michiro Isobe[1],
Eric A. Hudson[2], Satoshi Hamaguchi[1]

[1] *Center for Atomic and Molecular Technologies, Osaka University*
[2] *Lam Research Corporation*
E-mail: cagomoc@ppl.eng.osaka-u.ac.jp

Scattering properties of energetic ions on smooth and rough silicon and silicon dioxide surfaces were studied through molecular dynamics simulation. In general, specular polar scattering of the ions occur with minimal azimuthal deflection. Effects of surface roughness on the scattering probability become weak as the incident ion energy increases.

1. Introduction and Methodology

Research and development of nano-scale semiconductor devices with higher integration have been continuously pursued to address the demand for high-speed information processing and communication in the modern society. To support this, a mechanistic understanding and control of plasma etch processes are required, including the interaction of energetic ions with material surfaces. In this study, being motivated to understand the scattering properties of energetic ions at a vertical material wall, we performed molecular dynamics simulation of scattering of neon, argon, and xenon ions on smooth or rough silicon and silicon dioxide surfaces at glancing incident angles. In the simulation, a roughened surface was realized by creating 1nm protrusions on the surface. The ions were injected with 100eV and 1000eV energies at several incident angles. Periodic boundaries were applied in the horizontal direction. The surface was returned to its initial state after every impact.

2. Results and Discussion

The simulation showed that the polar scattering for all impact ions was highly specular, especially at 85˚ for a smooth surface. For a rough surface, specular reflection was still observed though the polar scattering angle distribution was broader compared to that for the smooth surface. For both smooth and rough surfaces, the azimuthal scattering angle peaked at 0˚, i.e. no deflection, and its distribution broadened with the decreasing incident angle. Fig. 1 compares the reflection probability vs. incident angle for smooth vs. rough silicon. At 1000eV, the reflection probability for all ions at 70˚ incident angle was the same for both smooth and rough surfaces. At 80˚ and 85˚incident angles, reflection probability was higher for a smooth surface. The reflection probabilities of injected ions with 100eV and 1000eV for smooth Si were also compared. It was observed that, at 100eV, nearly all ions were reflected at specular polar scattering angles and minimal azimuthal deflection. At such low energy and a glancing incident angle, interaction between the impact ions and the substrate occurs mainly at the top 1 or 2 surface atomic layers.

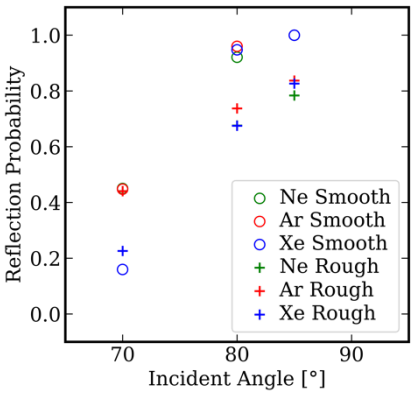

Fig. 1. Reflection probabilities of Ne, Ar, and Xe on smooth and rough silicon as function of the angle of incidence

Acknowledgements

One of the authors (CMDC) would like to acknowledge the Japan Society for the Promotion of Science (JSPS) Fellowship for the partial support of this study. The work was also supported partially by a grant of Lam Research Corp., JSPS Grant-in-Aid for Scientific Research(S) 15H05736, and Core-to-Core Program JPJSCCA2019002.

EXPERIMENTAL AND MODELING STUDY OF SURFACE REACTIONS OF PLASMA GENERATED ATOMIC OXYGEN WITH PHENOL SOLUTIONS

Kerstin Sgonina[1], Giuliana Bruno[2], Kristian Wende[2], and Jan Benedikt[1]

[1]*Institute of Experimental and Applied Physics, Kiel University, Kiel, Germany*
[2]*Leibniz Institute for Plasma Science and Technology, Greifswald, Germany*
E-mail: sgonina@physik.uni-kiel.de

The interaction of plasma generated atomic oxygen with phenol solution is studied experimentally using an atmospheric pressure plasma jet (COST-Jet). With varied gas admixtures of He/O_2 the amount of produced atomic oxygen leaving the plasma source and its recombination lifetime with O_2 are controlled at the same time. The use of different phenol concentrations allows a change of surface reaction probability to investigate the importance of surface reactions on liquid for atomic oxygen. A developed transport and reaction simulation of the experimental setup supports the findings and provides insight into the details of the reaction processes.

In recent decades plasma treated liquid became a relevant topic for various fields due to its high reactivity with biological substrates or organic compounds [1]. This increased reactivity is induced by reactive species like atomic oxygen or hydroxyl radicals. However, as the lifetime of atomic oxygen is short, knowledge about its reactions with dissolved species in aqueous solutions is limited. For example, it is not known whether the reactions occur dominantly at the liquid surface or in the liquid bulk. As the density of atomic oxygen leaving the COST-Jet is well known [2,3], this source suits well the investigations of ongoing oxygen reactions. Furthermore, it was proven in previous studies that phenol reacts directly with atomic oxygen without any intermediate reactions with or in water [4,5]. With phenol being a surfactant, a variation of phenol concentration between 0.1 and 25 mM changes the surface reaction probability of atomic oxygen with it. To reveal the reaction process, the consumption of phenol and the production of diols and triols are studied using mass spectrometry (MS) and high-performance liquid chromatography (HPLC).

To investigate the reaction rates at liquid surface or in its bulk and to support the experimental results, a 2D axisymmetric model has been developed in COMSOL Multiphysics without the necessity of simulating the plasma itself, as the densities of reacting species are well known from experiments [2,3]. A fluid dynamic simulation is performed to render the gas stream impinging on liquid surface and induced stirring of the liquid. After that, transport and reaction rate equations are solved for phenol, O, O_2 and O_3 species. Several values which are not reported in the literature, like the Henry's solubility law constant of atomic oxygen or surface reaction rate of atomic oxygen with phenol, were fitted and varied in this model. The implementation of surface coverage of surfactants and surface reactions on the liquid surface allow studying important reaction probabilities of atomic oxygen.

The results of the experimental and modeling studies show a good agreement (fig. 1). It is found that the reactions of atomic oxygen at the liquid surface are the key player of the degradation process of phenol molecules and therefore also for other surfactant molecules (fig. 2).

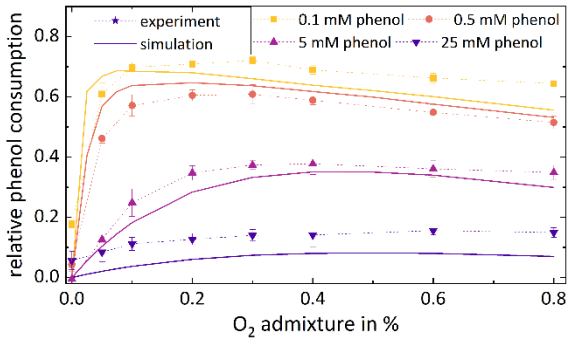

Fig. 1. Phenol consumption relative to initial phenol concentration varying between 0.1 and 25 mM for different O_2 admixtures. Comparison of experimental and modeling results.

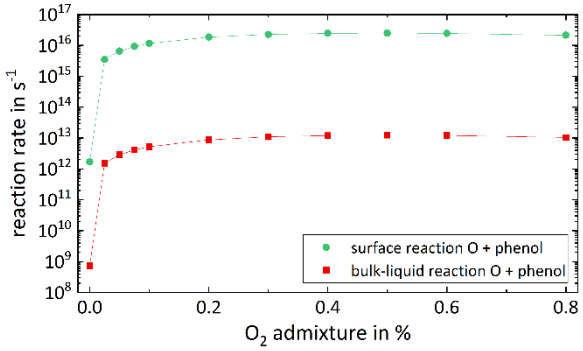

Fig. 2. Calculated reaction rates per second of atomic oxygen in 25 mM phenol solution at the liquid surface and in bulk-liquid depending on different O_2 admixtures in He/O_2 plasma.

The results of the simulation clearly show that most of the atomic oxygen reactions with phenol take place at the liquid surface, mainly due to the low value of Henry's solubility law constant of atomic oxygen and the surfactant character of phenol molecules. This study is relevant for atomic oxygen reactions with other species as well, for example the reaction with Cl^- anions in PBS or in saline solution to form ClO^-, because they are very probably also taking place dominantly at the surface of the liquid. The knowledge provided in this work has important implications for further development of plasma-liquid treatments involving atomic oxygen as reactant.

1. References

[1] S. Bekeschus et al., *Scientific Reports*, 7, 2791 (2017).
[2] D. Ellerweg et al., *New Journal of Physics*, 12, 013021 (2010).
[3] G. Willems et al., *New Journal of Physics*, 21, 059501 (2019).
[4] M. Mokhtar Hefny et al., *J. Phys. D: Appl. Phys*, 49, 404002 (2016).
[5] J. Benedikt et al., *Phys. Chem. Chem. Phys.*, 20, 12037 (2018).

THE ROLE OF ELECTRON-INDUCED SECONDARY ELECTRONS IN LOW-PRESSURE CAPACITIVELY COUPLED OXYGEN PLASMAS

B. Horváth[1,2], A. Derzsi[1], Z. Donkó[1], J. Schulze[3,4]

[1]*Wigner Research Centre for Physics, Budapest, Hungary*
[2]*Eötvös Loránd University, Budapest, Hungary*
[3]*Ruhr-University Bochum, Bochum, Germany*
[4]*Dalian University of Technology, Dalian, People's Republic of China*
E-mail: horvath.benedek@wigner.hu

The role of the electron-surface processes in single-frequency (13.56 MHz) capacitively coupled oxygen discharges is studied in the low-pressure regime (< 1 Pa) by particle based simulations. Two different models are used to describe the interaction of electrons with the electrodes: (i) a simple one assuming only elastic reflection of the electrons with a constant probability of 0.2 (model A) and (ii) a realistic one which takes elastic reflection, inelastic reflection and secondary electron emission into account as a function of the energy and angle of incidence of the electrons (model B). It is found that electron-induced secondary electrons remarkably increase the plasma density and the $O_2(a^1\Delta_g)$ metastable concentration, and consequently decrease the electronegativity of the discharge.

1. Introduction

Capacitively coupled plasmas (CCPs) operated in electronegative gases, such as oxygen, have been widely used in plasma-based surface treatment applications, such as etching, deposition and biomedicine [1–4]. In these applications, the interaction of the charged heavy particle species with the electrodes plays an important role. In order to optimize the flux and the energy of the particles colliding with the electrodes, a scientific approach is beneficial to understand the complex physics of the plasma. For example, understanding the electron power absorption dynamics [5] and the effects of surface processes on the plasma have become a central issue [6-7]. This work focuses on the latter phenomenon by conducting Particle-in-Cell/Monte Carlo Collisions (PIC/MCC) simulations of CCPs. In such simulations, several simplifications are common regarding the plasma-surface interactions. In the description of the interaction of electrons with boundary surfaces, the most wide-spread simplifications are the following: (i) the electron reflection is completely neglected, or a constant value (typically 0.2 [8]) for the electron reflection coefficient is assumed, irrespectively of the discharge conditions; (ii) the secondary electron emission (SEE) due to electron impact is not taken into account, and (iii) the effects of the electrode material and surface conditions on these processes are not accounted for. In a recent study, a realistic semi-empirical model has been introduced for the interaction of the electrons with the electrodes [9] and used for CCPs operated in argon [9–13]. In the current work, the same model is applied for oxygen discharges, that are relevant for surface treatment applications.

2. Simulation model and discharge conditions

The calculations are performed with our PIC/MCC code developed for oxygen [14], which is one-dimensional in space and three-dimensional in velocity space. The species that are followed in the particle dynamics are O_2^+ and O^- ions and electrons. The model considers 22 elementary collision processes involving these particles and $O_2(a^1\Delta_g)$ metastables (for details see [14]). The motion of the metastable molecules is not followed in the simulation: they are assumed to have a homogeneous density profile between the two electrodes, and their concentration is determined based on a balance equation, in which their source is the metastable excitation reaction, and the losses are the associative detachment and the quenching at the electrodes, which was set to be $6 \cdot 10^{-3}$/s [14]. The electrodes are plane, parallel and infinite, resulting in a geometrically symmetric discharge. The electrode separation is $L = 6.7$ cm, and both electrodes are assumed to be made of SiO_2 with the same surface conditions, hence they are characterized by the same electron emission and particle reflection properties. The temperature

of the oxygen gas is assumed to be 400 K. One of the electrodes is grounded, while the other one is driven by a single-frequency sinusoidal waveform:

$$V(t) = V_0 cos(2\pi f t). \quad (1)$$

The value of the frequency is $f = 13.56$ MHz in all cases, and the driving voltage amplitude is varied between 500 V and 1500 V, while the gas pressure is between 0.5 Pa and 1 Pa.

In order to study the role of the interaction of the electrons with the electrodes in the discharge, we compare the simulation results obtained by a simple (A) and a realistic (B) model:

- *Model A* assumes that the electrons hitting the electrode surface are elastically reflected with a constant probability of 0.2 [8], independently on their energy and angle of incidence.
- *Model B* is a realistic description of the electron-surface interaction. It assumes that the total SE yield (σ) consists of three components: elastically reflected primary electrons (PEs), inelastically reflected PEs and electron-induced SEs (true SEs, δ-electrons):
  $$\sigma = \eta_e + \eta_i + \delta, \quad (2)$$
  where η_e is the elastic reflection yield, η_i is the inelastic backscattering yield and δ is the electron-induced SEE yield. The characteristics of the surface are taken into account via material specific input parameters, such as the maximum emission at normal incidence, the energy of the PE at maximum emission etc. A detailed description of this approach is given in [9]. The model parameters are set to reflect the properties of a SiO_2 surface.

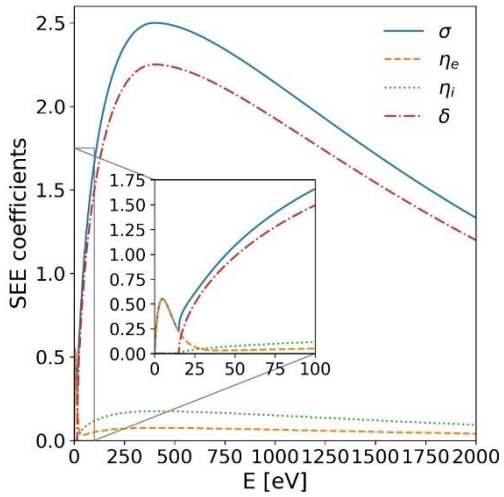

Fig. 1. The total electron-induced secondary electron emission coefficient (σ) and the partial emission coefficients of the elastic reflection (η_e), inelastic backscattering (η_i), and electron-induced secondary electron emission (δ) as a function of the incident electron energy, ε, at normal incidence for SiO_2 surfaces [9].

The total and partial electron emission coefficients for SiO_2 surfaces are shown in figure 1, at normal incidence. For the ion-induced SEE coefficient, a constant value of $\gamma = 0.4$ is used in the simulations. (Since our main goal was to study the effects of electron-induced SEs, a simple model for the ion-induced SEE was used.)

3. Results

A comparison of the charged particle densities at the center of the discharge obtained based on the simple and the realistic model is shown in figure 2. As the driving voltage amplitude is increased from 500 V to 1500 V at 0.7 Pa, the charge densities remarkably increase for model B, while their increase is much less pronounced for model A. The O_2^+ ion density increases approximately by a factor of 1.5 in case of model A, while an increase above a factor of 2 is observed by model B.

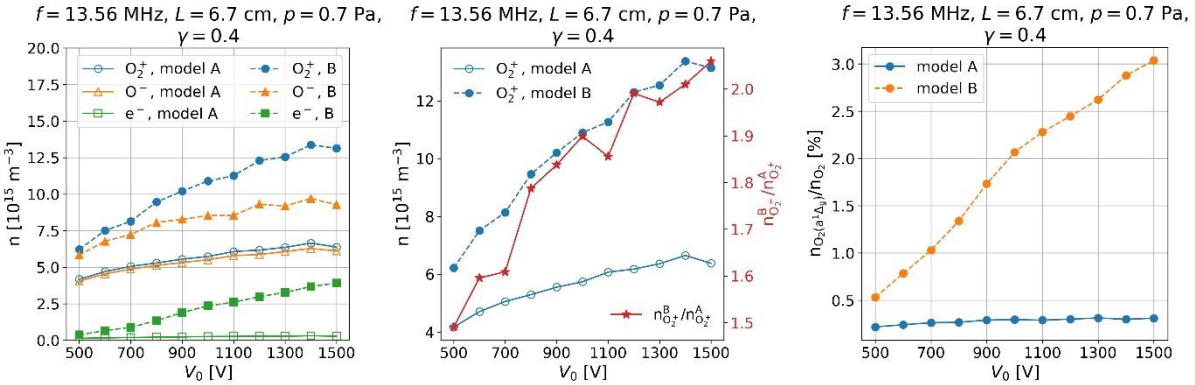

Fig. 2. The charged particle densities at the center of the discharge obtained from model A (open symbols) and model B (filled symbols), respectively (left panel); the O_2^+ ion densities and the ratio of the O_2^+ densities obtained from model A and B (center panel); and the density ratio of $O_2(a^1\Delta_g)$ metastables (right panel), as a function of the driving voltage amplitude, at a pressure of 0.7 Pa.

The electron density hardly changes when the simple model is used, while it increases by almost an order of magnitude, if the realistic model is used, which includes electron-induced secondary electron emission. Meanwhile, at the highest voltage amplitude, a more than twice higher O_2^+ density is obtained for model B compared to model A (see the center panel). The reason behind this remarkable increase of the density at higher voltages is electron-induced secondary electron emission, which becomes more efficient at higher incident electron energies. In the right panel of figure 2, the density ratio of $O_2(a^1\Delta_g)$ metastables compared to neutral O_2 is shown. The ratio increases with the voltage amplitude for model B, because of the increased number of electrons that can cause metastable excitation. The rate of metastable loss by associative detachment is orders of magnitude lower than the source channel, for all cases investigated. The electronegativity at the center of the discharge is shown in figure 3. As the voltage amplitude is increased from 500 V to 1500 V at 0.7 Pa, the electronegativity decreases for both models. However, while the decrease is linear in case of model A, it is found to be exponential for model B, if electron-induced secondary electrons are present. Moreover, the electronegativity is remarkably lower for model B than for model A. This is the consequence of the increased number of electrons in the discharge, and the tendency of increasing electron density in case of model B. The increased electron density also has an indirect effect that decreases the electronegativity: as the metastable concentration is increased because of the increased number of electrons that create them by excitation, the associative detachment rate (i.e. the destruction of O^- ions in collisions with metastable molecules) increases, which is an important loss channel of negative ions.

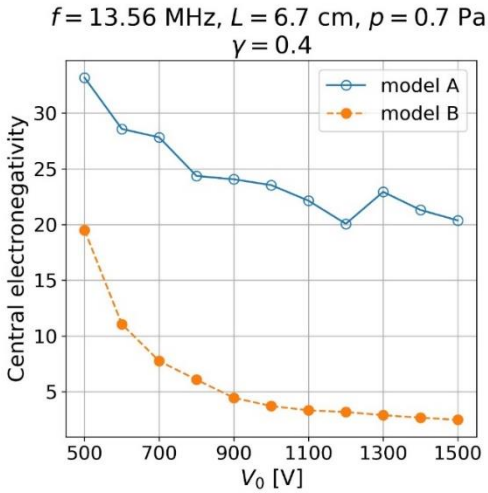

Fig. 3. The central electronegativity obtained by the simple and the realistic model, model A and B, respectively, as a function of the driving voltage amplitude, at a pressure of 0.7 Pa.

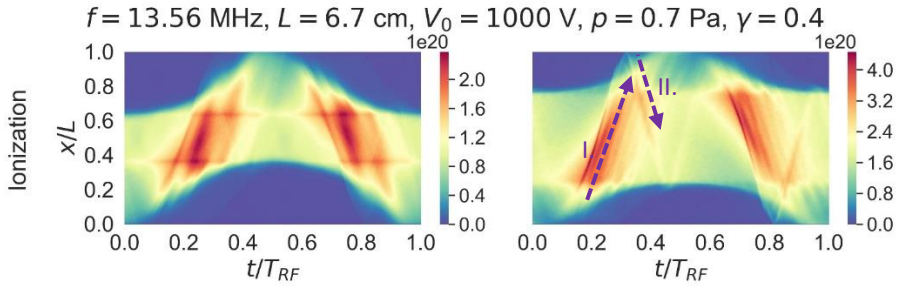

Fig. 4. The spatio-temporal distribution of the ionization rate [$m^{-3}s^{-1}$] obtained for model A (left) and model B (right), at a pressure of 0.7 Pa and driving voltage amplitude of 1000 V.

Figure 4 shows a comparison of the ionization dynamics obtained for model A and model B, for a selected case in the middle of the studied parameter regime: for a pressure of 0.7 Pa and a driving voltage amplitude of 1000 V. In case of model A (left panel), drift-ambipolar discharge operation mode can be observed, while model B exhibits α-mode with additional ionization caused by secondary electrons: a second ionizing beam (II. in the figure) departs upon arrival of the α-beam (I. in the figure) at the phase of partial sheath collapse, which is highly accelerated by the residual sheath potential. It is found that this beam (II.) mostly consists of secondary electrons emitted from the electrode, induced by ions and electrons. Moreover, it is also found that electron-induced secondary electrons (δ-electrons) directly contribute approximately 50% of the ionization processes. This way δ-electrons cause a dramatic increase in the electron density, which leads to the increase of the metastable density and the decrease of the electronegativity.

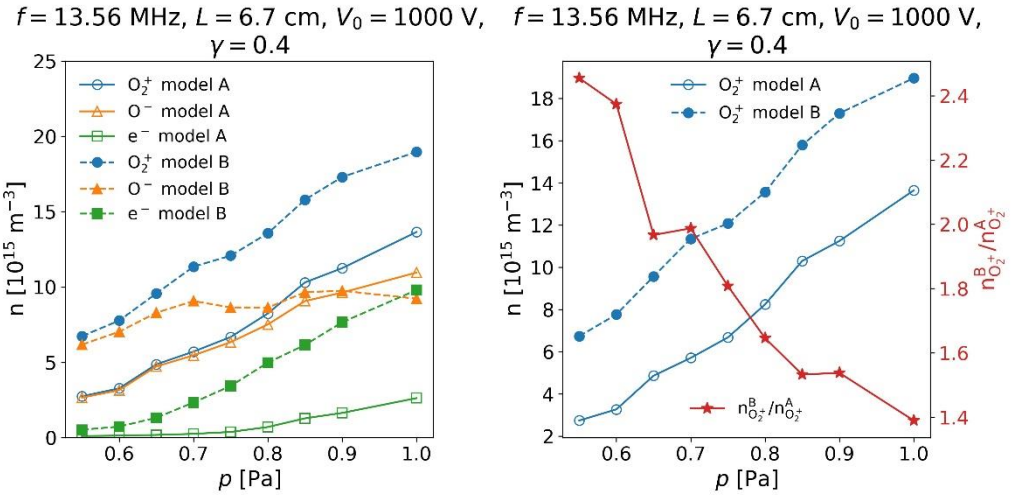

Fig. 5. The charged particle densities at the center of the discharge obtained for model A (open symbols) and model B (filled symbols), respectively (left panel), and the O_2^+ ion densities and the ratio of the O_2^+ densities obtained for model A and B (right panel), as a function of the pressure, at a driving voltage amplitude of 1000 V.

In addition to the study examining the effects of varying the driving voltage amplitude at a fixed pressure, the effects of a pressure variation between 0.55 and 1 Pa at a fixed driving voltage amplitude of 1000 V was also analysed. The corresponding central charged particle densities are shown in figure 5. As the pressure is increased, the density of all species increases in case of both models, following similar trends. However, the ratio of the O_2^+ ion density obtained from model B and model A decreases, as the pressure is increased from 0.55 to 1 Pa. As the pressure is increased, the multiplication of electrons via ionization becomes more efficient and the average energy of electrons arriving at the electrodes decreases as a consequence of the shorter electron free path, making the role of electron-induced secondary electron emission less pronounced in the discharge, i. e. decreasing the difference between the results obtained from the two models.

4. References

[1] Liebermann M A and Lichtenberg A J 2005 *Principles of Plasma Discharges and Materials Processing* 2nd ed (New York: Wiley)

[2] Makabe T and Petrovic Z 2006 *Plasma Electronics: Applications in Microelectronic Device Fabrication* (London: Taylor and Francis)

[3] Chabert P and Braithwaite N 2011 *Physics of Radio-Frequency Plasmas* (Cambridge: Cambridge University Press)

[4] Makabe T 2019 *Jpn. J. Appl. Phys.* **58** 110101

[5] Belenguer P and Boeuf J P 1990 *Phys. Rev.* A **41** 4447–59

[6] Donkó Z 2001 *Phys. Rev.* E **64** 026401

[7] Hannesdottir H and Gudmundsson J T 2016 *Plasma Sources Sci. Technol.* **25** 055002

[8] Kollath R 1956 *Encyclopedia of Physics* Vol. XXI, ed. Flügge S (Berlin, Springer) p 264

[9] Horváth B, Daksha M, Korolov I, Derzsi A and Schulze J 2017 *Plasma Sources Sci. Technol.* **26** 124001.

[10] Horváth B, Schulze J, Donkó Z and Derzsi A 2018 *J. Phys. D: Appl. Phys.* **51** 355204

[11] Sun J-Y, Wen D-Q, Zhang Q-Z, Liu Y-X and Wang Y-N 2019 *Phys. Plasmas* **26** 063505

[12] Derzsi A, Horváth B, Donkó Z and Schulze J 2020 *Plasma Sources Sci. Technol.* **29** 074001

[13] Hartmann P, Wang L, Nösges K, Berger B, Wilczek S, Brinkmann R P, Mussenbrock T, Juhasz Z, Donkó Z, Derzsi A, Lee E and Schulze J 2020 *Plasma Sources Sci. Technol.* **29** 075014

[14] Derzsi A, Lafleur T, Booth J P, Korolov I, Donkó Z 2016 *Plasma Sources Sci. Technol.* **25** 015004

SIMULATION OF ATMOSPHERIC-PRESSURE PLASMA JETS USING FINITE ELEMENT METHOD

Sinéad A. Mannion[1], Tomoyuki Murakami [2], Carla McDonnell[1], Thomas A Field[1], David Riley[1], Steven White[1], William G Graham[1]

[1]*Queen's University Belfast, Northern Ireland, UK,*

[2]*Seikei University, Tokyo, Japan*

E-mail: smannion02@qub.ac.uk

Atmospheric-pressure plasma jets (APPJ) are devices that generate chemically reactive species and operate at atmospheric pressure and ambient temperature for a wide range of applications. Plasmas jets produce charged particles (electrons and ions), neutral metastable species, radicals, electric fields, and VUV and UV photons. This plasma cocktail not only triggers a variety of cell responses (cell detachment, apoptosis), but is also at a temperature that does not damage tissue/skin. APPJs are used routinely in material processing and biomedical applications. Material processing examples include surface modification, etching, and thin film deposition [1]. Plasma medical applications or plasma medicine examples include the killing of cancer cells, wound healing, and sterilisation [2]. The plasma jet at Queen's University Belfast has shown to be effective in bacteria inactivation [3].

The plasma jet consists of helium gas flowing through an open dielectric tube into air at atmospheric pressure and room temperature. Gas flowing through the quartz tube excited by the pulsed voltage given by the copper electrodes creates the plasma. Adding a small impurity to the noble gas produces the chemically active species. The flow rate of the working gas or the electrical field geometry determines the length of the plasma plume. APPJ can be 1000s K in the tube, but the plasma jet itself can have temperatures of a few 100 K making it ideal for biomedical applications.

A plasma fluid simulation with 2D finite element method is being used to model our APPJ. The model created in COMSOL Multiphysics® includes coupled calculations of the plasma, turbulent fluid flow, and heat transfer. The simulation results include the electrical and plasma properties of the jet, including fluid velocity, number density, electron density, reaction rates, plasma potential, and electric fields.

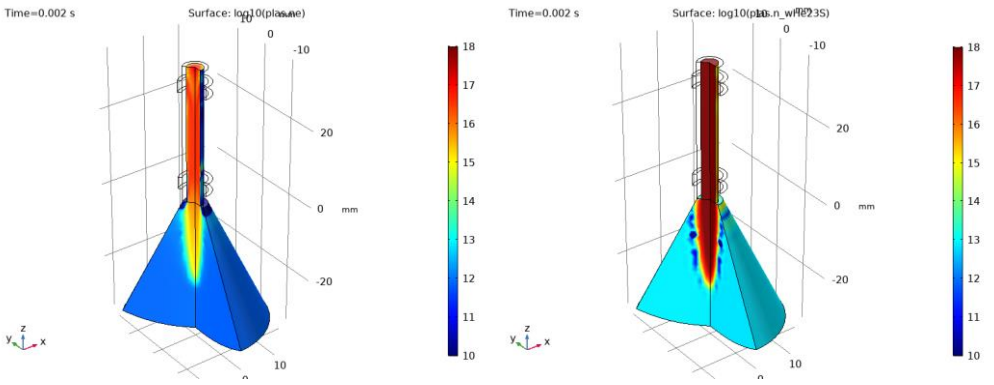

Fig 1. Left) Snapshot of electron density | Right) Snapshot of metastable helium 2 $^3S_1$ state density

Currently, the model only includes He, but a model with reactive species derived from N_2 and O_2 is being developed. The aim is to compare experimental emission observations with predictions from the simulation. A key test of the correlation between the experiment and the model will be to investigate the effect of, for example, input power variation. It will also be interesting to vary the gas composition in the plasma jet.

References

[1] J. Winter, R. Brandenburg, and K. Weltmann, “Atmospheric pressure plasma jets: an overview of devices and new directions," Plasma Sources Science and Technology, vol. 24, no. 6, p. 064001, 2015.

[2] M. Laroussi, X. Lu, and M. Keidar, “Perspective: The physics, diagnostics, and applications of atmospheric pressure low temperature plasma sources used in plasma medicine," Journal of Applied Physics, vol. 122, no. 2, p. 020901, 2017.

[3] Alshraiedeh, Nid'A. H., et al. "Extracellular polymeric substance-mediated tolerance of Pseudomonas aeruginosa biofilms to atmospheric pressure nonthermal plasma treatment." Plasma Processes and Polymers 17.12 (2020): 2000108.

Plasma Bio-Applications and Liquid Applications

Chairman of the session: Marija Radmilović-Rađenović

CHARAKTERIZATION AND APPLICATION OF MICROWAVE PLASMA ON WOUND HEALING

F K. Smejkalová[1], D. Truchlá[1], F. Krčma[1], Z. Kozáková[1], P. Matoušková[1], L. Traikov[2], T. Bogdanov[2]

[1] *Brno University of Technology, Faculty of Chemistry, Purkňova 118, 612 00 Brno, Czech Republic*

[2] *Medical University–Sofia, 1 Georgi Sofiiski Boulevard, 1431 Sofia, Bulgaria*

E-mail:

The aim of this presentation is the investigation of the microwave plasmas for skin wound healing. Microwave discharges used for this work were generated in argon; the surface wave sustained and direct vortex torch were compared. The model wounds on laboratory mousses were treated by plasma and wound healing was examined during 3 weeks after the plasma treatment. Both plasma systems showed healing acceleration. Application of torch discharge was proved to be the most effective method in the healing of skin defects. The plasma vortex system was visualized using fast camera at selected powers and gas flows. Additionally, determination of active particles was taken by optical emission spectroscopy. Based on these measurements, plasma parameters were determined: electron temperature, rotational and vibrational temperatures. To determine role of different plasma active species, the treatment of indigo coloured artificial skin model was treated under various conditions by both plasma systems. Results show that the direct interaction between plasma particles is the main effect, role of radiation, only, is more or less negligible.

Acknowledgments: This work was supported by the project Posilenie výskumno-vývojovej kapacity Slovensko-českého cezhraničného regiónu v oblasti plazmových technológií pre medicínské použitie within the programe EU INTEREG VA SK-CZ, number 304011P709.

TREATMENT OF ACID BLUE 25 DYE BY PLASMA ACTIVATED WATER

Amit Kumar[1], Nikola Škoro[1], Wolfgang Gernjak[2,3] and Nevena Puač[1]

[1] *Institute of Physics Belgrade, University of Belgrade, Serbia*
[2] *Catalan Institute for Water Research (ICRA), University of Girona, Spain*
[3] *Catalan Institution for Research and Advanced Studies (ICREA), Barcelona, Spain*

E-mail: amit@ipb.ac.rs, nevena@ipb.ac.rs

The removal of acid blue 25 (AB25) dye from water by using plasma-activated water (PAW) has been investigated in this study. PAW was produced by using an Ar atmospheric pressure plasma jet (APPJ) with a pin electrode type configuration. After treatment of dye solution with PAW, we observed that dye could be effectively eliminated from water.

1. Introduction

Removal of dyes from aqueous solutions by using different types of atmospheric pressure plasmas has proven its efficiency [1]. Recently, APPJs are used in treatments of clean water in order to create PAW [2]. PAW contains a cocktail of various chemically active oxygen (e.g. ·OH, H_2O_2, O_3, O_2^-) and nitrogen (e.g. NO·, NO_2^-, NO_3^-, $ONOO^-$, $OONO_2^-$) species [3], with many of these species having high oxidation potential, thus making PAW potentially efficiently decontaminant polluted water. Here, we present the results of the removal of AB25 ($C_{20}H_{13}N_2NaO_5S$) dye from aqueous solution by using PAW.

2. Experimental setup

The schematic of the experimental apparatus is illustrated in Figure 1. The APPJ consists of glass, ceramic tube and stainless steel electrode. The stainless steel wire type electrode is used as a powered electrode. The powered electrode with a sharpened edge diameter of 1 mm is placed inside the ceramic tube. Both are inserted in the centre of the glass tube. The outer and inner diameters of the glass tube are 6 mm and 4 mm, respectively. The copper tape served as a ground electrode and was wrapped over the bottom of the sample vessel. The plasma was driven by a commercial high voltage RF power supply. The voltage and current at the powered electrode were determined by a high voltage probe and a current probe, respectively. The voltage across the resistor was measured by a voltage probe. The voltage and current waveforms were recorded by using a digital oscilloscope.

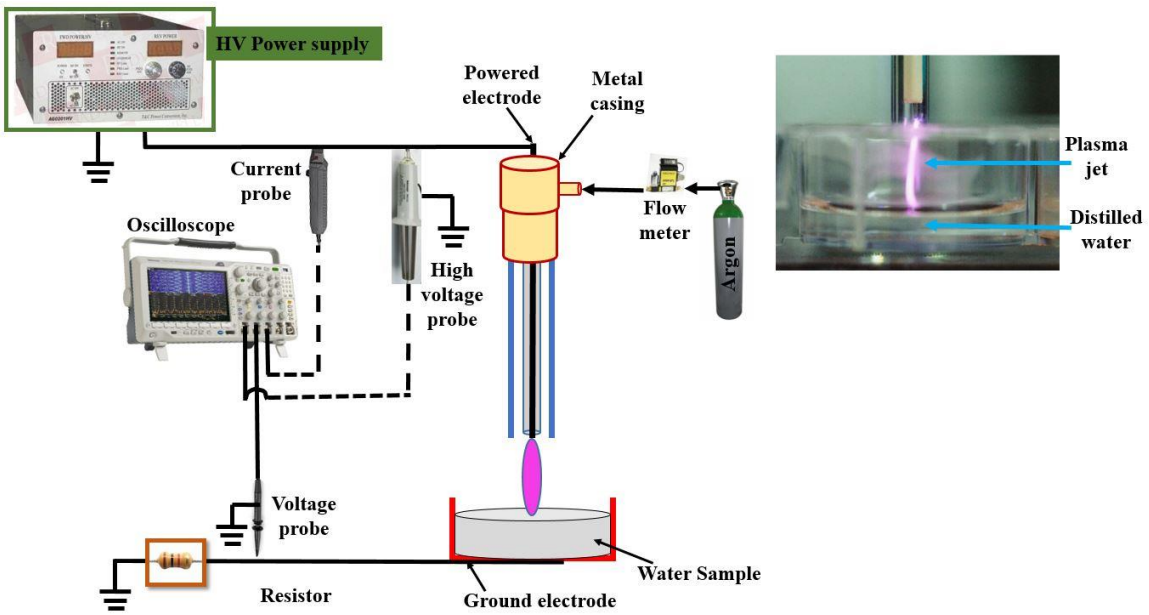

Figure 1. Schematic diagram (left) and photograph (right) of the plasma jet over the liquid surface.

PAW has been generated by exposure of distilled water for 10 minutes to the plasma jet. PAW was mixed with dye-containing solution immediately after treatment. Experimental parameters of plasma jet: plasma power 11 W, frequency 334 kHz, the flow rate of feed gas 1 standard liter per minute, the distance between the tip of the electrode and water surface 10 mm, treatment time 10 min, sample volume 5 ml. PAW and AB25 containing solution has been characterized for several days by using a spectrophotometer to obtain dye concentration.

3. Results and discussion

It can be seen from Figure 1 that AB25 concentration decreased and removal efficiency increased with the number of days. The removal efficiency of the order 44.7 % and 71.0 % was obtained in 4 days and 17 days of analysis, respectively. The maximum increase in the removal rate was obtained in the first 7 days after the treatment. We proposed the hypothesis that the observed effect can be connected to long-living reactive species in PAW but precise processes will be investigated in further research.

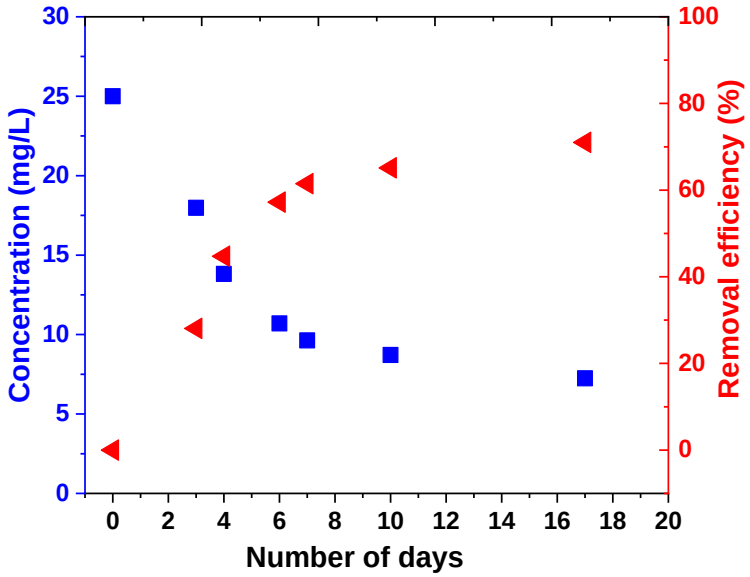

Figure 2. AB25 decomposition and removal efficiency during 17 days (C_o = 25 mg/L).

4. Conclusion

We studied the degradation of AB25 by using PAW. PAW was generated by Ar APPJ, whereas APPJ was driven by a commercial high voltage RF high voltage power supply with a frequency of 334 kHz. The experimental results showed that PAW could a good candidate for the removal of AB25 from aqueous solution.

5. Acknowledgement

This work was done within project NOWELTIES. NOWELTIES received funding from the European Union's Horizon 2020 research and innovation programme under the Marie Skłodowska-Curie grant agreement No. 812880. We thank IPB for hosting the NOWELTIES project.

6. References

[1] Hijosa-Valsero, M., Molina, R., Montràs, A., Müller, M., & Bayona, J. M. (2014). Decontamination of waterborne chemical pollutants by using atmospheric pressure nonthermal plasma: a review. Environmental Technology Reviews, 3(1), 71-91.

[2] Shaw, P., Kumar, N., Kwak, H. S., Park, J. H., Uhm, H. S., Bogaerts, A., & Attri, P. (2018). Bacterial inactivation by plasma treated water enhanced by reactive nitrogen species. Scientific reports, 8(1), 1-10.

[3] Zhou, R., Zhou, R., Prasad, K., Fang, Z., Speight, R., Bazaka, K., & Ostrikov, K. K. (2018). Cold atmospheric plasma activated water as a prospective disinfectant: the crucial role of peroxynitrite. Green Chemistry, 20(23), 5276-5284.

Plasma generation in NaCl and KBr solutions

Fayza Hassan[1], Kealan McAllister[1], Thomas A. Field[1], William G. Graham[1]

[1] *Centre for Plasma Physics, School of Mathematics and Physics, Queen's University Belfast, University Road BT7 1NN, United Kingdom*
E-mail: fhanafyhassan01@qub.ac.uk

Plasma discharges, produced by applying high voltage in liquid, are widely applicable in a number of novel technologies [1–3]. They are widely used in nanoparticle fabrication [4, 5], in water purification [6–8], and in several biomedical applications [9]. The complex physics of the electric discharge phenomena in liquids is not fully understood. It is well accepted, however that, with low voltages and higher conductivity solutions, the plasma discharge in solution is highly influenced by the formation of a bubble or gas film around the electrode tip where the discharge occurs [10]. Recent work in our group has investigated the formation of this vapour layer around the electrode prior to plasma formation [11].

In this presentation, plasma discharges created by applying HV DC pulses in potassium bromide and sodium chloride solutions will be described. The plasmas were formed between two tungsten electrodes in a pin-to-pin configuration and with the electrodes immersed in the liquid. An Oscilloscope was used to record the voltage applied across the electrode, the current through the solution and the photomultiplier tube (PMT) signal, which measures light emission. A nanosecond gated intensified charge coupled device (ICCD) camera was used to record shadowgraphs with backlighting to observe the formation of the vapour layer. The ICCD camera was used without backlighting to observe plasma emission. Optical emission spectroscopy was used to observe emission spectra from the plasma.

The results indicate that initially there was formation of a gas bubble due to ohmic heating between the two electrodes followed by electrical breakdown across the gap. Time-independent broadband optical spectra of both solutions were measured. Emission lines of hydrogen (486.13nm, 656.28nm) and oxygen (777nm) appeared with both solutions. No evidence was found for emission from chlorine or bromine atoms. The difference between KBr and NaCl solution spectrum is the appearance of potassium emission at 767nm instead of the appearance of sodium (589.5 nm) emission. The broadening of Hα is observed as a Lorentzian profile, therefore it can used for estimation of the number of electron density using the value of full width half-Maximum. This study provides a promising approach for the investigation of plasma under KBr and NaCl solutions.

References

[1] WG Graham and KR Stalder. Plasmas in liquids and some of their applications in nanoscience. Journal of Physics D: Applied Physics, 44(17):174037, 2011.
[2] Davide Mariotti and R Mohan Sankaran. Microplasmas for nanomaterials synthesis. Journal of Physics D: Applied Physics, 43(32):323001, 2010. 2
[3] Hyun-Jin Kim, Jun-Goo Shin, Choon-Sang Park, Dae Sub Kum, Bhum Jae Shin, Jae Young Kim, Hyung-Dal Park, Muhan Choi, and Heung-Sik Tae. In-liquid plasma process for size-and shape-controlled synthesis of silver nanoparticles by controlling gas bubbles in water. Materials, 11(6):891, 2018.
[4] S Yatsu, H Takahashi, H Sasaki, N Sakaguchi, K Ohkubo, T Muramoto, and S Watanabe. Fabrication of nanoparticles by electric discharge plasma in liquid. Archives of Metallurgy and Materials, 58(2):425–429, 2013.
[5] Sri balaji Ponraj, Zhiqiang Chen, Lu Hua Li, Jayanth Suryanarayanan Shankaranarayanan, Gayathri Devi Rajmohan, Johan Du Plessis, Andrew J Sinclair, Ying Chen, Xungai Wang, Jagat R Kanwar, et al.

Fabrication of boron nitride nanotube–gold nanoparticle hybrids using pulsed plasma in liquid. Langmuir, 30(35):10712–10720, 2014.
[6] John Foster, Bradley S Sommers, Sarah Nowak Gucker, Isaiah M Blankson, and Grigory Adamovsky. Perspectives on the interaction of plasmas with liquid water for water purification. IEEE Transactions on Plasma Science, 40(5):1311–1323, 2012.
[7] Muhammad Arif Malik. Water purification by plasmas: Which reactors are most energy efficient? Plasma Chemistry and Plasma Processing, 30(1):21–31, 2010.
[8] John E Foster. Plasma-based water purification: Challenges and prospects for the future. Physics of Plasmas, 24(5):055501, 2017. 3
[9] KD Weltmann and Th Von Woedtke. Plasma medicine—current state of research and medical application. Plasma Physics and Controlled Fusion, 59(1):014031, 2016.
[10] Hung-wen Chang and Cheng-che Hsu. Diagnostic studies of ac-driven plasmas in saline solutions: the effect of frequency on the plasma behavior. Plasma Sources Science and Technology, 20(4):045001, 2011.
[11] L Asimakoulas, WG Graham, F Krcma, L Dostal, KR Stalder, and TA Field. Fast framing imaging and modelling of vapour formation and discharge initiation in electrolyte solutions. Plasma Sources Science and Technology, 29(3):035013, 2020.

Treatment of DMEM and RPMI 1640 cell medium by DBD type atmospheric pressure plasma jet

Anđelija Petrović[1], Nikola Škoro[1] and Nevena Puač[1]

[1]*Institute of Physics, University of Belgrade, Pregrevica 118, 11080 Belgrade, Serbia*
e-mail: andjelija@ipb.ac.rs

Here we will present the results of the plasma treatment of the DMEM and RPMI 1640 cell culture mediums. Both mediums were treated by Dielectric Barrier Discharge (DBD) type of atmospheric pressure plasma jet. After treatment concentrations of RONS were determined by spectrophotometry and colorimetric methods.

1. Introduction

Plasma medicine is interdisciplinary research field that combines studies in physics, biology, chemistry and medicine [1]. The use of plasma on living cells and tissues has already been thoroughly investigated. Recently, indirect application previously prepared Plasma Activated Medium (PAM) on cells has also attracted great attention, since the cells are normally surrounded or covered with various biological fluids. Therefore, the chemistry induced by the plasma in the aqueous state becomes essential and crucial for the biological outcomes in the treatment of different cell types [2].
In this work we have investigated effects of plasma treatment on cell culture mediums DMEM and RPMI 1640. Atmospheric pressure plasma jets able to generate reactive oxygen and nitrogen species in medium which is then used as PAM.

2. Experimental setup

The physical and chemical properties and potential application of PAM depends on different plasma sources which are employed as well as different medium. We have used two configurations (with one and two electrodes) of dielectric barrier discharge (DBD) type of the APPJ system powered by kHz sine wave high-voltage power supply system (Fig. 1). Helium was used as working gas with the 2 slm gas flow. The distance between the ending of the APPJ tube and surface of the sample, which was contained in a well of a micro-titter plate, was 5 mm. After the treatment the effects of plasma were investigated by spectrophotometry and colorimetric methods. Concentrations of nitrite ions, nitrate ions and hydrogen peroxide were determined and correlated with the different type of medium.

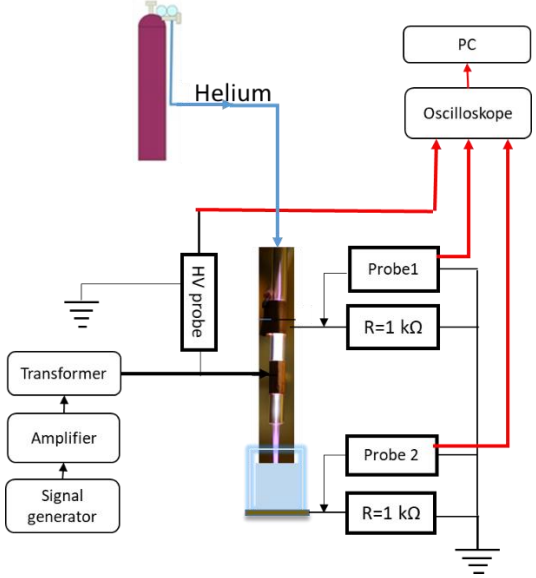

Fig. 1. Schematic diagram of plasm treatment medium by DBD jet

3. Results and discussion

Figure 2 shows the increase in concentrations of reactive species in two different media RPMI 1640 and DMEM after 5 minutes of treatment by 2 electrodes DBD atmospheric pressure plasma jet. Before treatment, the concentration of hydrogen peroxide and nitrate was 1 mg/l and 32 mg/l respectively, while

there was no nitrite in RPMI 1640 medium. There were not reactive species measured by colorimetric and spectrophotometry methods in DMEM medium before the treatment. Although the treatment conditions are the same, the concentration of hydrogen peroxide in PAM-RPMI 1640 is more than 6 times higher than in PAM-DMEM, while the concentration of nitrites is twice as high. Nitrate concentration in PAM-RPMI 1640 also increased after treatment while in PAM-DMEM the colorimetric method did not show any nitrates after treatment as well as before treatment. The differences in concentrations stem from the different chemical compositions of these two mediums that induces different chemical reactions during plasma treatment. Consequently, different concentrations of reactive species in PAM will give different effects on the cells.

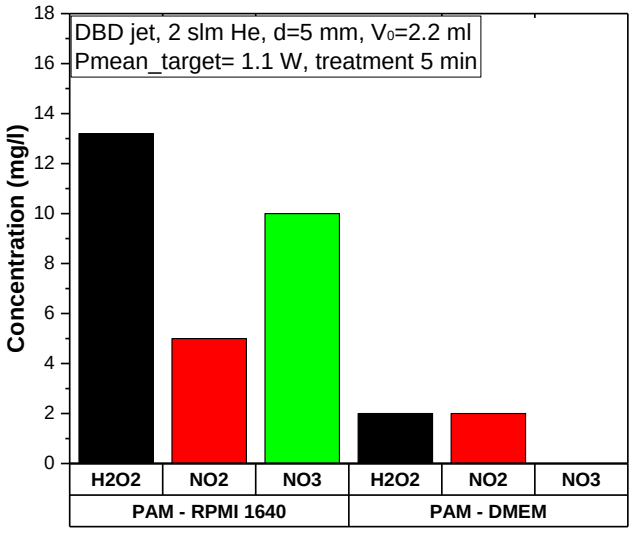

Fig. 2. Increase in reactive species concentrations in PAM-RPMI 1640 and PAM-DMEM after 5 min of treatment and 1.1 W power deposited in the plasma treatment by DBD jet

4. Conclusion

In order to achieve the desired influence of PAM on the cells, the first step is to investigate the effects of plasma treatment on the medium after treatment. It was shown that PAM properties depends on plasma source, treatment time feeding gas and power deposited in the plasma treatment. Here we investigated the influence of the composition of liquid, i.e. type of medium on plasma RONS production. The experimental results show that employment of a Dielectric Barrier Discharge (DBD) type of atmospheric pressure plasma jet produces different RONS concentrations in mediums RPMI 1640 and DMEM while operating with the same working gas and at the same power.

5. Acknowledgments

This research has been supported by MESTD Republic of Serbia projects III41011 and ON171037. Part of the research was funded by IPB through grant by MESTD.

6. References

[1] Weltmann K D, Kindel E, von Woedtke T, Hähnel M, Stieber M and Brandenburg R 2010 Atmospheric-pressure plasma sources: Prospective tools for plasma medicine *Pure Appl. Chem.* **82** 1223–37

[2] D. Graves, *J. Phys. D: Appl. Phys*. **45**, 263001 (2012)

METABOLIC ACTIVITY IN RELATION TO BACTERIAL VIABILITY INDUCED BY TRANSIENT SPARK DISCHARGE

Aleksandra Lavrikova[1], Helena Bujdáková[2], Karol Hensel[1]

[1]*Division of Environmental Physics, Faculty of Mathematics, Physics and Informatics*
[2]*Department of Microbiology and Virology, Faculty of Natural Sciences,*
Comenius University, Bratislava, Slovakia
E-mail: lavrikova6@uniba.sk

Transient spark discharge plasma generated in ambient air was applied to liquid solutions of planktonic *S. aureus* and *E. coli* bacteria circulating through the discharge zone. Metabolic activity and bacterial viability induced by direct plasma treatment in different types of liquids and bacterial growth phases were evaluated and correlated with concentrations of reactive species in liquids. Plasma treatment of *E. coli* / *S. aureus* in saline solution for 10 min resulted in a decrease in metabolic activity by 68 / 66% and bacterial population by 2.5 / 2.8 log, respectively.

1. Introduction

Multiple applications of cold atmospheric plasma (CAP) and plasma-activated water (PAW) in biomedicine are getting more attention in recent years. They require comprehensive and in-depth research of the complex mechanisms of the interaction of cold plasmas with biological systems at all levels. The understanding of basic mechanisms of plasma effects on living cells is one of the main preconditions to develop systematically innovative methods for bio-decontamination. One of the major factors that influences inactivation efficacy of CAP is the background environment (e.g. type of liquid) [1]. The liquid-phase processes have been identified to be the main key to determine detailed pathways of plasma-cell interactions. Liquids and bacterial suspensions after treatment by CAP become antimicrobial and these effects can be attributed to the generation of redox-active species (reactive oxygen and nitrogen species, RONS) [2]. Interestingly, the stable end-products in different plasma-treated liquids (non-buffered and buffered water or saline solutions, cell culture media) are more or less the same (hydrogen peroxide, nitrite and nitrate) which suggests general pathways of chemical reactions triggered by plasma [3][4]. Despite this, bactericidal effect varies depending on the type of a liquid [5]. The objective of this work was to investigate the effect of transient spark discharge plasma on planktonic *Escherichia coli* and *Staphylococcus aureus* in culture media, buffered and saline solutions and establish the correlation between their metabolic activity and viability.

2. Materials and methods

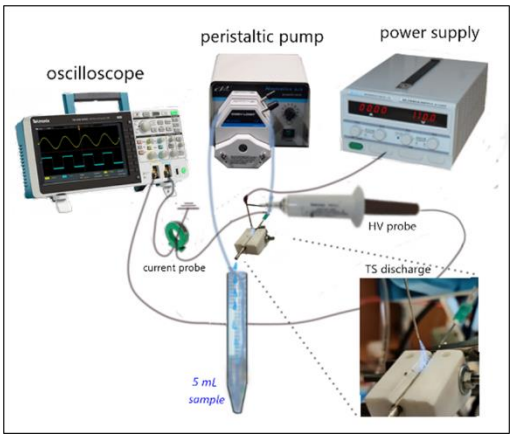

Fig. 1. Experimental Setup

Transient spark (TS) discharge (DC-driven self-pulsing repetitive streamer to spark transition discharge) was operated in ambient atmospheric pressure air in a direct contact with a bacterial suspension (volume = 5 mL initial $C_n=10^7$ CFU/mL) circulated by a peristaltic pump through the discharge plasma zone (Fig.1). The discharge was operated at the constant applied voltage ~14 kV and pulse repetition frequency ~ 2 kHz, and plasma treatment times 5 and 10 min.

The standard strains of Gram-positive *S. aureus* CCM 3953 and Gram-negative *E. coli* CCM 3954 bacteria were used and treated by the plasma during their stationary/exponential phase of growth. After exposition to plasma, changes in metabolic activity by MTT reduction assay and bactericidal effect by colony forming unit (CFU) enumeration method were analysed. All experiments were performed in three different solutions: culture media (Mueller Hinton Broth, MHB), saline solution (saline) and phosphate-buffered saline solution (PBS). In addition to biological analysis, the accumulation of RONS (nitrites NO_2^-, nitrates NO_3^-, hydrogen

peroxide H_2O_2) in the solutions was measured by UV-VIS absorption spectroscopy [6]. Changes in pH, electrical conductivity, temperature and ORP of treated liquids were monitoring during experiments, too.

3. Results

TS discharge resulted in an effective inactivation (up to 3 log reduction) of *S. aureus* and *E. coli* in physiological saline solution. On the other hand, it had almost no effect on the viability in PBS and culture media. Increasing plasma treatment time did not cause stronger bactericidal effect. Once the plasma was turned off the bactericidal effects continued and this delayed effect resulted in a complete inactivation of *E. coli* after 1 hour, and 5.05 log reduction of *S. aureus* after 2 hours incubation.
Metabolic activity was not in a correlation with viability of bacteria as it decreased with increasing treatment time for both *S. aureus* and *E. coli* (Fig. 2) in all three types of liquids. Trend of metabolic activity suppression in different growth phase of *E. coli* in saline solution was detected: in the stationary phase, activity was suppressed by 50% in 5 and 10 minutes, whereas in the exponential phase, 5 minutes resulted in 57% suppression, and 10 minutes in 68%.
Measurements of RONS showed concentration of H_2O_2 in deionized water, buffered and saline solutions increased with increasing treatment time. The maximum accumulation of NO_2^- was obtained in buffered solution. In deionized water and saline solution predominance of NO_3^- was observed.

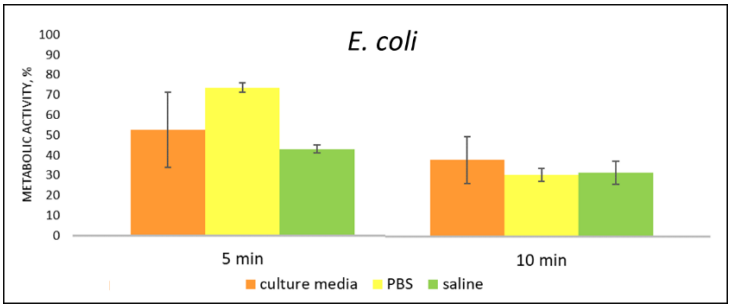

Fig. 2. Metabolic activity of *E. coli* after plasma treatment in culture media (Mueller Hinton Broth, MHB), PBS (phosphate-buffered saline) and saline solution (NaCl, 0.85%).

4. Conclusion

Reduced metabolic activity and the presence of RONS did not cause bactericidal effect against *E. coli* and *S. aureus* in PBS and culture media after TS discharge treatment. RONS in combination with acidic environment promoted bactericidal effect in saline solution. The findings prove that plasma treatment can result in a significant bactericidal efficacy that depends on type of a liquid and less on the bacteria growth phase. The mechanisms of specific action of RONS on individual components of bacteria (cell membrane, DNA, proteins) should be investigated thereafter. Study of CAP interaction with bacterial cells will allow us to obtain additional knowledge required to embody the full potential of cold plasma in biomedicine.

Acknowledgment

This research was funded by Slovak Research and Development Agency grant APVV-17-0382.

5. References

[1] X. Liao *et al.*, *Food Res. Int.* (2018), 105, 178–183.
[2] G. Daeschlein, *Comprehensive Clinical Plasma Medicine: Cold Physical Plasma for Medical Application*, Springer Int. (2018), 113–125.
[3] H. Jablonowski and T. von Woedtke, *Clin. Plasma Med.* (2015), 3 (2), 42–52.
[4] A. Khlyustova et al., *Front. Chem. Sci*. (2019), 13(2), 238–252
[5] M. Huang et al., *Appl. Sci.* (2018), 8 (11), 1–15.
[6] B. Tarabová et al., *Plasma Process Polym.* (2018), 15, e1800030.

Elementary Processes and Plasma Chemical Reactions

Chairman of the session: Tom Field

INVESTIGATION OF MAGIC NUMBERS OF NEON CLUSTER IONS

Stefan Bergmeister [1], Siegfried Kollotzek [1], Lukas Tiefenthaler [1],

Simon Albertini [1], Elisabeth Gruber [1], Fabio Zappa [1], Paul Scheier [1], Olof Echt [1,2]

[1]*Institut für Ionenphysik und Angewandte Physik, Universität Innsbruck, A-6020 Innsbruck, Austria*
[2]*Department of Physics, University of New Hampshire, Durham NH 03824, USA*

E-mail: stefan.bergmeister@uibk.ac.at

The stability of Ne_n^+ clusters up to n = 197 generated via pickup of neon into charged helium nanodroplets (HNDs) has been investigated to receive knowledge of their structural arrangement. Different local anomalies in the abundance distribution are found, which may arise from different cluster formation processes, depending on the charge state of the pure HND.

1. Introduction

The investigation of the size and stability of Ne_n^+ clusters have already started in 1987 with the observation of a stable icosahedral structure the cluster can form [1]. Clusters in size up to n = 90 were examined according to their stability and results were briefly compared to other rare gas clusters. Since that time no other paper has covered the size at and above the second icosahedral shell closure of neon clusters. In the present study the question, which stable size and structure neon clusters are likely to form will be revived and with new techniques, larger cluster will be produced and investigated.

2. Experimental setup

For the measurements of Ne_n^+ clusters two slightly different setups have been used. One setup will be explained in more detail and the difference to the other setup will be shortly illustrated. A cut-away view of the experimental setup is shown in figure 1. Flowing through a gas line attached to a two-stage closed cycle refrigerator, helium 6.0 at a pressure of 20 MPa gas gets cooled down to temperatures as low as 4K and by counter heating in combination with a PID controller a stable temperature of 9.7K was achieved. Expansion through a 5 µm nozzle into vacuum leads to the formation of HNDs with an average size of about half a million He atoms. After passing a skimmer the HNDs get multiply ionized by electron impact [2]. Utilizing an electrostatic sector analyzer, droplets with a specific mass per charge ratio are selected. The highly charged droplets (maximum charge state of 28) fly through a differentially pumped pick-up region filled with neon 5.0. Collisions between the charged HNDs and neon will lead to capture of Ne atoms that are attracted by the charge centers. Charge transfer to the first Ne atom and attachment of additional dopants leads to growth of Ne_n^+ clusters in the droplets, and evaporation of helium atoms. Multiple collisions with room-temperature helium gas, introduced into a subsequent RF-hexapole, evaporates helium from the HNDs doped with neon cluster ions which finally releases bare Ne_n^+ cluster ions. The neon cluster are guided through an additional quadrupole mass filter and another hexapole (both not used in these measurements) and are finally analyzed by a time of flight mass spectrometer.
In comparison, the other setup produces only singly charged HNDs due to other formation, ionization and bending conditions. Apart from other chamber size dimensions, the only mechanical difference is an electrostatic quadrupole bender instead of the electrostatic sector mass analyzer. Further information to the setup is published elsewhere [3].

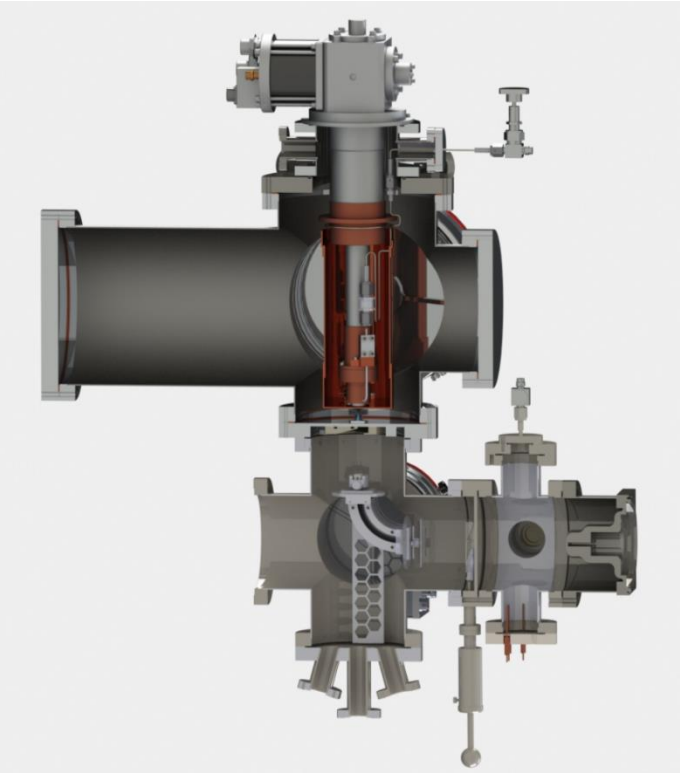

Fig. 1. Rendering of a cross-section view of the in detail described setup. The helium gas line, starting from the upper right, is attached to the two stages of a cryostat, here shown in red. In the chamber below the electron impact ionization source and the mass per charge selecting electrostatic sector mass analyzer are visible. To the right in a light gray color the pick-up chamber is shown. The adapter to the bottom right of the picture represent the connection to the Q-TOF mass spectrometer (not visible in this figure).

3. Results and Discussion

Two different sequences of magic numbers are discernible in the mass spectra. One setup produces with initially multiply charged HNDs local anomalies in the abundance distribution at values of n = 7, 13, 19, 26, 29, 34, 55, 71, 81 and even higher numbers, in comparison growth in singly charged droplets with the other setup produce values of n = 14, 21, 55/56, 75, 82 with also weaker anomalies at numbers in between. The difference in the stability of the neon clusters can be explained by the difference in the charge state of the undoped HNDs. The suggestion is that the occurrence of multiply charges leads to the growth of a distinctly different structural family compared to singly charged ones [4]. Three recorded spectra of neon clusters grown in large, multiply charged HNDs are shown in figure 2.

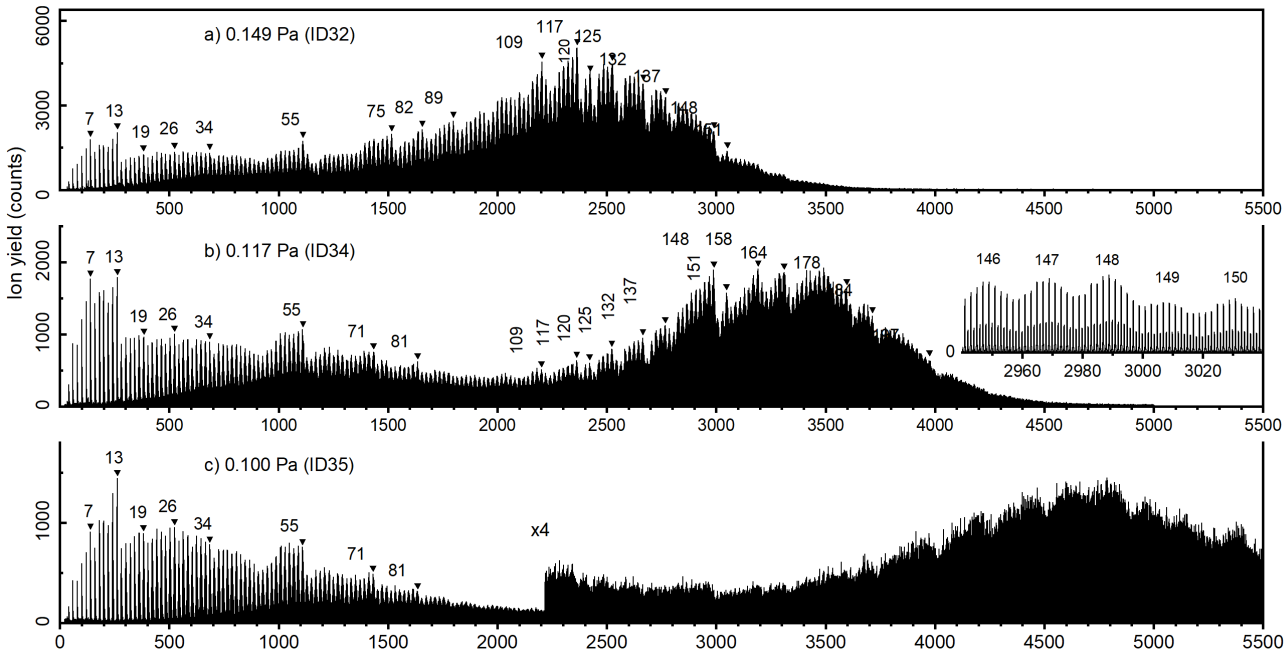

Fig. 2. Three mass spectra of neon cluster ions grown inside initially multiply charged HNDs. The pressure of He in the collision cell to extract the neon cluster ions from the HNDs is decreased from 0.149 Pa in panel a) to 0.1 Pa in panel c). In panel b) the inset reveals the isotopologues of Ne_n^+ around $n \approx 148$.

4. Acknowledgement

This work was supported by the Austrian Science Fund, FWF, Project Nr. W1259, T1181, I4130 and the European Commission, EFRE (K-Regio project FAENOMENAL, grant number EFRE 2016-4)

5. References

[1] Märk T D and Scheier P 1987 *Chemical Physics Letters 137*(3), 245-249.

[2] Laimer F, Kranabetter L, Tiefenthaler L, Albertini S, Zappa F, Ellis A M, Gatchell M and Scheier P 2019 *Physical Review Letters* 123(16), 165301.

[3] Tiefenthaler L, Kollotzek S, Gatchell M, Hansen K, Scheier P and Echt O 2020 *The Journal of Chemical Physics 153*(16), 164305.

[4] Kollotzek S, Bergmeister S, Tiefenthaler L, Albertini S, Gruber E, Zappa F, Scheier P and Echt O 2020 "On the Stability of Neon Cluster Ions" submitted.

DISSOCIATION OF 2-METHYL-2-OXAZOLINE AND 2-ETHYL-2-OXAZOLINE MOLECULES INDUCED BY LOW-ENERGY ELECTRON IMPACT

Ján Blaško, Peter Papp, Štefan Matejčík

Faculty of Mathematics, Physics and Informatics, Comenius University in Bratislava, Mlynská dolina, 842 48 Bratislava, Slovakia
E-mail: jan.blasko@fmph.uniba.sk

Experimental investigation of electron ionization of 2-methyl-2-oxazoline and 2-ethyl-2-oxazoline was carried out using crossed electron beam and molecular beam method. We have recorded the mass spectra of positive ions at ~ 70 eV and assigned detected masses to possible fragments. The ionization energies of the 2-methyl-2-oxazoline and 2-ethyl-2-oxazoline were determined to be 9.5 eV and 9.13 eV respectively. Appearance energies for the main fragments were for the first time estimated, too.

1. Introduction

Polyoxazolines are a significant group of polymers with a large scale of possible applications for example in materials as thermal sensors. Another application is a carrier system for active substances in drug delivery [1]. Due to their well-known biocompatibility, polyoxazolines have the potential to find a diversity of applications in biological systems. The cationic ring opening polymerization of 2-oxazolines was first publicated in the 1960s, which was later modified with microwave-assisted processes. This technique was used to achieve higher yields [2]. Microwave radiation shortens the polymerization time up to 400 times compared to hot heating [1]. During research in the 1960s, polymerization was investigated through NMR spectroscopy, chromatography, kinetic studies and MALDI-TOF MS [1].

The present work is focused to molecular properties of 2-methyl-2-oxazoline (2M2O) and 2-ethyl-2-oxazoline (2E2O) under electron impact. Using the mass spectrometry technique, the mass spectra of positive ions at ~ 70 eV and cross sections for both molecules was obtained. Threshold energies were determined from cross sections with a suggestion of possible chemical formulas of products.

2. Experimental setup

For investigation of electron induced processes of molecules an experiment with crossed electron and molecular beam was used (see scheme in Fig.1). The molecular beam source (MBS) was filled with the measured sample (2M2O, CAS: 1120-64-5, purity: 98%, Sigma Aldrich and 2E2O, CAS: 10431-98-8, purity > 99%, Sigma Aldrich) and generated the effusive beam passing into the vacuum through capillary. The electrons were produced by trochoidal electron monochromator (TEM) generating an electron beam with a well specified energy and colliding with the molecular beam from MBS. The positive ions were extracted by a weak electric field from the collisional region into the quadrupole mass spectrometer (QMS), where ions with selected *m/z* passed through QMS into the channeltron electron multiplier (CEM) detector.

The pressure in the vacuum chamber during the measurements was in the range of 1×10^{-7} mbar to 5×10^{-7} mbar. The apparatus was operated in two different modes. In the first one the mass spectrum was collected at a constant electron energy of ~70 eV in range from m/z 10 amu to 105 amu for 2E2O and from m/z 10 amu to 90 amu for 2M2O. In the second mode, the ion efficiency curves for particular ions with given *m/z* were measured as a function of incident electron energy (with a step of ~0.025 eV) around the threshold energy of selected ion fragment. The appearance energy (AE) of the selected process after electron ionization was estimated based on the Wannier law [3]. For calibration of the kinetic energy of the electrons we used Ar as well-established calibration gas with threshold energy of first ionization energy of 15.76 eV.

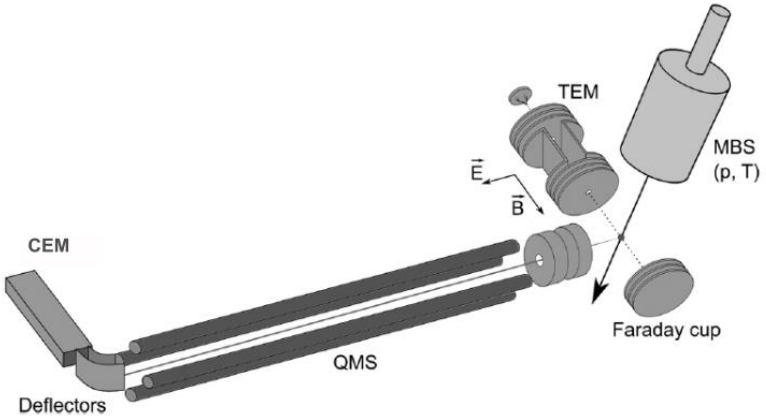

Fig.1. The schema of the electron and molecular crossed beams experiment CEMBIA based on [4].

3. Results

The positive ion mass spectrum of 2M2O recorded at ~70 eV is shown in Fig. 2. The parent molecular ion (P^+) with *m/z* 85 was detected, as well as other fragments already identified in NIST database [5]. The spectrum is in good agreement with the NIST spectrum regardless of intensity of some fragments. The peaks in the spectrum are labeled according to the possible products, more products for one peak are noted if there are more possibilities for one *m/z*. To reveal exact products quantum chemical calculations will be performed in the future. The second heaviest fragment is *m/z* 84 where the hydrogen is dissociated from the molecule. Without the support of theoretical calculations, it is not possible to determine the position from which the H atom dissociated. The highest peak is at mass *m/z* 55, there are three possibilities for this fragment C_2HNO^+, $C_3H_3O^+$, $C_3H_5N^+$. For 2M2O we did not detect formation of product via loss of the CH_3 side chain group. But in the spectrum at the mass *m/z* 15 the cation of methyl group is visible.

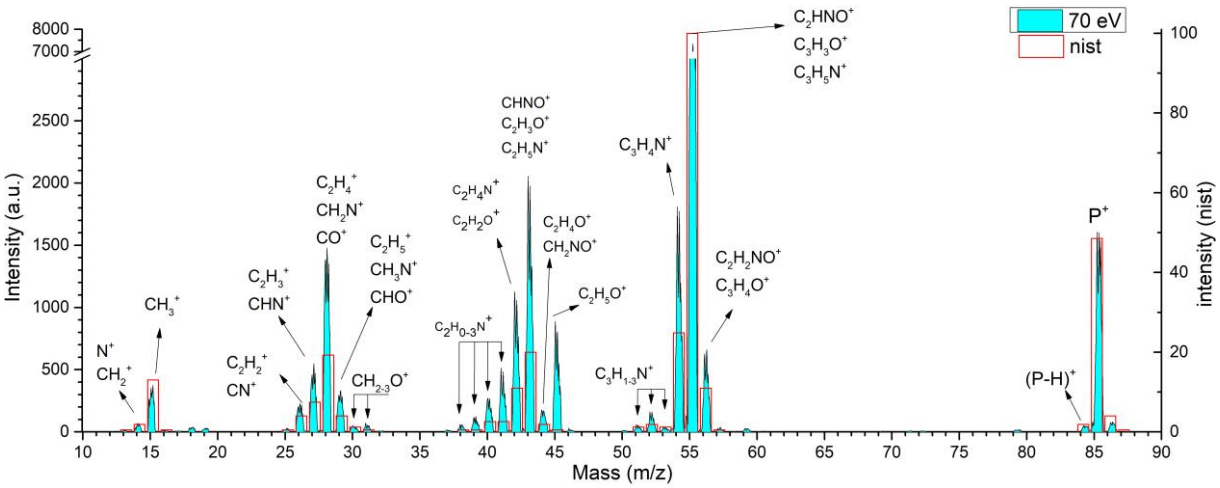

Fig. 2. Mass spectra of measured 2-methyl-2-oxazoline molecule at ~70 eV in comparison with mass spectra from NIST.

The positive ion mass spectrum of 2E2O recorded at ~70 eV is shown in Fig. 3. The parent molecular ion (P^+) has the mass *m/z* 99 which was identified as well as fragments *m/z* 98 where the hydrogen is dissociated from the molecule and *m/z* 69 $(P\text{-}CH_2\text{-}CH_3\text{-}H)^+$ or $(P\text{-}CH_2\text{-}O)^+$. The peak at mass *m/z* 100 is isotope of the parent. In the mass spectrum of 2E2O measured at ~70 eV we have again identified the supposed fragments in agreement with NIST database [6] regardless on intensity of some fragments. Only exclusion is that in the NIST spectrum there is a weak fragment at the mass *m/z* 97 which we did not identify in our spectrum. On the other hand, the fragment at mass *m/z* 49 and *m/z* 45 is seen in our spectrum, and the doubly charged parent ion at *m/z* 48.5. The first fragment is at mass *m/z* 15 which represents methyl group (not shown in the NIST spectrum starting at *m/z* 20). Also, the side chain cation is visible, the ethyl group $(CH_3\text{-}CH_2)^+$ at mass *m/z* 29, however there is the

possibility of creation of another product CHO^+ at this mass. The hydrogen loss is now more efficient than for 2M2O, the $P\text{-}H^+$ ion is more intensive than the parent ion. The most intensive product is at mass *m/z* 54.

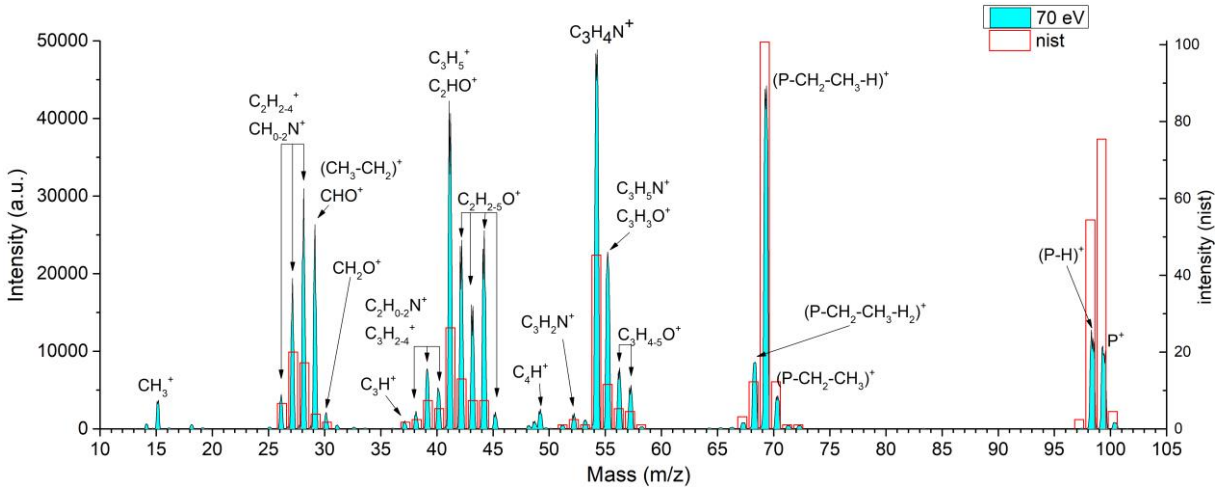

Fig. 3. Mass spectra of 2-ethyl-2-oxazoline molecule at ~70 eV in comparison with mass spectra from NIST.

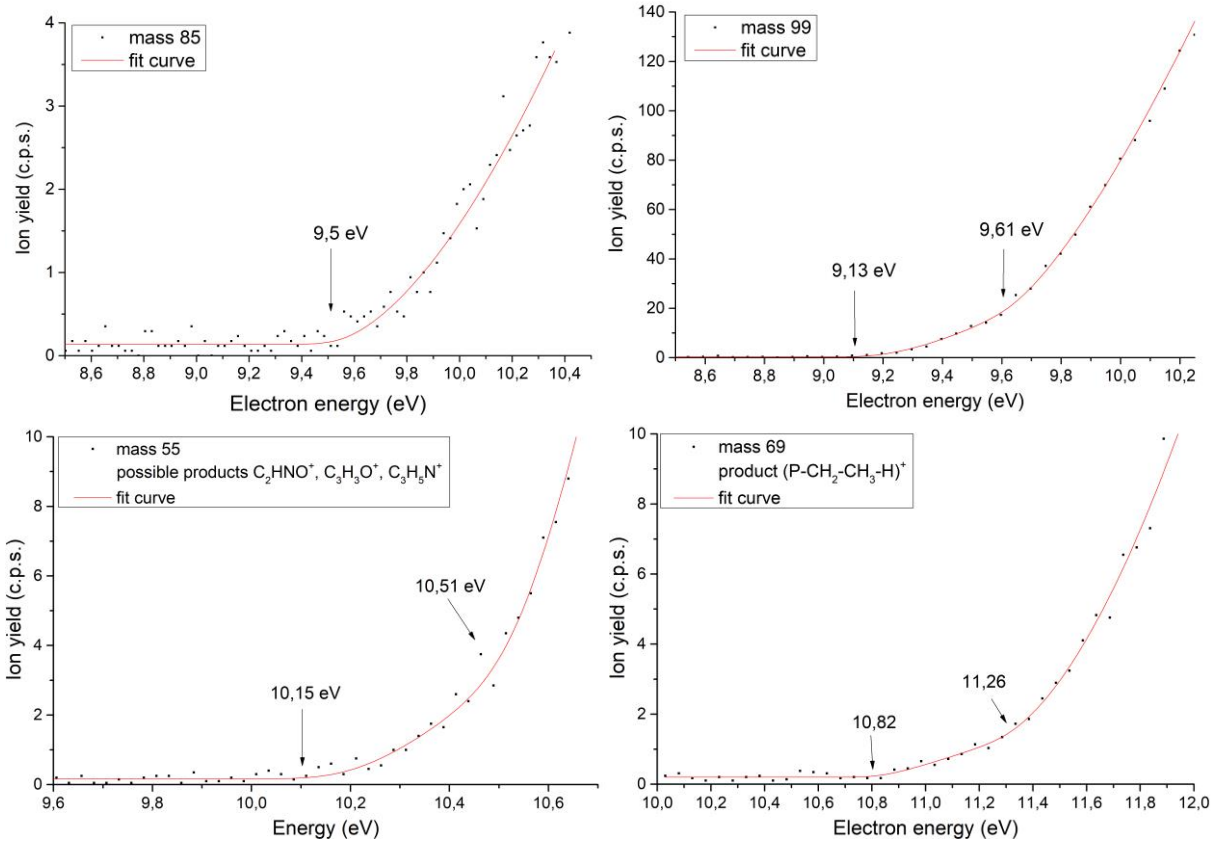

Fig. 4. Region of threshold of cross section of molecule ionization 2-methyl-2-oxazoline (left) and 2-ethyl-2-oxazoline (right)

The ionization energy (IE) for 2M2O is showed at Fig. 4. (top left) and is estimated on 9.5 eV. The IE for 2E2O is 9.1 eV with a second threshold at 9.6 eV, what we can see at Fig. 4 (top right). Subsequently we determine appearance energies for most of the fragments showed in the Tab. 1. From the differences of IE and AE it is possible to determine the dissociative energies (DE) of the products. In the mass spectra and in Tab. 1, we observe some sequences. There are several peaks originating

from hydrogen losses for example for 2M2O at masses *m/z* 51 – 55 representing $C_3H_{1-5}N$. Very similar dissociation is at masses *m/z* 39 – 43 $C_2H_{1-5}N^+$, where H is sequentially dissociated. Carbon was most likely dissociated from the product at *m/z* 55 C_2HNO^+, $C_3H_3O^+$, $C_3H_5N^+$ to give fragment at mass *m/z* 43 $CHNO^+$, $C_2H_3O^+$, $C_2H_5N^+$, and subsequently fragment at mass *m/z* 31 CH_3O^+, CH_5N^+.
In the case of 2E2O, there are also visible sequencies for example at masses *m/z* 41 – 45 representing $C_2H_{1-5}O^+$. Carbon with hydrogen was most likely sequentially dissociated from product at the mass *m/z* 57 $C_3H_5O^+$ to give product at mass *m/z* 44 $C_2H_4O^+$. This fragment was dissociated to product at mass *m/z* 31 CH_3O^+. Another type of sequential dissociation is the CH_2 dissociation from product *m/z* 57 $C_3H_5O^+$ to the products *m/z* 43 $C_2H_3O^+$ and *m/z* 29 CHO^+. At the mass *m/z* 98 H is dissociated from the parent and fragment $(P\text{-}H)^+$ is created. Next fragment is $(P\text{-}CH_2\text{-}CH_3)^+$, where the side chain – ethyl group $CH_2\text{-}CH_3$ is dissociated. The dissociation energy for the side chain is 2.4 eV, what is about 1,19 eV less than in literature for dissociation C-C bond [7]. We did not observe this kind of dissociation in 2M2O, what is according to the NIST. The next 2 peaks are *m/z* 69 $(P\text{-}CH_2\text{-}CH_3\text{-}H)^+$ or $(P\text{-}CH_2\text{-}O)^+$ and *m/z* 68 $(P\text{-}CH_2\text{-}CH_3\text{-}H_2)^+$, where, in addition to the ethyl group, the carbon – bond hydrogens from the ring are also dissociated.

m/z	Supposed products	Energy (eV)
85	P^+	9.5 (IE)
84	$(P\text{-}H)^+$	9.89
56	$C_2H_2NO^+$, $C_3H_4O^+$	10.42
55	C_2HNO^+, $C_3H_3O^+$ $C_3H_5N^+$	10.15 & 10.51
54	$C_3H_4N^+$	13.39
53	$C_3H_3N^+$	14.62
52	$C_3H_2N^+$	13.1
51	C_3HN^+	15.72 & 16.71
45	$C_2H_5O^+$	15.37
44	$C_2H_4O^+$, CH_2NO^+	10.52
43	$CHNO^+$, $C_2H_3O^+$ $C_2H_5N^+$	10.37
42	$C_2H_4N^+$, $C_2H_2O^+$	11.37 & 12.11
41	$C_2H_3N^+$	12.56
40	$C_2H_2N^+$	14.15
39	C_2HN^+	14.63
31	CH_3O^+	12.5 & 13.51
30	CH_2O^+	11.27
29	$C_2H_5^+$, CH_3N^+, CHO^+	13.03 & 13.97
28	$C_2H_4^+$, CH_2N^+, CO^+	13.39
27	$C_2H_3^+$, CHN^+	13.93 & 14.53
26	$C_2H_2^+$, CN^+	11.77 & 14.78
15	CH_3^+	15.46
14	N^+, CH_2^+	16.33

m/z	Supposed products	Energy (eV)
99	P^+	9.13 & 9.61 (IE)
98	$(P\text{-}H)^+$	10.39 & 11.02
70	$(P\text{-}CH_2\text{-}CH_3)^+$	11.53 & 12.41
69	$(P\text{-}CH_2\text{-}CH_3\text{-}H)^+$ $(P\text{-}CH_2\text{-}O)^+$	10.82 & 11.26
68	$(P\text{-}CH_2\text{-}CH_3\text{-}H_2)^+$	12.29 & 12.66
57	$C_3H_5O^+$	11.56 & 12.17
56	$C_3H_4O^+$	10.65 & 11.22
55	$C_3H_5N^+$, $C_3H_3O^+$	12.25 & 13.13
54	$C_3H_4N^+$	12.19 & 12.67
49	C_4H^+	16.5
45	$C_2H_5O^+$	10.61
44	$C_2H_4O^+$	10.53
43	$C_2H_3O^+$	10.26 & 10.8
42	$C_2H_2O^+$	10.96 & 12.02
41	$C_3H_5^+$, C_2HO^+	11.99 & 12.49
40	$C_2H_2N^+$, $C_3H_4^+$	12.29
39	C_2HN^+, $C_3H_3^+$	14.68
38	C_2N^+, $C_3H_2^+$	20.37 & 24.85
32	NH_2O^+, CH_4O^+	12.16
31	HNO^+, CH_3O^+	11.79 & 12.81
30	CH_2O^+	11.13 & 12.17
29	$(CH_3\text{-}CH_2)^+$, CHO^+	12.1 & 12.65
28	$C_2H_4^+$, CH_2N^+	10.87 & 12.26
27	$C_2H_3^+$, CHN^+	13.98
26	$C_2H_2^+$, CN^+	11.5
17	OH^+	10.63
15	CH_3^+	15.37 & 16.65

Tab. 1.: Main products of 2-ethyl-2-oxazoline (right) and 2-methyl-2-oxazoline (left) fragmentation and appearance energies of ions as determined in the present work.

By comparison of the 2M2O and 2E2O table (Tab. 1.), it is possible to notice a supposed common product at *m/z* 55 for 2M2O and *m/z* 69 for 2E2O. However, looking at DE, it can be seen that DE for 2E2O is 1.69 and for 2M2O is 0.65, what makes difference of approximately 1.04 eV. Therefore, it can be concluded that this will not be a common product. For the supposed product CH_3^+, the DE for 2M2O is 5.96 and for 2E2O is 6.24. At the *m/z* 26 with the supposed products $C_2H_2^+$, CN^+ the DE for

2M2O is 2.27 and for 2E2O is 2.37. According to the DE, which is very similar for *m/z* 26, it is very likely that it will be the same product.
The potential fragmentation pathway for the 2E2O is shown in the Fig. 5. In the scheme there is assigned options for a given mass, thanks to that it is possible to assign dissociation energy to some specific bond. Subsequently, the results of bonds energies which represents DE are compared with the tabular values from the literature.

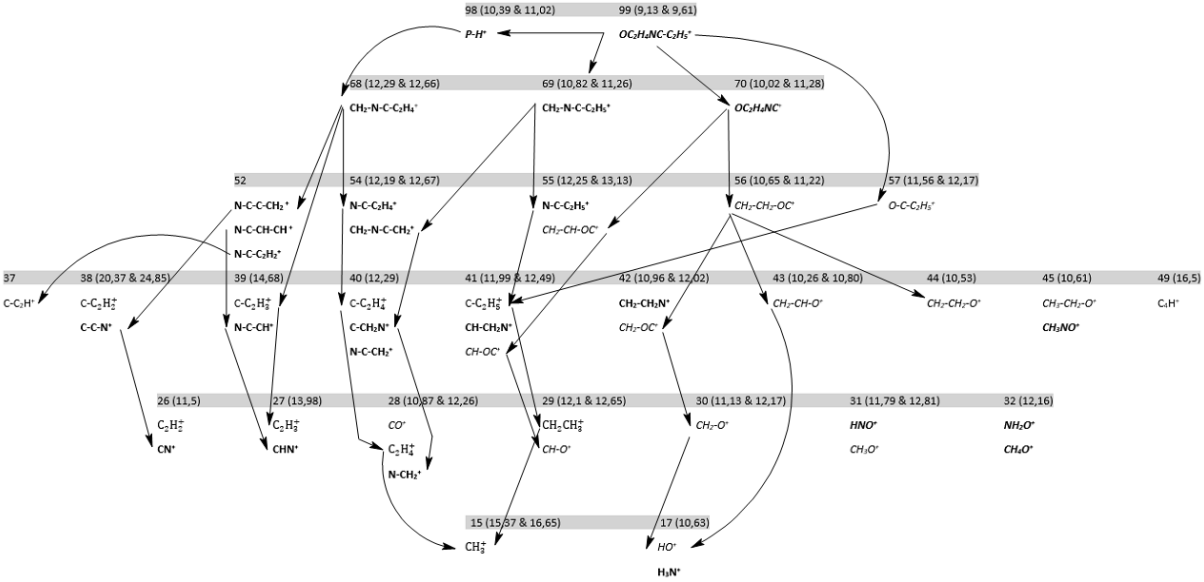

Fig. 5.: Possible fragmentation pathway of 2-ethyl-2-oxazoline.

Acknowledgments: This work was supported by the Slovak Research and Development Agency. Project No. APVV-19-0386. Financing of this work was by the Slovak Grant Agency VEGA 1/0733/17. This project has received funding from the European Union's Horizon 2020 research and innovation programme under grant agreement No 692335.

4. Conclusion

We have studied formation of the positive ions formed by electron impact ionization of 2-methyl-2-oxazoline and 2-ethyl-2-oxazoline by means of crossed electron and molecular beam experiment. We have measured the mass spectra of the molecules at electron energy 70 eV. The measurements at 70 eV showed products of molecules fragmentation in accordance with NIST published data [5,6]. We recorded the ion efficiency curves in the threshold region of the most dominant fragments and estimated the appearance energies of the ions. The ionization energy of the 2-methyl-2-oxazoline´s parent ion was estimated to be 9,5 eV and the ionization energy of the 2-ethyl-2-oxazoline´s parent ion was estimated to be 9,13 eV. The formation of cationic methyl product *m/z* 15 CH_3^+ from 2M2O was observed, in contrast to 2E2O, where not only cationic ethyl product *m/z* 29 CH_2-CH_3 was observed bud also side chain – ethyl group CH_2-CH_3 is dissociated and the cationic fragment *m/z* 70 is formed. Although the appearance energies of ions were determined to reveal the accurate identifications quantum chemical calculations will be performed in the future to provide more insight.

5. References

[1] A. Baumgaertel 2009 *Rapid Commun. Mass Spectrom*, 23 756–762 John Wiley & Sons.
[2] T. Bassiri, A. Levy, M. J. Litt, 1967 *Polym. Sci., Part B: Polym. Lett*, 5 871.
[3] G. H. Wannier 1953 *Physics Review*, 90 817.
[4] M. Lacko, P. Papp and Š. Matejčík 2018 *The Journal of Chemical Physics*, 148 214305.
[5] https://webbook.nist.gov/cgi/cbook.cgi?ID=C1120645&Units=SI&Mask=200#Mass-Spec
[6] https://webbook.nist.gov/cgi/cbook.cgi?ID=C10431988&Units=SI&Mask=200#Mass-Spec
[7] http://www.wiredchemist.com/chemistry/data/bond_energies_lengths.html

DFT STUDY ON THE INTERACTIONS OF LOW ENERGY ELECTRONS WITH PYRIDINE, PYRAZINE, AND THEIR HALO DERIVATIVES

Natalia Tańska[1]

[1]*Institute of Physics and Applied Computer Science, Faculty of Applied Physics and Mathematics, Gdańsk University of Technology, ul. Gabriela Narutowicza 11/12, 80-233 Gdańsk*
E-mail: natalia.tanska@pg.edu.pl

Vertical electron affinities to pyridine, pyrazine and their halo-monosubstituted derivatives were calculated with density functional theory using B3LYP hybrid functional and various basis sets. Relaxed potential energy curves along C-X (X=H, Cl, Br) bond and enthalpies of dissociative attachment of thermal electron to the investigated molecules were also determined to roughly estimate the energetics of the process. The results are in acceptable agreement with the available data.

1. Introduction

Dissociative electron attachment (DEA), shown schematically in the Figure 1, plays a significant role in both science and industry [1]. This chemical reaction control tool is used in the FEBID (Focused Electron Beam Induced Deposition) method [2] or radiotherapy [3]. DEA manifests itself also in many astrophysics and astrochemical processes, for example in auroras of Earth and other planets and in formation of complex molecules in atmospheres, comets and interstellar medium [4]. In many of the above fields, organic or biological molecules are of particular importance.

Potential energy curves (PECs) are very helpful in understanding the dissociative electron attachment, as well as other chemical reactions. To calculate PECs that are useful in electron scattering processes, one should use a sophisticated method such as R-matrix theory [5] or multichannel Schwinger method [6]. Unluckily, each has its flaws, including the need of large computing resources or even fine-tuning to the experimental data to achieve meaningful results. On the other hand, simple and relatively efficient methods of quantum chemistry, such as the second order Møller-Plesset perturbation theory (MP2) or the density functional theory (DFT), can lead to erroneous results when dealing with temporary negative ions (TNIs). This is caused by the fact that the structure is not stable and the calculations could locate the extra electron on a very diffuse orbital. Quite acceptable results can be achieved by using a compromise between the size of the base orbitals and the accuracy of calculations, which has been shown in [7,8]. Pyridine and pyrazine rings are present for example in B vitamins, pharmaceuticals and agrochemicals. As one of the simplest biological molecules, pyridine is considered in astrochemical experiments [9] and nucleic acids based on pyrazine are candidates for the prebiotic RNA precursor [10]. In this work we apply the DFT method with B3LYP functional to obtain the vertical electron affinities (VEAs) and potential energy curves for pyridine, pyrazine and those molecules monosubstituted by chlorine or bromine atom.

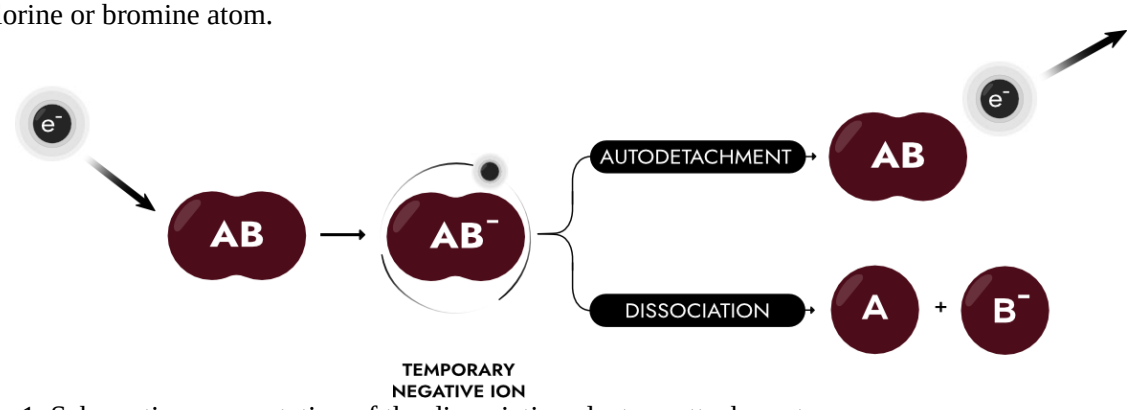

Fig. 1. Schematic representation of the dissociative electron attachment.

2. Details of calculations

All calculations were performed with Gaussian 16 suite. The vertical electron affinities for 2-,3- or 4-substituted pyridines and 2-substituted pyrazines were obtained with basis sets listed in the Table 1 with the B3LYP functional according to the formula:

$$VEA = E(\text{neutral}) - E(\text{anion}) \quad (1)$$

where both of the species are in the optimized neutral geometry. Singly occupied molecular orbitals (SOMOs) were then carefully inspected for the correct symmetry and size, that is, whether they are the resonant π* orbitals of b_1 or b_1-like symmetry. Relaxed potential energy curves along the C_n-X bond (for the numbering of atoms see Figure 2) were calculated with Opt = ModRedundant keyword at the B3LYP/6-31+G(d) level. Separate scans were performed for the neutral molecule, anion lowest π* state, σ* dissociative state and π*/σ* mixed (without any symmetry constraints). The enthalpies of the following reactions were also determined:

$$R - H + e_0^- \rightarrow R^- + H\cdot, \quad (2)$$
$$R - X + e_0^- \rightarrow R\cdot + X^-, \quad (3)$$

where X=Cl, Br and e_0^- is the thermal (near-zero eV) electron.

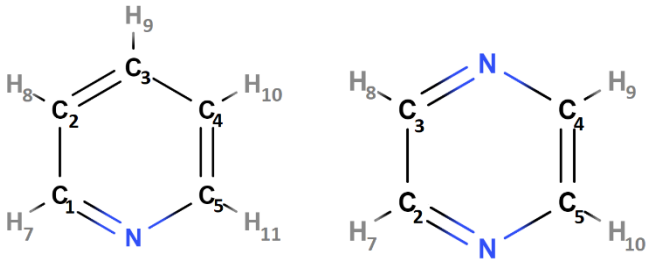

Fig. 2. The numbering of atoms in pyridine and pyrazine used in this work.

3. Results and conclusions

Calculated vertical electron affinities are shown in the Table 1. In the Figure 3 the discrepancies between obtained values and experimental data are depicted. The only available data that concern halo derivatives of investigated compounds are for 2-,3-, and 4-chloropyridine and for 4-bromopyridine. For the 6-31+G(d) and aug-cc-pVTZ the trend is correct and the agreement is acceptable. The 6-311++G(d,p) basis was problematic during the calculations because of the deformed orbitals, and so the results are less predictable.

Tab. 1. Calculated vertical electron affinities (eV). Two values are given if the lowest in energy SOMO is diffuse and has different symmetry than π*(b_1).

	6-31G(d)	6-311G(d,p)	6-31+G(d)	6-311++G(d)	aug-cc-pVTZ
Py	-1.68	-1.31	-0.93	-0.31 or -0.65	-0.35 or -0.85
2-ClPy	-1.16	-0.76	-0.55	-0.49	-0.49
2-BrPy	-1.11	-0.77	-0.5	-0.43	-0.42
3-ClPy	-1.16	-0.76	-0.53	-0.47	-0.46
3-BrPy	-1.11	-0.77	-0.48	-0.41	-0.4
4-ClPy	-1.18	-0.82	-0.52	-0.48	-0.44
4-BrPy	-1.11	-0.76	-0.41	-0.37	-0.36
Pz	-0.97	-0.67	-0.27	-0.22	-0.22
2-ClPz	-0.47	-0.17	0.10	0.15	0.14
2-BrPz	-0.41	-0.13	0.15	0.22	0.20

In the case of pyridine in the two biggest basis, the order of the orbitals is changed and the lowest energy SOMO has incorrect symmetry, values of VEAs to both orbitals are given in the table. It can be seen that the VEAs tend to converge to the fixed values with increasing basis set and that the 6-31+G(d) is sufficient, not problematic and compact at the same time.

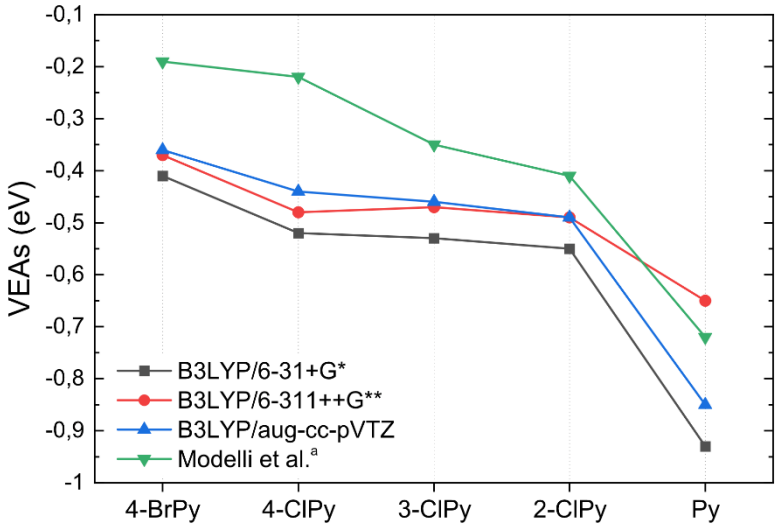

Fig. 3. Vertical electron affinities obtained in different basis sets comparing to the experimental data. [a]VEAs from [11] and [12].

Potential energy curves for pyridine, pyrazine, halopyrazines and 4-substituted pyridines, are shown in the Figures 4-6. Mulliken population analysis revealed, that if the bond C-X is stretched (X=H, Cl, Br), the extra electron rather resides on the ring, in case of pyridine and pyrazine, or on the halogen atom in substituted compounds, following the reactions from Eq. (2) and Eq. (3), respectively. Enthalpies of these reactions are listed in the Table 2 along with the equilibrium lengths of C-X bonds in neutral molecules. All the anion curves without symmetry constraints are qualitatively the same. They start with planar geometry and pi* state. Close to the intersection of the pi* and sigma* states, the states mix by the deviation of the C_n-X bond from the plane of the ring to about 40º, to finally form the σ* state of planar geometry and the molecule dissociates. The curves of pyridine and pyrazine are also quantitively similar, except that the curve of pyrazine anion lies very close to the neutral one. This is reflected in the results of other research groups showing the adiabatic affinity of pyrazine is close to zero (e.g. [13]). Formation of the $[Py\text{-}H]^-$ anion was observed at 2.5 eV by Ryszka and coworkers [14], so quite below the reaction threshold. Both dissociation to the σ* state and the π* state are highly energy unfavourable. According to calculations, anions of halopyrazines are stable with respect to the neutral molecule and dissociation products of the reaction in Eq. (2). Unfortunately, there is no experimental or theoretical data with which to compare that result. Halopyridines have negative vertical electron affinities and do not have a clear minimum in π* state. The minimum of σ* state is visible, but rather shallow. Formation of Cl^- and Br^- from 4-chloropyridine and 4-bromopyridine was observed by Modelli et al. [12] at 0.26 eV and 0.1 eV, respectively. This is in a good agreement with VEAs obtained by this group, indicating that the curve may be (almost) repulsive. Enthalpies of reaction in Eq. (3) are relatively small or negative for 2-substituted halopyridines and halopyrazines.

Tab. 2. Calculated parameters of the potential energy curves. AE is the activation energy (kcal/mol), r(C_n-X) is the equilibrium distance in the neutral molecule (Å) and ΔH (kcal/mol) stands for the enthalpy of reactions in Eq. (2) and Eq. (3).

	AE	r(C_n-X)	ΔH	
	6-31+G(d)	6-31+G(d)	6-31+G(d)	aug-cc-pVTZ
2-HPy	-	1.0887	86.4	86.4
3-HPy	-	1.0865	78.2	78.8
4-HPy	-	1.0872	76.1	76.7
2-ClPy	1.38	1.7622	-0.104	1.40
2-BrPy	0.00	1.9111	0.174	-7.69
3-ClPy	1.18	1.7536	3.20	4.97
3-BrPy	0.00	1.8986	4.17	-3.61
4-ClPy	0.00	1.7524	2.62	4.39
4-BrPy	0.00	1.8975	3.42	-4.41
Pz	-	1.0881	77.5	78.0
2-ClPz	5.78	1.7533	-0.763	0.763
2-BrPz	3.79	1.9019	-0.570	-8.21

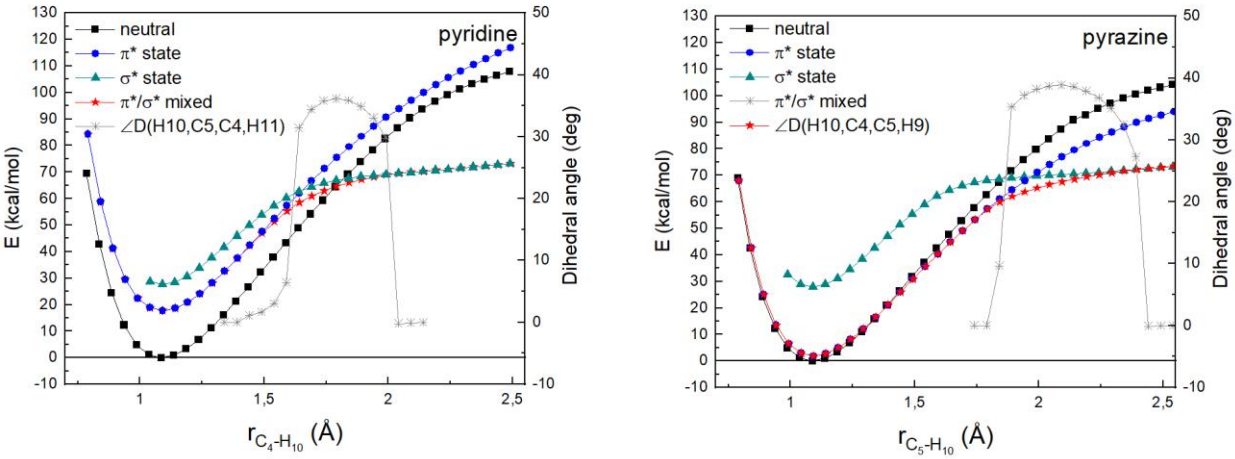

Fig. 5. Potential energy curves of pyridine and pyrazine. Numbering of atoms is in the Figure (2).

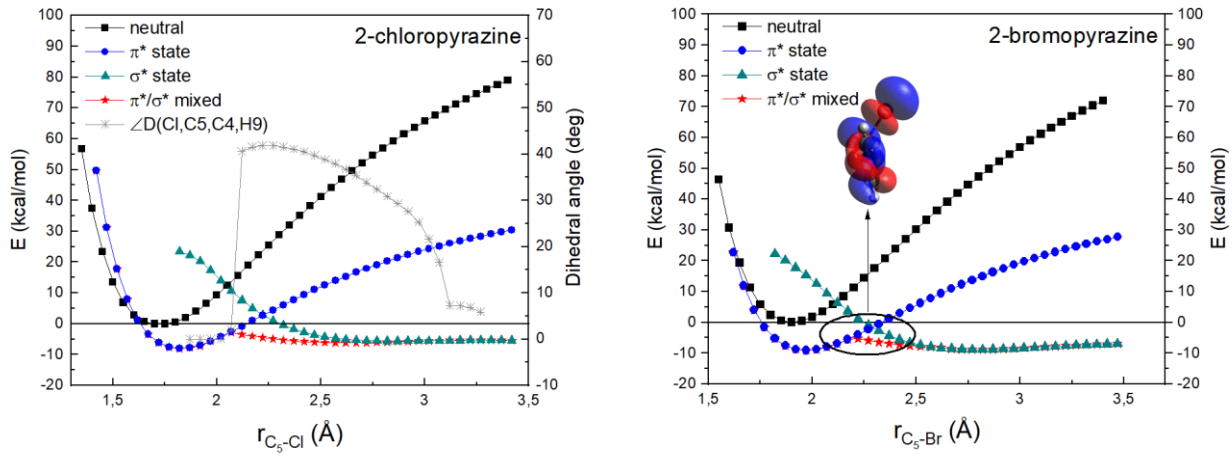

Fig. 4. Potential energy curves of halopyrazines. On the right the area of the bond bending is circled and the mixed π*/σ* orbital is shown.

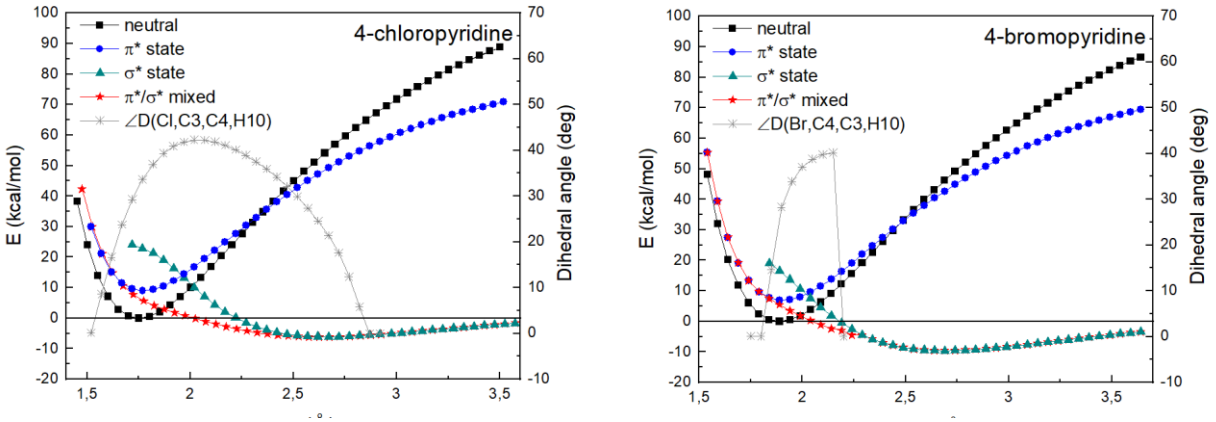

Fig. 6. Potential energy curves of halopyridines.

4. Summary

Determining the vertical electron affinity using the B3LYP functional with the basis set that includes diffuse functions can be an alternative to the more sophisticated ones, but the SOMO orbital should be carefully verified. According to calculations, pyrazine has a near-zero adiabatic electron affinity, halopyrazines form stable anions, whereas negative ions of pyridines are temporary. Dissociation of the investigated molecules goes through the symmetry breaking by bending of the dissociating bond, and therefore converting from the π* to σ* state. The curves of halopyridines may be almost repulsive. Dissociative attachment of the thermal electron for 2-substituted molecules is slightly endothermic or exothermic, while for pyridine and pyrazine molecules highly endothermic.

5. Acknowledgments

Calculations were carried out at the Academic Computer Centre in Gdańsk (TASK).

6. References

[1] Fabrikant I I, Eden S, Mason N J and Fedor J 2017, Recent Progress in Dissociative Electron Attachment: From Diatomics to Biomolecules, in: Advances In Atomic, Molecular, and Optical Physics, Vol. 66, edited by Arimondo E, Lin C C and Yelin S F, Academic Press, pp. 545-657
[2] Huth M, Porrati F and Dobrovolskiy O 2018 *Microelectron. Eng.* **185-186** 9
[3] Chen H-Y, Chen H-F, Kao C-L, Yang P-Y, Hsua S C N 2014 *Phys. Chem. Chem. Phys.* **16** 19290-19297
[4] Joshipura K, Mason N 2019, Applications of Electron Scattering, in: Atomic-Molecular Ionization by Electron scattering: Theory and Applications. Cambridge University Press, Cambridge, pp. 177-218
[5] Burke P G 2011, R-Matrix Theory of Atomic Collisions. Springer, Berlin, Heidelberg
[6] Winstead C and Mckoy V 1996 *Adv. Atom. Mol. Phys.* **36** 183
[7] Szarka A Z, Curtiss L A and Miller J R 1999 *Chem. Phys.* **246** 147
[8] Mishra P M 2015, *Comput. Theor. Chem.* **1068** 165
[9] McMurtry B M, Turner A M, Saito S E and Kaiser R I 2016 *Chem. Phys.* **472** 173
[10] Weber A L 2008 *Org. Life Evol. Biosph.* **38** 279
[11] Modelli A and Burrow P D 1983 *J. Electron Spectros. Relat. Phenomena* **32** 263
[12] Modelli A, Foffani A. Scagnolari F and Jones D. 1989 *Chem. Phys. Lett* **163** 269
[13] Mašín Z and Gorfinkiel J D 2011 *J. Chem. Phys.* **135** 144308
[14] Ryszka M, Alizadeh E, Li Z and Ptasińska S 2017 *J. Electron, Spectros. Relat.Phenomena* **147** 094303

LOW ENERGY ELECTRON ATTACHMENT TO COBALT TRICARBONYL NITROSYL MOLECULES AND CLUSTERS AND MIXED CLUSTERS WITH ACETIC ACID

Dušan Mészáros, Peter Papp, Štefan Matejčík

Department of Experimental Physics, Faculty of Mathematics, Physics and Informatics, Comenius University in Bratislava, Mlynská dolina, 842 48 Bratislava, Slovakia
E-mail: meszaros44@uniba.sk

We present low energy electron interaction studies of $Co(CO)_3NO$, widely used as a precursor in Focused Electron Beam Induced Deposition (FEBID) and in the alternative Electron Beam Induced Surface Activation (EBISA) technology. The electron attachment (EA) and dissociative electron attachment (DEA) of gas phase $Co(CO)_3NO$ will be compared to the DEA of $Co(CO)_3NO$ clusters and to mixed clusters with acetic acid. New resonances will be revealed in the recent results for pure clusters of $Co(CO)_3NO$, while the mixed clusters with acetic acid has been measured for the first time.

1. Introduction

Interaction of low energy electrons with molecules and molecular clusters is one of the elemental processes in plasma and plasma technologies. In our study we are focusing on electron attachment (EA) and dissociative electron attachment (DEA) on cobalt tricarbonyl nitrosyl ($Co(CO)_3NO$) and mixture of $Co(CO)_3NO$ with acetic acid (CH_3COOH). $Co(CO)_3NO$ is used as precursor gas in Focused Electron Beam Induced Deposition (FEBID) and Electron Beam Induced Surface Activation (EBISA) technology. In previous studies it was shown that deposition of Co layers from $Co(CO)_3NO$ works well with FEBID but not with EBISA [1,2]. The main difference between FEBID and EBISA is the procedure of deposition. FEBID is based on real-time deposition, high energy focused electron beam is used to draw structures on surface via direct interaction with the precursor gas. On the other hand, in EBISA technique the high energy focused electron beam is used to activate the surface and the precursor gas interacts only with the activated surface, not with the electron beam. In EBISA works [1,2] the metal-organic framework (MOF) HKUST-1 was used which consists from metallic atoms (copper) and as linker is used trimesic acid ($C_9H_6O_6$). Therefore in our recent study we focus on interaction of $Co(CO)_3NO$ with the carboxylic group of the MOF, however with acetic acid, considered as a simpler model of trimesic acid.

The CLUSTER-ILN experiment [3] (Fig. 1) was used to measure the electron molecular and cluster interactions, with a trochoidal electron monochromator (~200 meV measured at FWHM of the Cl^- peak from CCl_4 molecule) and quadrupole mass analyser for identifying the charged products of electron impact, both in a perpendicular orientation. We use external bottles to prepare the mixture of $Co(CO)_3NO$ and Ar gas, in this experiment ~33 mbars of $Co(CO)_3NO$ and ~10 bars of Ar was used. This mixture flows above the surface of liquid acetic acid placed in a container (optional), the mixed gasses are then expanding via 80 μm nozzle into the high vacuum (expansion chamber). The cooling of the gas via supersonic expansion produces a beam of molecular clusters which is then separated with the skimmer (0.8 mm) into the reaction chamber. EA and DEA were measured on $(Co(CO)_3NO)_mAr_k$ and $(Co(CO)_3NO)_m(CH_3COOH)_nAr_k$ clusters, electron molecular or cluster reactions relevant to our experiment are summarized below. With CLUSTER-ILN we can study the electron attachment to molecules (2_a), clusters (3) and (6) and corresponding dissociative electron attachment (reactions (2_b), (4), (5) and (7)-(10)).

$$e^- + AB \rightarrow AB^* + e^- \quad (1_a)$$
$$AB^* \rightarrow A^+ + B^- \quad (1_b)$$
$$e^- + AB \rightarrow AB^{-*} \quad (2_a)$$
$$AB^{-*} \rightarrow A\cdot + B^- \quad (2_b)$$
$$e^- + (M)_n \rightarrow (M)_n^- \quad (3)$$
$$\rightarrow X^- + R(M)_{n-1} \quad (4)$$
$$\rightarrow X^-(M)_{n-1} + R \quad (5)$$
$$e^- + M_mN_n \rightarrow (M_mN_n)^- \quad (6)$$
$$\rightarrow X^- + R(M_{m-1}N_n) \quad (7)$$
$$\rightarrow X^-(M_{m-1}N_n) + R \quad (8)$$
$$\rightarrow A^- + B(M_mN_{n-1}) \quad (9)$$
$$\rightarrow A^-(M_mN_{n-1}) + B \quad (10)$$

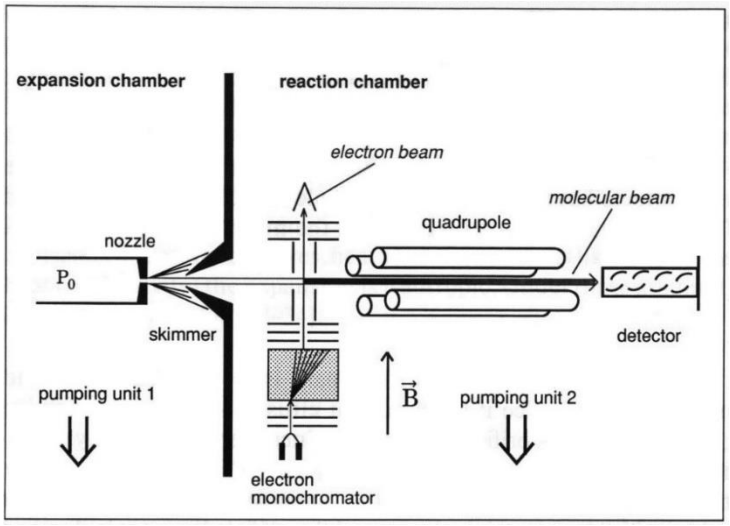

Fig. 1. The schema of CLUSTER-ILN experiment at the Comenius University in Bratislava (built at the Freie Universität Berlin [3]).

2. Dissociative electron attachment to $Co(CO)_3NO$ clusters

At the beginning of the presented studies we have performed the measurements of electron attachment to $Co(CO)_3NO$ clusters and compared these results with the previously published gas phase studies [4] and He droplet cluster studies [5], both are summarized in Table 1. All reported molecular fragments are in good agreement with gas phase works of Engmann [4] with few exceptions coming from cluster reactions and few differences with Postler [5]. The recent DEA studies to clusters vs gas phase revealed additional higher energy resonances for fragments $[Co(CO)_2]^-$, $[CoCONO]^-$, $[Co(CO)_2NO]^-$, and two higher energy resonances for fragment $[Co(CO)_3]^-$ (at 9.88 eV has similar shape to the resonance of the $[CoCONO]^-$ fragment at 9.94 eV). However, cluster fragments (>173 amu) reveal some differences from Postler's work [5], we assume it is due to different method of producing the clusters (co-expansion with Ar vs pick up to He droplet). The sensitivity to ionic products is higher in our work, we have nicely resolved the resonances of cluster fragments published previously in Postler's work [5], additionally with electron energies from 0 eV contrary to 2 eV in their work [5]. Common feature of cluster fragments is that multiple processes result in the same fragment. Cluster fragment can be created by several consecutive reactions because of a possibility of interaction between molecules in cluster. This is possible due to self-scavenging electrons. That means electron can scatter on first molecule in cluster, lose some energy and then interact with another molecule. That may result in higher number of resonances, some may be detected at higher energies as the kinetic energy of interacting electron is the sum of the attachment energy and the energy lost in scattering interaction.

We were able to detect cluster fragments up to 3 molecules of $Co(CO)_3NO$ in cluster. It is important to note that parent ion does not exist in gas phase and is only visible in cluster measurements. As a consequence of short molecular distances in cluster, energy released at formation of the molecular negative ion, can be distributed more efficiently within a cluster which results in stabilisation of parent ion contrary to the gas phase. Similarities and differences were observed in the energy spectra of cluster fragments in Fig. 2. M^-, M_2^-, $[Co_2(CO)_5(NO)_2]^-$, $[Co_2(CO)_4(NO)_2]^-$ have similar shapes of the ion yields but also some significant differences. First difference is the slight shift of the low energy resonance position, M_2^- has the maximum at 0.03 eV, $[Co_2(CO)_5(NO)_2]^-$ at 0.15 eV, M^- at 0.32 eV and $[Co_2(CO)_4(NO)_2]^-$ at 0.49 eV. Also the relative intensity of first and second resonance (~4.5 eV) differs for these fragments. While for M^- and M_2^- the first resonance is much more dominant, the second resonance becomes more significant for $[Co_2(CO)_5(NO)_2]^-$ and $[Co_2(CO)_4(NO)_2]^-$. In addition, M^- and M_2^- have one more resonance at higher energy at 10.3 eV and 11.9 eV respectively. $[Co(CO)_2NO]^-$ has resonances with similar shape to those of M^-, first resonance is split to two at 0.05 eV and 0.52 eV. For fragments with below m/z 145 (smaller than $[Co(CO)_2NO]^-$) the main resonance is shifting to higher energies with the increasing number of dissociated ligands. $[CoCONO]^-$ has its main resonance split to two at 2 eV, 2.8 eV and one more at 9.94 eV. $[Co(CO)_2]^-$ and $[Co(CO)_3]^-$ share second resonance at ~7 eV and $[Co(CO)_3]^-$ has one more at 9.88 eV similar to $[CoCONO]^-$. Next similarity is between $[Co_2(CO)_5NO]^-$ and $[Co_2(CO)_6NO]^-$. Shape of their resonances is almost identical with two exceptions,

relative intensity of resonances ~4.5 eV and ~7 eV is different and $[Co_2(CO)_5NO]^-$ have one additional weak resonance at 0.62 eV. $[Co_2(CO)_3NO]^-$ and $[Co_2(CO)_4NO]^-$ like previous pair has similar shape of resonances and $[Co_2(CO)_4NO]^-$ have two more weak resonances close to each other at 2.05 eV and 2.9 eV.

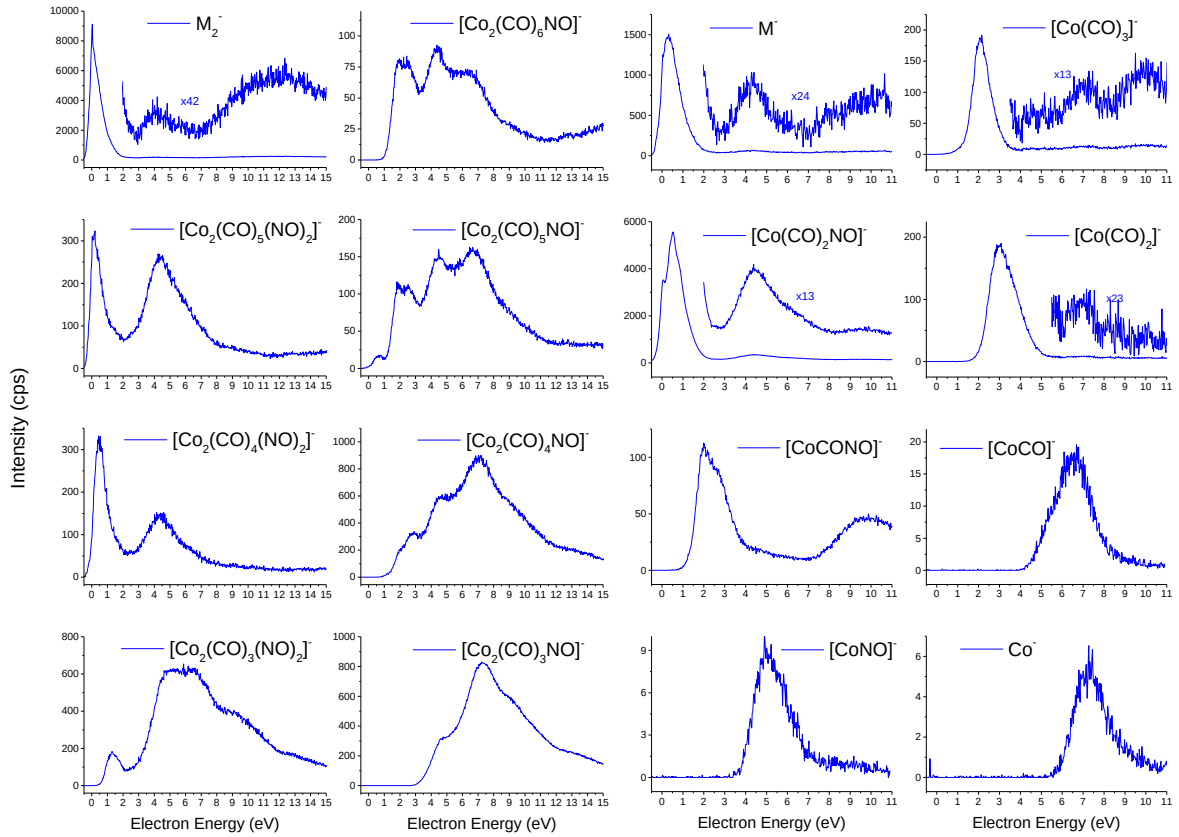

Fig. 2. Ion yield curves of $Co(CO)_3NO$ clusters and its DEA fragments.

Tab 1. Cluster DEA products of $Co(CO)_3NO$, peak positions of the resonances.

Ion	*m/z*	*Peak Position [eV]*		
		Gas ph. [4]	Clusters [5]	**CLUSTER-ILN**
Co^-	59	7.30	7.3	**7.30**
$[CoCO]^-$	87	6.50	6.5	**6.55**
$[CoNO]^-$	89	5.11	5.1	**5.07**
$[Co(CO)_2]^-$	115	2.99	2.9	**3.02, 6.96**
$[CoCONO]^-$	117	1.96, 2.55	2.3	**2.00, 2.80, 9.94**
$[Co(CO)_3]^-$	143	1.96	1.7, 2.3, 17.5	**2.05, 7.08, 9.88**
$[Co(CO)_2NO]^-$	145	0.02, 0.53	1.6, 4.1	**0.05, 0.52, 4.44, 9.8**
$[Co(CO)_3NO]^-$	173		5.8, 10.4, 14.9	**0.32, 4.30, 10.3**
$[Co_2(CO)_3NO]^-$	232		~10	**4.72, 7.22, 9.2, 13.1**
$[Co_2(CO)_4NO]^-$	260		~11	**2.05, 2.90, 4.63, 7.06, 9.2, 13.1**
$[Co_2(CO)_3(NO)_2]^-$	262		~11	**1.30, 5.10, 6.41, 9.2, 13.1**
$[Co_2(CO)_5NO]^-$	288		~9	**0.62, 1.94, 2.57, 4.47, 6.68, 8.8**

$[Co_2(CO)_4(NO)_2]^-$	290	~10	**0.49, 4.35**
$[Co_2(CO)_6NO]^-$	316	~12	**1.94, 2.56, 4.37, 6.22, 9.1**
$[Co_2(CO)_5(NO)_2]^-$	318	~13	**0.15, 4.37**
$[(Co(CO)_3NO)_2]^-$	346	~4, ~8, ~14	**0.03, 4.05, 11.9**

3. Dissociative electron attachment to mixed clusters of $Co(CO)_3NO$ and CH_3COOH

In this chapter we will discuss the effects of mixed clusters, acetic acid with $Co(CO)_3NO$. Most of the products of interaction between electron and mixed cluster are shown in Fig. 3, in the mass spectrum of this interaction at electron energy 3.9 eV. In the spectrum the same cluster fragments of $Co(CO)_3NO$ as in pure measurements are marked with brown, pure acetic acid clusters (pink) with the maximum 7 acid molecules in cluster are visible. In addition there are cluster fragments of $Co(CO)_3NO$ with number of acetic acid molecules attached (red). Introduction of acid into the mix caused creation of products which contained water (blue). This water originated from water contamination of acid and as by-product of creation of acetic acid clusters as was shown in Ferreira Da Silva's work [6]. Interesting pattern has been detected for the parent ion $(Co(CO)_3NO)^-$ with number of acid molecules attached, from one molecule all the way up to five (green).

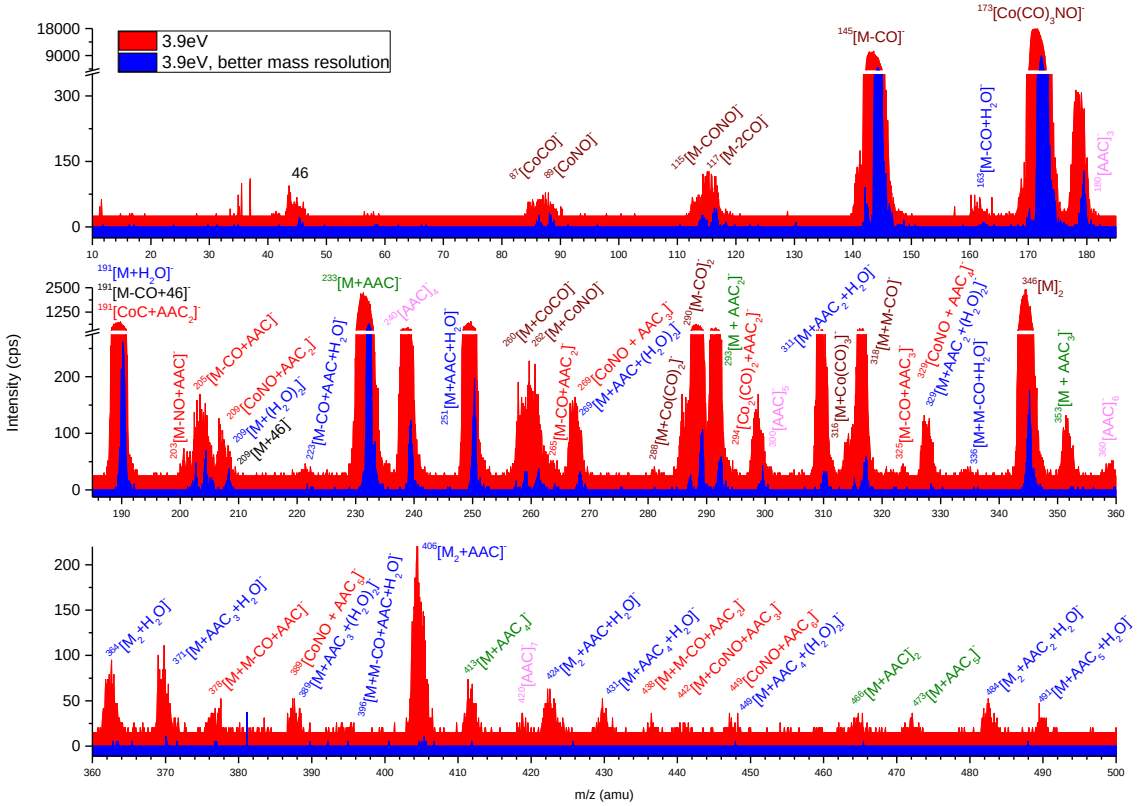

Fig. 3. Mass spectrum of mixed clusters of $Co(CO)_3NO$ and acetic acid at electron energy 3.9 eV.

Further investigation result on left side of Fig. 4. On these energy dependence spectra, the effect of increasing number of acid molecules in cluster with the parent ion is visible. Spectra look almost identical with few exceptions, one of which is slight shift of main resonance from 0.46 eV at zero acid molecules to 0.86 eV at one and more. The ~0 eV resonance becomes more significant as the intensity of the main resonance decreases with the number of acids. Second difference is decreasing intensity of resonance at ~4 eV with increasing number of acid molecules in cluster. It seems that the presence of acid in cluster closes that channel of the parent ion. This is evident in the spectrum of fragment $Co(CO)_2NO^-$, we can compare its spectrum of pure $Co(CO)_3NO$ clusters, of mixed clusters and even

more with one molecule of acetic acid attached. Result of this comparison is on the right side of Fig. 4. When acetic acid was present in the chamber but not in the product itself it slightly amplified the resonance at ~0 eV and opened an additional resonance channel at ~8 eV (blue vs red on Fig. 4 right). On the other hand, when acid molecule was part of the product, resonance at ~0 eV was totally suppressed and the main dominant resonance at 0.49 eV was suppressed to level of 4.5 eV resonance and shifted to 0.72 eV.

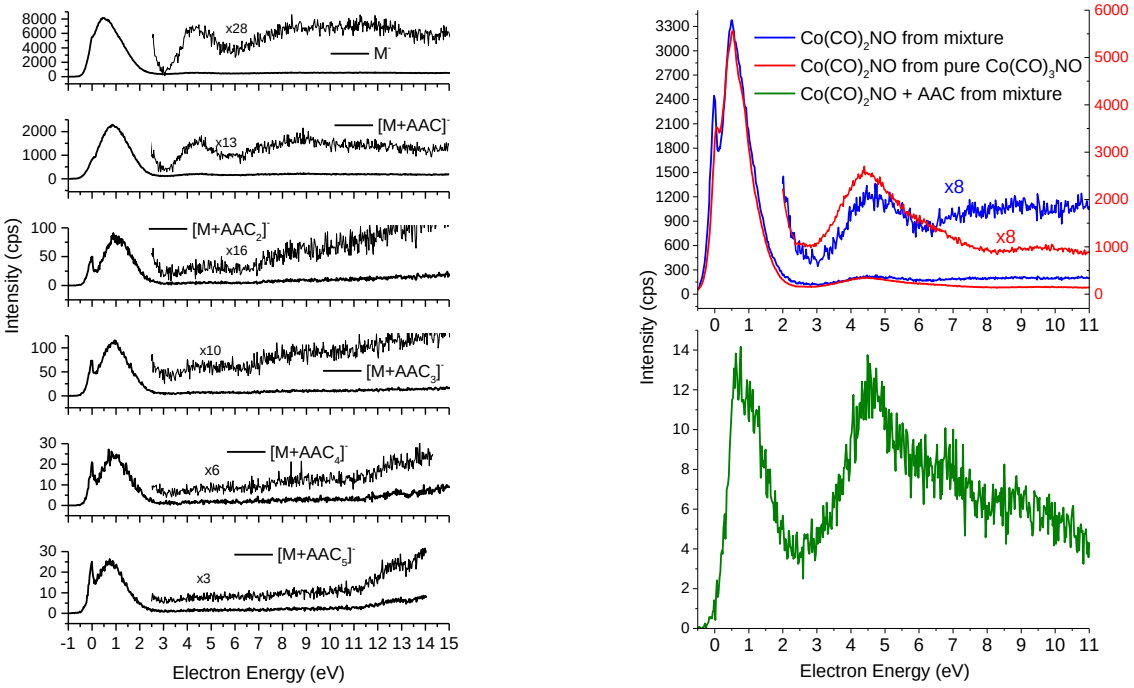

Fig. 4. Evolution of energy dependence of parent ion $(Co(CO)_3NO)^-$ (M) creation with increasing number of acetic acid (AAC) molecules in cluster (left). Difference between energy dependence of $Co(CO)_2NO^-$ fragment creation with (right, blue line) and without (right, red line) presence of acetic acid in chamber and with acetic acid in cluster (right, green line).

4. Conclusion

The electron attachment and dissociative electron attachment to pure $Co(CO)_3NO$ clusters and mixed with acetic acid were performed. We have found a good agreement of the pure $Co(CO)_3NO$ cluster results with previously published gas phase data with few exceptions. Many differences were found in comparison of cluster data with previously published due to different method of cluster creation. Parent ion was seen in cluster measurements which does not exist in gas phase because of excess energy released by negative ion creation. Many resonances were spotted in energy dependence spectra of cluster fragments. This was caused by self-scavenging electrons which one electron will interact with first molecule in cluster, lose some energy and then attach to second molecule in cluster.

The electron attachment and dissociative electron attachment to mixed clusters of $Co(CO)_3NO$ and acetic acid were performed for the first time. Except expecting fragments from both molecules, mixed cluster fragments were detected containing fragments of $Co(CO)_3NO$ with one or more acetic acid molecules or with water molecules. Slight shift of main resonance and decreasing intensity of resonance at ~4 eV of parent ion with increasing number of acid molecules was observed. Similar effect was observed on $Co(CO)_2NO^-$ fragment.

5. Acknowledgments

This project has received funding from the European Union's Horizon 2020 research and innovation programme under grant agreement No 692335. This work was supported by the Slovak Research and Development Agency contract no. APVV-19-0386 and the Slovak Grant Agency for Science contract no. VEGA 1/0733/17.

6. References

[1] Ahlenhoff, K., et al., *J. Phys. Chem. C*, **122**, (2018), Pages 26658-26670
[2] Drost, M., at al., *ACS NANO*, **12**, (2018), Pages 3825-3835
[3] Ingolfsson, O., Weik, F., Illenberger, E., *Int. J. Mass. Spec.*, **155**, (1996), 1.
[4] Engmann, S., et al., *J. Phys. Chem.*, **138**, (2013), 044305.
[5] Postler, J., et al., *J. Phys. Chem. C*, **119**, (2015), Pages 20917-20922
[6] Ferreira Da Silva, F., et al., *Phys. Chem. Chem. Phys.*, **11**, (2009), Pages 11631-11637

NEGATIVE ION MOBILITY SPECTROMETRY FOR MEASURING ELECTRON ATTACHMENT RATES

Izabela Wolańska[1], Edyta Budzyńska[1], Jarosław Puton[1]

[1]*Faculty of Advanced Technologies and Chemistry, Military University of Technology, Poland*
E-mail: izabela.wolanska@wat.edu.pl

1. Experimental and Theoretical Study

Ion Mobility Spectrometry (IMS) is an analytical method based on the movement of ions in gases. The sensitivity of the IMS depend on the effectiveness of the substance ionization, which may be increased by changing various measurement parameters, such as a shutter grid opening time, changes in temperature, or the presence of admixtures in gases flowing through the detector. Due to the selective detection of trace amounts of substances and a short time analysis, IMS is used mainly in the detection of chemical warfare agents, toxic substances and explosives materials [1].

Our work is devoted to the study of fundamental phenomena related to the operation of the IMS detector in the negative mode, in which ionization of the sample components occurs through electron capture (EC). This way of ionization is possible when nitrogen is the carrier and drift gas in the detector [2]. The IMS detector can be used not only as analytical tool but also to derive the basic parameter describing the EC - the capture rate constant. In these studies appropriate measurement systems are used for the introduction of samples into the drift section. The results of the experiments are drift time spectra containing characteristic signals. This group of methods, known as SWARM techniques, uses the interaction of swarm of ions or electrons with analyte molecules in gases [3,4].

The main aim of our research was to determine the optimal methods and parameters for conducting the SWARM experiment in the IMS detector. The tests were performed for two exemplary analytes: benzyl and benzal chlorides.

2. References

[1] G. A. Eiceman, Z. Karpas, H. H. Hill Jr., *Ion Mobility Spectrometry, CRC Press, Boca Raton*, (2014).
[2] E. Budzyńska et al.,, *Ion mobility spectrometers and electron capture detector – a comparison of detection capabilities, Talanta*, **194** (2019) 159 – 165.
[3] M. Tabrizchi, A. Abedi, *A novel use of negative Ion mobility spectrometry for measuring electron attachment rates, J. Phys. Chem. A* **108** (2004) 6319–6324.
[4] H. Feng, et al., *Rate constants of electron attachment to chlorobenzenes measured by atmospheric pressure nitrogen corona discharge electron attachment ion mobility spectrometry, Int. J. Mass Spectrom*. **305** (2011) 30 – 34

PRELIMINARY RESULTS ON QUANTITATIVE GC-IMS ANALYSIS OF ARABICA AND ROBUSTA COFFEES IN MIXES

Kateryna Trach[1], Oleksandr Prystopiuk[1], Martin Sabo[2], Štefan Matejčík [1, 2]

[1]*Department of Experimental Physics, Comenius University, Bratislava, Slovak Republic*
[2]*MaSaTech s.r.o., Sadová 3018/10 91501 Stará Turá, Slovak Republic*
E-mail: trach1@uniba.sk

We have applied MCC-GC-IMS (Multicapillary - Column-Gas-Chromatography - Ion Mobility Spectrometry) technique to qualify the composition of the coffee samples. In total 41 coffee samples were processed and analyzed, (22 samples Arabica, 8 Robusta, and 11 mixtures). Machine learning (ML) and chemometrics methods were applied to the 2D MCC-GC-IMS spectra of the samples. We have achieved 96% accuracy of the composition prediction, which is sufficient value for practical application.

1. Introduction

Coffee is among the most popular beverages worldwide and simultaneously coffee market belongs to the biggest agricultural markets (82,441.77 million U.S. dollars of worldwide revenue in the year 2019) [1]. According to International Coffee Organization [2], the EU consumption of coffee in the year 2019 was about 45 million bags (one bag is equivalent to 60kg).

Over the last decade, consumers' habits towards coffee have changed significantly. Nowadays so-called "third wave" of coffee culture is observed [3]. It can be characterized by the process of coffee transformation from a regular commodity to a valuable handicraft product. This is manifested in form of emergence of the small roasteries and coffee shops, where unique mixes with emphasis on the recognized region of the beans origin and the author's recipe of mixing/brewing are created [4].

Despite habit changes, general consumer behavior remains the same: the most important demand is to get a high-quality product. Studies have investigated factors that can be considered as subjective indicators of quality thus can stimulate or limit coffee consumption and purchase. There is evidence that two main groups of such factors are "sensory preferences" and "functional motives" [5]. The former includes sensory qualities of coffee: taste and smell, while the latter group comprises positive emotions, feeling of being aroused, focused mental state, etc. In terms of objective qualities, both groups of factors are related to the chemical composition of ground coffee that is used to brew the beverage. Sensory qualities are provided by the specific aroma of volatile organic compounds (VOCs), while flavor depends on substances that are extracted from coffee powder with boiling water. Finally, functional motives are fully related to the quantity and bioavailability of caffeine contained in the beverage. Keeping this in mind, coffee quality can be assessed with modern analytical techniques. For instance, laser-induced-breakdown spectroscopy [6], high-performance liquid chromatography [7], gas chromatography [8] were reported to be successful in the analysis of coffee in different forms.

Considering the aforementioned change, the quality assessment remains an issue, especially at coffee shops and roasteries that do not belong to retail networks thus have no access to quality control laboratories. Obviously, such small enterprises can not utilize above stated techniques due to the high cost of equipment and the need for highly-qualified personnel to operate it and to interpret the results. Very few options remain to provide high-quality coffee: either to purchase directly from trusted farmers or believe to the label information provided by gross retailers. Unfortunately, both have been found unreliable. Fraud in coffee mixes is a widespread problem [8-10]. In the most often case Arabica is replaced with more cheap Robusta species. Due to the huge difference in compounds in these species, a poor mix affects beverage quality, alters its taste and aroma.

The ion mobility spectrometry (IMS) method is successfully used for VOCs identification. IMS has numerous advantages due to which it shows a significant growth in use over the last decade. In particular, it is used for the characterization of VOCs in coffee [7, 11]. The method needs very simple sample preparation and no consumables are needed. Also modern IMS devices are table-top or portable and have a reasonable price. However, IMS spectra interpretation demands special knowledge and identification of individual peaks with reference compounds. As was mentioned before, this drawback limits the use of the method in small enterprises.

The presented investigation aimed to find out whether the software based on the machine learning approach can determine the quantitative composition of coffee powder mix containing various proportions of Arabica and Robusta species. In the case of satisfactory performance, such software may eliminate the need for IMS spectra interpretation. With this IMS analysis of coffee mixes may become attractive for small coffee-focused enterprises.

2. Materials and Methods

Total 41 samples were processed and analyzed. Among them 22 samples were pure Arabica species, 8 were pure Robusta and 11 were mixes. Most of the samples were originally in form of roasted beans in various packages of 100-250g weight. Beans were ground by an electric grinder. Mixes that were used in the experiment were created by adding 10-90% (by mass) of Robusta to 90-10% of Arabica. Each mix contained a single kind of each species.

To perform headspace sampling 1.0g of freshly ground coffee in form of powder was put into a 5ml glass vial. Afterward, the vial was heated in the oven at 90 °C for 20 minutes. 2.25ml of headspace vapor was automatically sampled and introduced into the MCC-GC-IMS injector with a maintained temperature of 132 °C. All samples were analyzed by MCC-GC-IMS Peakmachine (MaSaTECH, SK) [12], which consists of the automatic sampler, MCC-GC column, and IMS device. The device was pre-set as follows: drift tube temperature 100°C; drift gas flow was 700 ml/min, sample speed was 30 ml/min and injection speed was 100 ml/min.

All spectra were measured in positive polarity. In total, 41 ion mobility spectra and 41 2D maps were obtained. For spectra visualization and processing MaSaTECH data post-processing software was used [13]. Analysis of obtained spectra was performed with Chemometrics software [13]. It has several machine learning functions that can be used for unknown IMS spectra classification. Random forest architecture (a kind of neural network that is often used in solving classification problems) was used in the present investigation.

3. Results

Original 2D spectra of Arabica and Robusta (Fig.1, b) have differences in peak positions, its intensity, and some peaks are absent. For the relevant example, one can see the 2D IMS spectrum of pure Arabica (Fig.1, a) and pure Robusta (Fig.1, b).

However, it is hard to find out the mix composition from the 2D spectrum (Fig.2, c). Because of this obtained spectra were classified by random forest method provided in the program Chemometrics. As can be seen from Tab. 1, where the part of analyzed mixes is specified, the classification of samples is accurate enough. The accuracy average was 0.96, which is sufficient for practical application. For instance, the mixture containing 90% of Arabica and 10% of Robusta was predicted as 89.9% of Arabica and 10.1% of Robusta. For other entries in the table i.e. for other coffee mixes relevant results also were obtained. The lowest matching value among the presented results is 70.4% against the real value of 90%. This may be due to the geographical origin of the coffee, as the other two coffee samples of this brand, showed higher Arabica content than was actually blended: the revealed value of 83.3% against real content of 80% and revealed value 85% against real content of 80%, respectively.

Tab. 1. Results of the coffee samples classification.

Given composition		Composition revealed with ML	
90% Arabica Bozin Brazil	10% Robusta Caffe Gourmet India	89,9% Arabica Bozin Brazil	10,1% Robusta Caffe Gourmet India
80% Arabica Bozin India	20% Robusta Hardy 3 countries	83,3% Arabica Bozin India	16,7% Robusta Hardy 3 countries
80% Arabica Bozin Guatemala	20% Robusta Trieste	85% Arabica Bozin Guatemala	15% Robusta Trieste
20% Arabica Trieste	80% Robusta CP Guatemala	14,4% Arabica Trieste	85,6% Robusta CP Guatemala
20% Arabica Trieste	80% Robusta CP Guatemala	14,4% Arabica Trieste	85,6% Robusta CP Guatemala

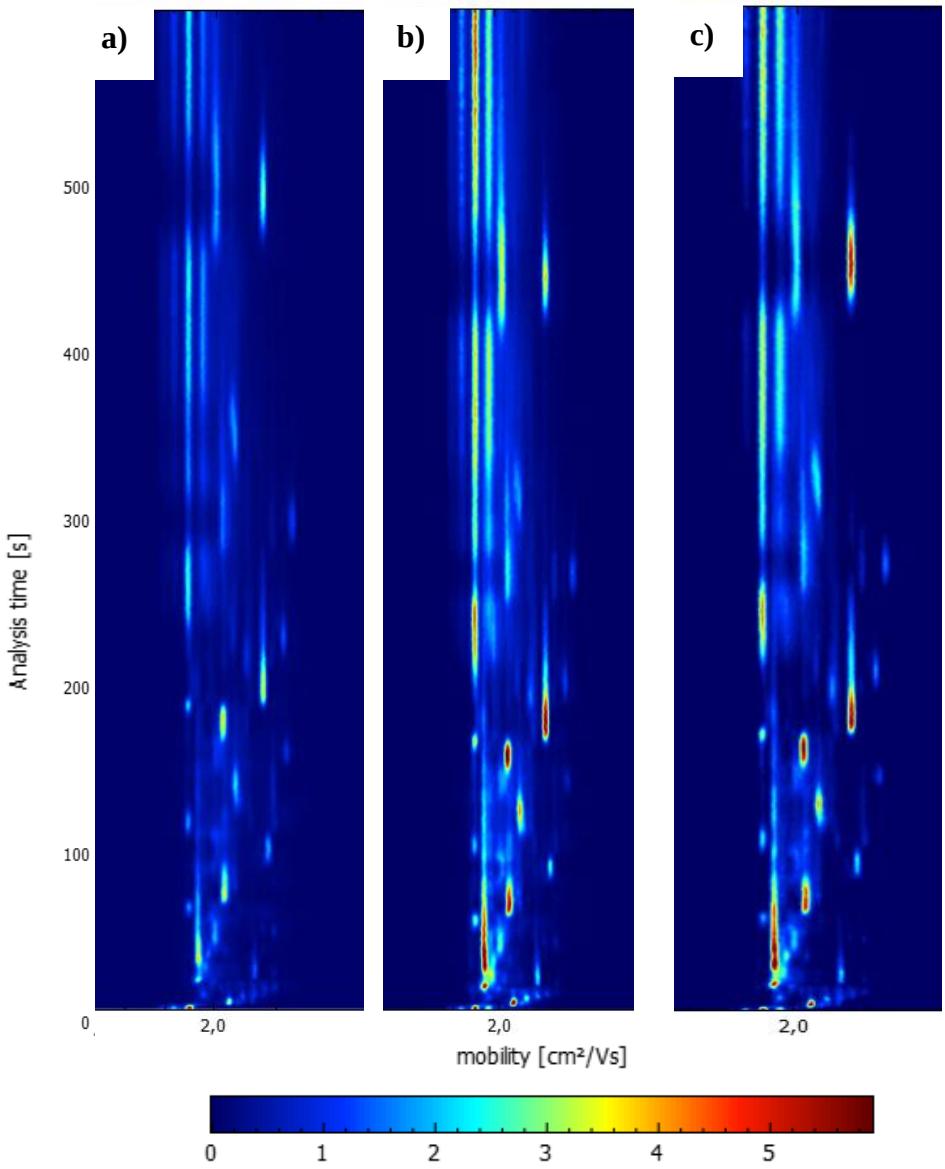

Fig.1. 2D MCC-GC-IMS spectra of VOCs in ground coffee: a) pure arabica (Bozin, Brazil), b) pure robusta (Caffe Gourmet, India), c) Arabica/Robusta mixture (90% Arabica Bozin Brazil and 10% Robusta Caffe Gourmet).

4. Conclusion

MCC-GC-IMS method was used for ground coffee analysis. Due to the method features it was possible to perform the analysis with very little sample preparation, namely with only grinding of roasted beans followed by pouring of the powder to vials. The method is sensitive enough, so meaningful IMS spectra can be obtained by the sampling of VOCs from the vial headspace.

Furthermore, two-dimensional IMS spectra were successfully analyzed by the original software featured with ML algorithms. Application of random forest architecture allowed obtaining average accuracy of 0.96% in the determination of Arabica-Robusta composition in ground coffee mixes. Inclusion of this kind of software to IMS device software bundle could eliminate the need for the employment of skilled professional for the analysis results interpretation. Taking this into consideration, the IMS method may become easy-to-use and cost-effective thus attractive to small coffee-related enterprises. Moreover, it may become a key factor in guaranteed client satisfaction by uncompromised quality of coffee products.

5. References

[1] Oloruntoba A (ed.) 2020: https://www.statista.com/forecasts/758662/revenue-of-the-coffee-market-worldwide-by-country
[2] International Coffee Organization 2020: http://www.ico.org/trade_statistics.asp
[3] Manzo J 2014 *Journal of Arts and Humanities* **3** 8.
[4] Carvalho N B, Minim V P R *et al.* 2015 *Food Research International* **77** 400–407.
[5] Samoggia A and Riedel B 2018 *Appetite* **129** 70–81.
[6] Zhang C and Shen T 2017 *Sensors* **18** 1.
[7] Caporaso N, Whitworth M B *et al.* 2018 *Food Research International.* **108** 628–640
[8] Pauli E D and Barbieri F 2014 *Food Res. Int.* **61**
[9] Dias R C and Valderrama P 2018 *Food Chem.* **255**
[10] Preedy V R (ed.): Coffee in Health and Disease Prevention 2015 *Academic Press*.
[11] Konieczka P P, Aliaño-González M J *et al.* 2020 *Sensors.* **20** 3123.
[12] MCCGC-AIMS PeakMachine infopage; https://www.masatech.eu/peakmachine
[13] MaSaTECH control software; https://www.masatech.eu/control-software

Chairman of the session: Satoshi Hamaguchi

SHAFTLESS SCREW DIELECTRIC BARRIER DISCHARGE CONVEYOR FOR TREATMENT OF RECYCLED PET FLAKES

Martina Ilčíková[1], Samuel Kramár[2], Ladislav Hustý[1], Jozef Ráheľ[1]

[1] *Masaryk University, Faculty of Science, Department of Physical Electronics, Kotlářská 2, 611 37 Brno, Czech Republic*

[2]*Mendel University, Faculty of Forestry and Wood Technology, Department of Wood Science and Technology, Zemědělská 3, 61300 Brno, Czech Republic*

E-mail: ilcikova@mail.muni.cz

A design of dielectric barrier discharge plasma source suitable for treatment of bulk materials is described. The design is based on shaftless screw conveyor. It combines both the surface and volume dielectric barrier discharge and operates at atmospheric pressure. Rotational movement of shaftless spiral helps transporting and simultaneously mixing particulate material through the discharge zone. The machine was tested on plasma treatment of PET flakes in order to increase its surface free energy. To optimize the parameters of plasma treatment the measurement of chemiluminescence signal was used. Plasma treated PET flakes were used as an additional filler of wood-based particleboards. Particleboards containing plasma treated PET flakes showed substantially better mechanical properties than composite particleboards containing non-treated PET flakes.

1. Introduction

The increasing amount of plastic waste together with vexing problems of its environmentally-friendly disposal result in necessity to look for the new options of recycling. With respect to plastics, polyethylene terephthalate (PET) represents a significant fraction of total amount of plastic waste [1], chiefly due to its popularity in bottling industry. One of the recently tested possibilities for recycling PET bottles was use them as an additive or filler in new composite materials. In [2] authors list a number of published works dedicated to studies PET particles addition into concrete, e.g. to reduce final concrete density. In [3] properties of wood particle boards involving PET flakes fraction were investigated. The addition of PET flakes improved boards' water resistance (i.e. it reduced thickness of swelling and absorption), but on the other hand it also reduced their mechanical properties. This problem of particle board mechanical properties deterioration was successfully resolved in [4], where PET flakes were plasma activated (Fig. 1) by diffuse coplanar surface barrier discharge (DCSBD), which improved its adhesion to the used urea-formaldehyde adhesive.

The DCSBD has proved itself to be an effective tool not only for plasma treatment of the materials with well-defined flat surfaces (glass, foils, wood etc.) [5-7], but also for plasma treatment of powder material with non-uniform surface (powders, fibres or seeds) [8-10]. However, the DCSBD treatment of powders and bulk materials suffers in general by its low volume throughput. This originates from a poor contact of DCSBD generated plasma with multiform shapes of treated particles. To achieve a satisfactory treatment level of PET flakes, only a single layer of treated flakes (approx. 2-5 g in one batch) had to be uniformly spread on the discharge plate and stirred during the treatment (Fig. 1). After some treatment time flakes were swiped away out from the discharge plate and this process was repeated for many times. Although this way of powders-like materials plasma treatment is sufficient in laboratory scale, for actual commercial use one needs to consider a different way of plasma treatment, suitable for substantially higher throughput. Still, it is necessary keep the advantageous features of DCSBD such as its low temperature (suitable for thermally sensitive materials) or operation at atmospheric pressure (to avoid expensive vacuum system).

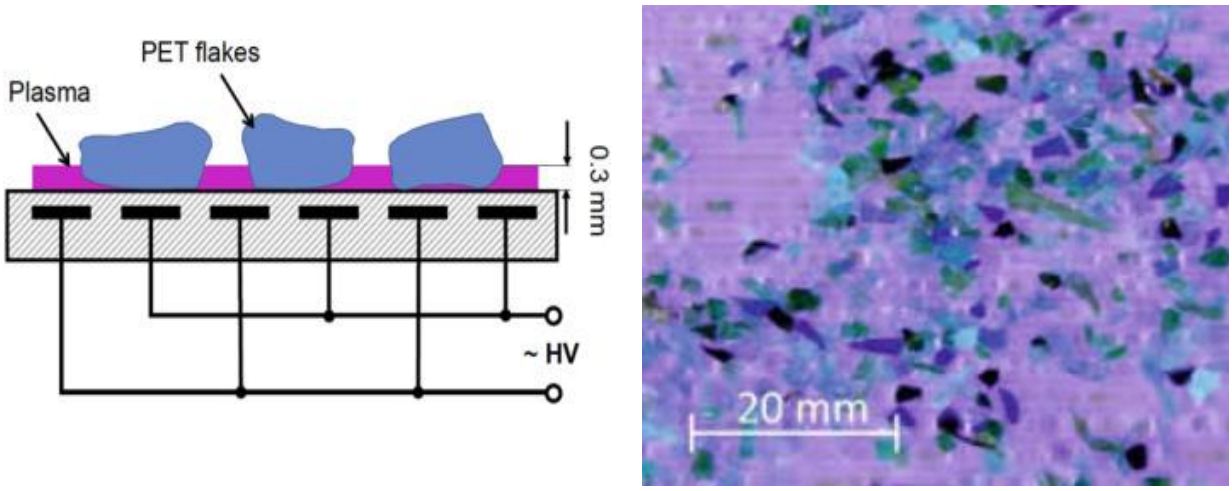

Fig. 1. PET flakes plasma treated on DCSBD [1].

In this work we will report on our attempt to up-scale the promising results of [4] into substantially higher throughput. To solve the problem of low surface energy of PET flakes we designed a new plasma source. A novel type of dielectric barrier discharge (DBD) reactor involving shaftless screw as a discharge electrode was constructed and tested for its performance [11]. Several kilograms of PET flakes were plasma activated, and used to prepare composite wood particle boards. Afterwards the obtained mechanical properties were evaluated. To analyse the level of PET flakes surface activation a method of chemiluminescence measurement was tested and evaluated.

2. Experimental setup

The schematic view and actual photograph of shaftless screw DBD conveyor are shown in Fig. 2 and 3 respectively. The system contained two coaxial dielectric tubes and three electrodes. The first electrode – conveying shaftless spiral (2) was made of stainless-steel compression spring wire of 1.5 mm wire diameter. It was centrally placed inside the inner dielectric tube (1) of 25 mm inner diameter, 2.5 mm wall thickness and 50 cm length. The spiral electrode was attached to IKA RW16 overhead stirrer which served as driving motor (3). Rotation motion of the electrode provided a transversal motion of treated bulk material. The use of spring wire was found to be beneficial due to its low friction with the thin wall of inner dielectric tube (1). Second and third driving copper electrodes (3a, 3b) were taped outside of the inner dielectric tube. These were galvanically connected to high voltage (HV) power supply of 150 W, 15 kHz, 10 kV. The central electrode (2) was on floating potential resulting from the capacitive coupling with driving electrodes 3a, 3b. In this way, no mechanically rotating HV connector to the central electrode was necessary. Actual view of generated discharge plasma is shown in Fig. 4. The machine was designed to sustain the continual regime of operation. Therefore the system had to be cooled. In this particular case the oil was flowing between inner and outer dielectric tube. Dosing of material and actual treatment time was regulated by slowing/fastening the rotational speed of shaftless spiral. To secure a good quality of plasma treatment without any thermal degradation of PET, each batch of treated material went through the discharge area three times. An average treatment time for simple passage was 10 sec. Actual volume throughput (with the account of triple passage) of tested apparatus was 5 g/min.

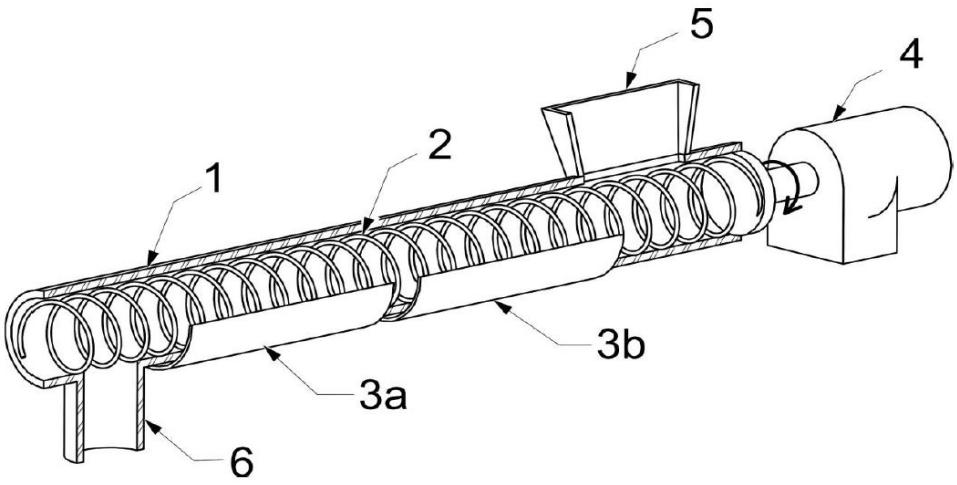

Fig. 2. Schematic of shaftless screw DBD plasma conveyor. 1 – dielectric tube, 2 – inner screw metal electrode, 3 – outer HV copper electrodes, 4 – driving motor, 5 – feed container 6 – output container [11]

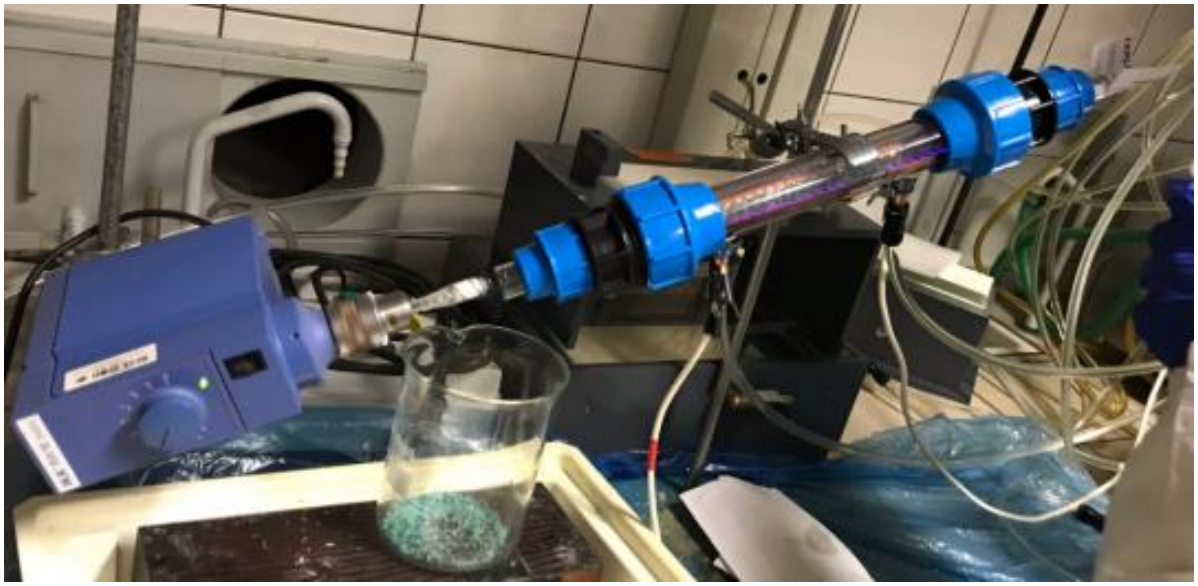
Fig. 3. Photo of shaftless screw DBD plasma conveyor.

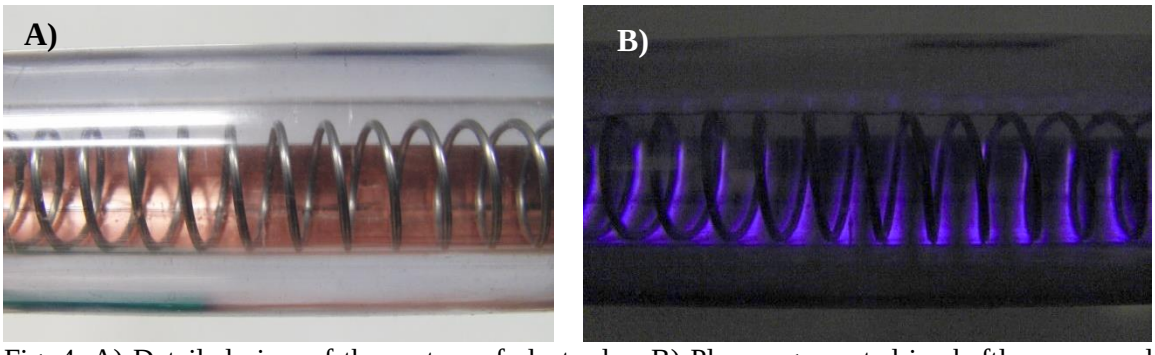

Fig. 4. A) Detailed view of the system of electrodes. B) Plasma generated in shaftless screw plasma conveyor

To optimize the treatment parameters of shaftless screw DBD conveyor the evaluation of chemiluminescence (CL) signal of PET flakes was used as a rapid assessment tool. The level of CL

signal is proportional to number density of surface hydroperoxyl groups [4], which is one of the providers of higher chemical reactivity of plasma treated surface. The parameters of plasma treatment (number of passages, input power as well as the rotation speed of spiral) were altered until the intensities of CL signal were comparable with those of PET flakes treated by DCSBD in [4]. The CL optical signal was detected by Lumipol 3 (LUMIPOL Technologies, Slovakia). For the CL measurement a small amount of examined sample (m=0.02 g) was placed into aluminium sample holder (Fig. 5) and heated linearly up to 120°C.

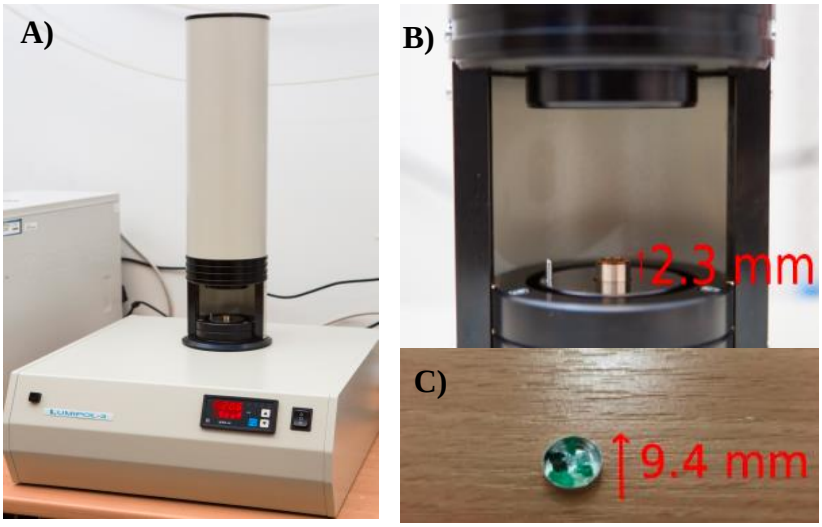

Fig.5. A) Lumipol 3 B) Heated chamber for samples C) Sample holder

Last part of our applied research was aimed at manufacturing wood partlicleboards filled with PET flakes modified with plasma (Fig. 6). Firstly PET flakes (PETKA CZ, Czech Republic) were separated according to the size of its fraction on mesh strainers. After the separation, wooden particles (standard mixture for partlicle boards containing spruce and recycled wood) and the same size PET flakes were glued together with urea formaldehyde (UF) resin. Last technological step was to create the particleboards by pressing the glued mixture (Fig. 6A). During this step the pressure was applied in four phases each lasted 45 s. We started with the pressure 5 MPa and decreased gradually to 3.5 MPa, 2 MPa and 0.5 MPa. The mass fraction of individual components was 20% - 73% - 7% for PET flakes, wood chips and glue, respectively.

Fig.6. A) Manufacturing of the particleboards B) Particleboard with plasma treated PET flakes

3. Results and discussion

Typical chemiluminiscence curve is shown in Fig. 7. We can see that the curve picturing the reference sample (black one) has its maximum values around 100 counts. Plasma treatment in DCSBD (pink) induced surface changes which resulted in 6-times higher maximum intensity. To approach these values of CL signal by shaftless screw plasma conveyor treatment, samples needed to pass the discharge zone for 3 times (blue).

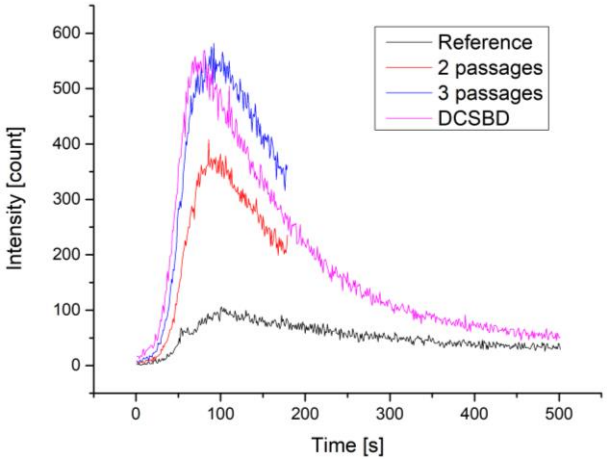

Fig.7. Measurements of CL signal comparing the treatment of PET flakes with shaftless screw plasma conveyor with DCSBD treatment

Tab. 1. Mechanical properties of particleboards (PB).

Sample	Bending strength [MPa]	Young's modulus [MPa]
pure PB	5.4	1124
(1 mm) PB + REF PET	2.2	508
(1 mm) PB + PT PET	4.1	909
(1 mm + 2 mm) PB + REF PET	1.8	425
(1 mm + 2 mm) PB + PT PET	4.3	943
(2 mm) PB + REF PET	1.6	412
(2 mm) PB + PT PET	5.2	1063
(OR) PB + REF PET	1.0	227
(OR) PB + PT PET	5.6	1135

To test our plasma conveyor milled PET flakes with different average size were used. Plasma treated (PT) PET flakes as well as PET flakes without plasma treatment (REF) were used as additive to wooden particleboards (PB). We worked with different size of PET flakes separated by system of mesh strainers. Dimensions of used PET particles (in mm) are marked in brackets while OR means that samples were prepared from the original mixed PET flakes (not separated according size).
Mechanical characteristics were evaluated by providing three-point bending test according to EN 310. Bending strength and Young's modulus of finals products in comparison with particleboards without additive (in Table 1. marked as PB) are summarized in table 1.

As-received milled PET flakes contain certain amount of milled paper and plastic foils coming from labels and etiquettes. This light fraction could have negative impact on the characteristics of final products as well as on process of the plasma treatment. All data listed in Table 1. represent the particleboards made of PET flakes from which the light fraction was not removed before the plasma treatment.

As it was expected, adding non-treated PET flakes into particleboards resulted in deterioration the mechanical characteristics of final products in all tested samples. In actual number original bending strength of 5.6 MPa was reduced to 2.2 MPa (for 1 mm flakes) or even more to 1.0 MPa for original PET flakes. On the contrary particleboards containing plasma treated PET flakes showed mechanical characteristics comparable with those without any PET addition. The final characteristic of the product is usually influenced by its inner structure. Therefore we assumed that mixing different sized PET flakes to the particleboards would result in different mechanical properties. This study showed slight differences between composite particleboards made of different size PET flakes. According to our results the larger the flakes are the higher bending strength is, as flakes of 2 mm showed the best results. This observation shall be closely examined in our next research, since the presented novel DBD discharge setup is particularly suitable for the treatment of larger particles.

4. Conclusion

New type of plasma source based on combination of surface and volume dielectric barrier discharge for plasma treatment of particulate materials was presented. Previous time consuming and operator-needed method plasma treatment was replaced by screw plasma conveyor. Thanks to continual operation mode presented source is more suitable for treatment much larger amount of material in shorter time and lower power input. In our pilot experimental set-up the reported DCSBD volume throughput of 5 g/min [4] was reproduced but at almost 3 times smaller power input (150W vs. 400W). Measurement of chemiluminescence signal used to optimize the input parameters of shaftless screw DBD conveyor treatment has proved its relevance to the rapid validation of treatment quality, as it allowed to avoid labour-intensive particleboards preparation with insufficiently modified PET fraction. Obtained mechanical properties of plasma activated PET flakes containing particleboards were comparable to that particleboards without any PET addition. This is a further very promising result. In [4] plasma activated PET were able to reach internal bonding strength of only 80% of pure wood particleboards. We suppose that this improvement should be attributed to generally better uniformity of plasma treatment of PET flakes' multiform shapes.

Acknowledgement: "This works was supported by TACR, project no. TP01010039."

5. References

[1] Sinha V, Patel MR, Patel JV (2010). PET waste management by chemical recycling: A review. *Journal of Polymers and the Environment*, *18*(1), 8–25.

[2] Gu L, Ozbakkaloglu T. (2016) Use of recycled plastics in concrete: A critical review, *Waste Management*, 51, pp. 19-42.

[3] Iždinský J, Tóth V, Kúdela J: Polyethylene terephtalate recycling in particle board production. In *Wood the best materials for mankind.* Zvolen. Arbora Publishers, 2013, pp. 93-97. ISBN 978-80-968868-6-9

[4] Klímek P, Morávek T, Ráhel J, Stupavská M, Děcký D, Král P, … Wimmer R (2016) Utilization of air-plasma treated waste polyethylene terephthalate particles as a raw material for particleboard production. *Composites Part B: Engineering*, *90*, 188–194.

[5] Buček A, Brablec A, Kováčik D, Sťahel P, Černák M (2017) Glass bond adhesive strength improvement by DCSBD atmospheric-pressure plasma treatment. *International Journal of Adhesion and Adhesives*, *78*(May), 1–3.

[6] Štěpánová V, Šrámková P, Sihelník S, Stupavská M, Jurmanová J, Kováčik D (2020) The effect of ambient air plasma generated by coplanar and volume dielectric barrier discharge on the surface characteristics of polyamide foils. *Vacuum*, *183*.

[7] Talviste R, Galmiz O, Stupavská M, Ráheľ J (2020) Effect of DCSBD plasma treatment distance on surface characteristics of wood and thermally modified wood. *Wood Science and Technology*, *54*(3), 651–665.

[8] Pouchlý V, Ráheľ J, Spusta T, Ilčíková M, Pavliňák D, Morávek T, Maca K (2019). Improved microstructure of alumina ceramics prepared from DBD plasma activated powders. *Journal of the European Ceramic Society*, *39*(4), 1297–1303.

[9] Shepa, I., Mudra, E., Pavlinak, D., Antal, V., Bednarcik, J., Mikovic, O., … Dusza, J. (2020). Surface plasma treatment of the electrospun TiO2/PVP composite fibers in different atmospheres. *Applied Surface Science*, *523*(April).

[10] Świecimska M, Tulik M, Šerá B, Golińska P, Tomeková J, Medvecká V, … Šerý M. (2020) Non-thermal plasma can be used in disinfection of scots pine (Pinus sylvestris L.) seeds infected with fusarium oxysporum. *Forests*, *11*(8), 1–12.

[11] Ráheľ J, Ilčíková M, Čech J, Hustý L. Plasma conveyor for the treating bulk materials, *Czech Utility model* – 34036, (26.05.2020).

EFFECTS OF ATMOSPHERIC PRESSURE AIR PLASMA ON PHOTOCATALYTIC ACTIVITY OF TIO_2 NANOFIBERS

Juraj Surovčík[1], Veronika Medvecká[1], Miroslav Zahoran[1]

[1]*Faculty of Mathematics, Physics and Informatics, Comenius University in Bratislava*
E-mail: Juraj.surovcik@fmph.uniba.sk

TiO_2 based materials are used in various applications, such as self-cleaning surfaces, energy storage and conversion devices, solar cells or air and water purification systems. For purification purposes, it is important to find ways to enhance photocatalytic activity of the semiconductor. In this work, we focused on increasing activity of electrospun TiO_2 nanofibers with atmospheric pressure air plasma generated by Diffuse coplanar surface barrier discharge (DCSBD).

1. Introduction

In recent years, photocatalysts are widely studied, mostly for their use in energy production and storage[1], and in purification systems[2]. TiO_2 is arguably the most promising photocatalysts for several reasons: it is durable, biologically and chemically inert, non-toxic, easy to produce, transparent to visible light and strong oxidizing abilities.

The most important requirement for the photocatalyst to decompose organic compounds is that the redox potential of H_2O/*OH lies within the band gap of this semiconductor. Upon absorption of UV light corresponding to TiO_2 band gap (varying for different crystal phases), electron-hole pairs separate in the material. After the separation, the charge carriers then diffuse into the material, where most of them recombine, and the energy is converted to either photons or phonons. Only those, that reach the surface of the material can drive the redox reactions. Using 1D structures such as fibers or tubes increases active reaction surface and limits diffusion in other two dimensions, which leads to improved photocatalytic effectivity.

In the past, several studies have shown enhancing effects of plasma on photocatalytic activity of titanium dioxide. Kong et al. used argon plasma etching to introduce surface defects to the nanosheets, remove organic contaminants and create porous structure. Oxygen vacancies and Ti^{3+} defects were also formed on the surface, which lead to narrowing of the band gap, broadening the light absorption spectrum.[3]

In our work, nanofibers were used because of several advantages they have as a photocatalyst – big surface area to volume ratio, limited diffusion, and contrary to nanoparticles, can form a self-standing structure. The goal was to examine the possibility of improving photocatalytic activity of TiO_2 nanofibers using low-temperature atmospheric pressure air plasma treatment.

2. Materials and methods

For our experiments, we used TTIP/PVP (tetraisopropoxide/polyvinylpyrrolidone) (80:20 ratio) nanofiber mats prepared by electrospinning using Nanospider^{TM}.

In the first step, as-spun fibers were exposed to DCSBD plasma generated in air at atmospheric pressure, using 15 kHz high voltage power source operating at 400 W for 30 minutes. After the plasma treatment, the nanofiber mat was calcinated at 500°C for 2 hours with rapid heating rate 22.5°C/min.

Photocatalytic activity was measured by the rate of decomposition of methylene blue in 10mg/l solution under the UV light. Quantitative values were obtained by absorption measurement at λ=664nm.

We compared the photocatalytic activity of plasma treated and thermally calcinated fibers with fibers calcinated under the same conditions without plasma treatment and for reference, we also measured absorbance of methylene blue solution without photocatalyst sample.

The WDX analysis of the treated samples was performed to compare changes in chemical composition. Under normal circumstances, nanofibers are relatively thin (under 1 μm) to be examined by WDX with interaction volume reaching several μm into the material. For this reason, the samples were homogenized using laboratory mortar and pestle, creating nanopowder. Another reason for this was natural microscopic non-homogeneity of as-spun fibers. After homogenisation, high pressure was applied to create small solid tablets. By this, the issues with non-homogeneity and small interaction volume were resolved, the ability to analyse the changes on the surface of the fibers was lost in the

process, which might be important for the purification application as well. For this, another diagnostic method will need to be used.

3. Results and discussion

WDX analysis (Table 1) showed the lower content of carbon residue and proportional higher ratio of titanium in plasma treated TiO_2 fibers compared to nontreated. In previous research it was found, that DCSBD plasma during plasma assisted calcination can help decomposition of organic part of TTIP/PVP before thermal treatment and the final product after sintering contains less carbon compounds.[4] Additionally, plasma treatment primarily affects the surface of fibers. Measurements of the homogenized samples provide information about chemical composition of volume of material.

	C (at%)	O (at%)	N (at%)	Ti (at%)
Nontreated	10.67 ± 0.13	69.11 ± 0.57	8.91 ± 0.46	11.31 ± 0.37
Plasma treated	10.01 ± 0.12	68.84 ± 0.57	9.05 ± 0.46	12.10 ± 0.38

Table 1 Stoichiometric ratios of homogenized non-treated and plasma treated TiO_2 nanofibers measured by WDS

In our experiments, we observed improvement in photocatalytic activity of plasma treated TiO_2 nanofibers represented by increased rate of photocatalytic methylene blue decomposition under UV irradiation.

The effect of plasma pre-treatment on photocatalytic activity of prepared TiO_2 fibers measured by decomposition of MB solution under UV irradiation showed more effective MB removal when sample was treated by plasma before sintering. The plasma pre-treatment caused significantly higher rate of MB decomposition. After 3 minutes, the absorbance of MB solution with plasma pre-treatment sample was comparable with non-treated sample, however, after 6, 12 and 18 minutes of UV irradiation, the absorbance of MB solution was by 2.6, 10.3 and 15.1 % (respectively) lower compared to untreated sample.

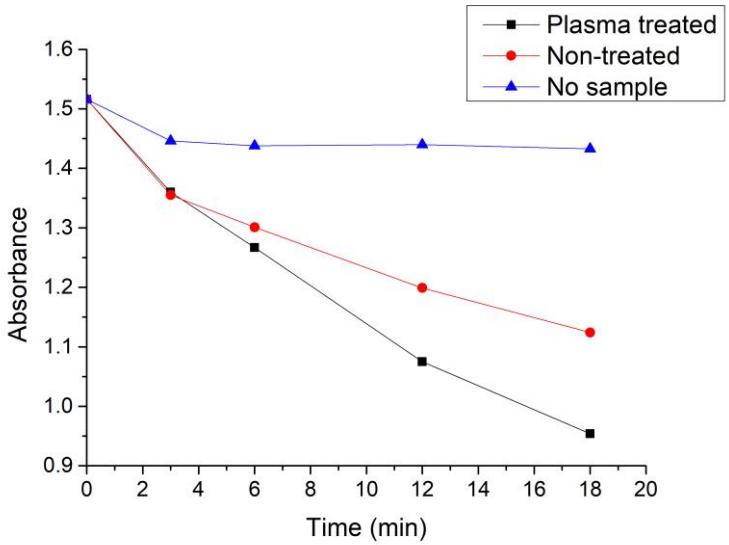

Figure 1: Absorbance of methylene blue solution at λ=664nm vs. irradiation time

4. Conclusion

In this work, the influence of plasma pre-treatment in preparation of TiO_2 fibers by the plasma assisted calcination was studied in term of effect on properties, which are important for application of mentioned material. TiO_2 is known for its photocatalytic activity and we found out, that the pre-treatment of initial TTIP/PVP fibers not only reduce the organic part of these hybrid fibers proved by previous research, but DCSBD plasma treatment also causes better photocatalytic activity of this material by significantly

higher rate of methylene blue solution decomposition with presence of samples treated by plasma compared to untreated sample. This effect indicated higher decomposition of organics and is very prospective in application for water and air purification, where TiO_2 is one of the most studied material.

Acknowledgements: This research has been supported by the Slovak grant agency Vega, project No. 1/0782/19 and UK grant No. UK/241/2020.

5. References

[1] D.P. Opra, S. V. Gnedenkov, and S.L. Sinebryukhov, *J. Power Sources*, **442**, 227225 (2019).
[2] S. Riaz and S.J. Park, *J. Ind. Eng. Chem.*, **84**, 23–41 (2020).
[3] X. Kong, Y. Xu, Z. Cui, Z. Li, Y. Liang, Z. Gao, S. Zhu, and X. Yang, *Appl. Catal. B Environ.*, **230**, 11–17 (2018).
[4] V. Medvecká, D. Kováčik, A. Zahoranová, and M. Černák, *Appl. Surf. Sci.*, **428**, 609–615 (2018).

INFLUENCE OF PLASMA PROPERTIES ON REACTIVE SPECIES IN PAW

Olivera Jovanović[1], Nevena Puač[1], Radmila Sandić[1], Nikola Škoro[1]

[1]*Institute of Physics, University of Belgrade, Pregrevica 118, 11080 Belgrade, Serbia*
E-mail: olivera@ipb.ac.rs

We have used a pin-type of atmospheric pressure plasma jet (APPJ) for treatment of distilled water samples and production of plasma activated water (PAW). Electrical characterization of the APPJ and plasma power measurements were performed in order to obtain information about stability of the treatment conditions, the plasma properties, and the influence of plasma parameters on PAW. In order to investigate the influence of working gas on the PAW chemistry, we have performed treatments with helium or argon streamer discharges. Diagnostics of treated liquid samples were carried out to evaluate the effectiveness of plasma treatment. Results show that chemically reactive gaseous environment of helium discharge favours the production of nitrates and nitrites. At the same time, the argon discharge produces an order of magnitude higher values of hydrogen peroxide and nitrates, but the amount of nitrites is quite low.

1. Introduction

Cold atmospheric pressure plasmas have been intensively investigated over the past decade due to their great potential for various applications. In the area of plasma agriculture, gaseous plasma treatment of aqueous solutions has multiple advantages such as reduction or elimination of organic contaminants and antimicrobial effects [1, 2]. The exposure of water to plasma induces a number of reactions occurred in the gaseous phase and introduces reactive oxygen and nitrogen species (RONS) species in aqueous phases. The resulting "plasma-activated water" was shown to remain active long after the plasma is turned off [3]. Among the most commonly detected chemical species in PAW are hydrogen peroxide, nitrite and nitrate due to their relative stability. These reactive species play a key role in the reactions involving dissolved organic species in water and can effectively inactivate bacteria or microorganisms [4]. Proper and detailed diagnostics of plasma sources will help to achieve better understanding and establish the correlation between the plasma processes and the treatment effects which is of crucial importance for further applications. From the point of view of plasma physics, the central issue is to standardize the performance in RONS production. Here we will present the results of the influence of the type of the working gas used (He or Ar) on the production of RONS in PAW.

2. Experimental setup

In the study, we assessed the performance characteristics of the pin-type configuration of an APPJ powered by a continuous high voltage signal at frequency 330 kHz and operated with He and Ar as working gases. Schematics of APPJ and experiment set up are provided in Fig.1. Determination of concentrations of three reactive species (H_2O_2, NO_2^-, NO_3^-) in liquid and pH of treated aquous solution was performed. Plasma source consists of a metal cylindrical case, a glass tube with concentrically placed powered sharpened electrode. The copper tape at the bottom of the microtiter plate was connected to the ground through a 1 kΩ resistance for monitoring the discharge current flowing through the plasma. The electrical volt–ampere characteristics as well as the power consumption were analysed with electrical probes.

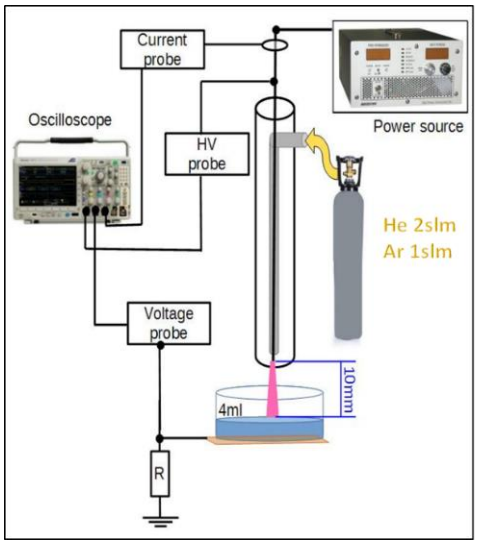

Fig. 1. Schematic overview of the experimental set up.

Two types of plasma treatments were done: with He as working gas with flow rate of 2 slm and Ar with flow rate of 1 slm. Treatment times were 5 and 10 minutes. The volume of treated samples placed in the wells of 6-well microtiter plate below the APPJ was 4ml. The distance between the water surface and wire was 10 mm in all treatments. In order to characterize PAW we used colorimetric methods for measuring the concentrations.

3. Results and Discussion

In Fig. 2. we show concentrations of long-lived reactive species obtained after 5 and 10 minutes treatment of water sample by a pin-electrode jet. We measured completely different concentrations of all reactive species depending on the working gas. By changing the working gas, concentrations of produced H_2O_2 and NO_3^- in PAW are measured to differ by an order of magnitude. For both gases the results show an increase in concentration of H_2O_2 and NO_3^- with treatment time. The amount of nitrite generated by He plasma is almost same after 5 and 10 min while in case of Ar plasma the concentrations of nitrite in liquid are negligible. This result may also reflect a significant difference in power dissipation under different feed gas composition.

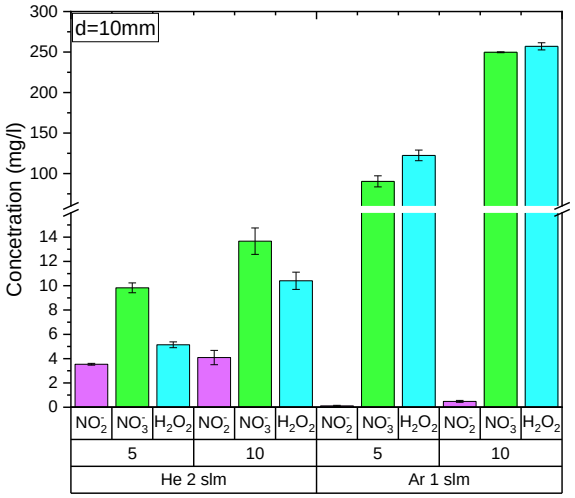

Fig. 2. Concentrations of nitrite, nitrate, and hydrogen peroxide in PAW samples after 5 and 10 minutes treatments using He and Ar as working gases.

4. Conclusions

Plasma treatments of distilled water were done using an APPJ in a pin-electrode configuration. These experiments demonstrated that changing the working gas produced different amounts of measured reactive species in PAW while in both cases filamentary type of plasma was established. Correlating measurement of plasma parameters with liquid sample properties will enable to investigate influence of different plasma parameters on changes in the properties of treated samples. Furthermore, it will be important to explore the potential use of these samples for the particular application in plasma agriculture field.

5. Acknowledgments

This research has been mainly supported by MESTD Republic of Serbia projects III41011 and ON171037. Part of the research was funded by IPB through grant by MESTD.

6. References

[1] Graves D Bakken L Jensen M and Ingels R 2019 *Plasma Chemistry and Plasma Processing*. 39.
[2] Skoro N Puac N Zivkovic S Krstic-Milosevic D Cvelbar U Malovic G Petrovic Z Lj 2018 *Eur. Phys. J. D*, 72 2.
[3] Lukes P Dolezalova E Sisrova I and Clupek M 2014 *Plasma Sources Sci Technol* 23.
[4] Niquet R Boehm D Schnabel U Cullen P J Bourke P and Ehlbeck J 2017 *Plasma Processes and Polymers* 15 e1700127.

INVESTIGATION OF STABILITY OF CORONA ION SOURCE AND ELECTRIC FIELD IN ION MOBILITY SPECTROMETRY

Arian Fateh Borkhari, Ladislav Moravský, Štefan Matejčík

Department of Experimental Physics, Comenius University
Mlynská dolina F2, 842 48 Bratislava, Slovakia

E-mail: borkhari1@uniba.sk

The stability of the operation of the negative corona discharge ion source for the Ion Mobility Spectrometry (IMS) has been studied. The temporal stability of the ion current was investigated as a function of wire diameter (20, 50, and 100μm) and wire material (the high-voltage electrode). The ion current generation efficiency was increasing for thin microwires. The temporal ion current stability was improving with the increasing electrode gap between the high voltage electrode and the hollow electrode (from 1 up to 10mm) and with decreasing of the wire diameter. The impact of the electrode material was low on the stability of the ion current. Additionally, we have simulated the configuration of the electric fields in the ion source and the IMS drift-tube.

1. Introduction

Ion Mobility Spectrometry (IMS) is an analytical technique for the separation of ions in the gaseous phase based on the differences in the mobilities of the ions under an electric field. The ion source is one of the main parts of IMS, besides the reaction chamber, shutter gride, drift tube, and detector [1-7]. The ion source serves as a source of reactant ions (RI) of positive or negative polarity, which are used for ionization of the sample in the reaction region and formation of gas-phase ions. Several different ion sources for IMS systems have been developed, such as radioactive ion sources, discharge ion sources, thermal ionisation, photoionization, X-ray ionization, electrospray ionization, atmospheric pressure electron gun, etc. [5-7].

In the present work, we present a study of the stability of the corona discharge ion source in negative polarity. The selection of a suitable material and geometry (radius of wire and the electrode gap) of the corona discharge electrode (microwire) result in the improvement of the stability of the ion current, the improvement of the ion intensity, and thus the sensitivity of IMS [8-11].

2. Experimental Setup

Figure 1 shows the experimental setup to study the operation of the corona discharge as an ion source for IMS. In this study, we have used a wire-to-plane configuration with the hollow in the plane electrode to negative corona discharge. The hollow electrode can be spatially adjusted in three directions, and the electrode separation can be controlled to 1 micrometre. A microwire was used as the high voltage electrode with different diameters (20, 50, and 100μm) and materials (tungsten, copper, platinum, cobalt, stainless steel), while the plane electrode material was brass. An additional electrode, Faraday plate was placed behind the plane electrode. Between the plane electrode and the Faraday plate, an extraction voltage (V_{HE}) was applied. The Faraday plate was equipped with a protection circuit consisting of back-to-back diodes. The electric current was amplified with a transimpedance current to voltage amplifier and measured using an oscilloscope (Tektronix TDS2022B). The high voltage part of the electrical circuit consisted of a high voltage power supply (Fug HCP 35-20000), with a resistor (15MΩ) to limit the DC current (10μA). The second DC power supply (Heinzinger LNG 350-03) supports the high voltage up to 350V to the plan electrode (HE).

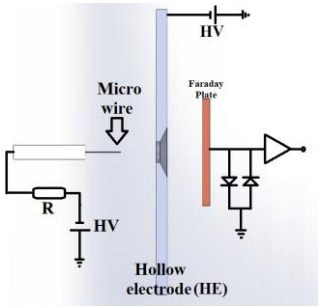

Fig. 1. The schematic view of the experimental setup for ion generation.

3. Results

Figure 2 shows the measured dependence of the negative corona current on the applied negative high voltage for different wire diameters (20, 50, and 100μm) and various electrode gap distances (from 3 up to 10mm). The high-voltage electrode was made of tungsten. The ion current was measured for different voltages of the hollow electrode (V_{HE} = 0, 50, 100, 200, and 350V). The potential V_{HE} pushes the ions generated by corona discharge to the detector (Faraday plate). We have observed that the measured current on the Faraday plate increases with the increasing HV potential on the wire electrode (due to increase of charge current) and also with the increasing HE potential, due to improvement of the ion transport to the Faraday plate.

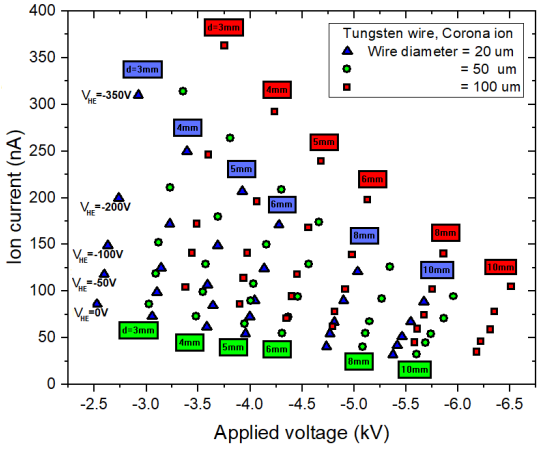

Fig. 2. Current-voltage characteristics for different diameters of the tungsten wire.

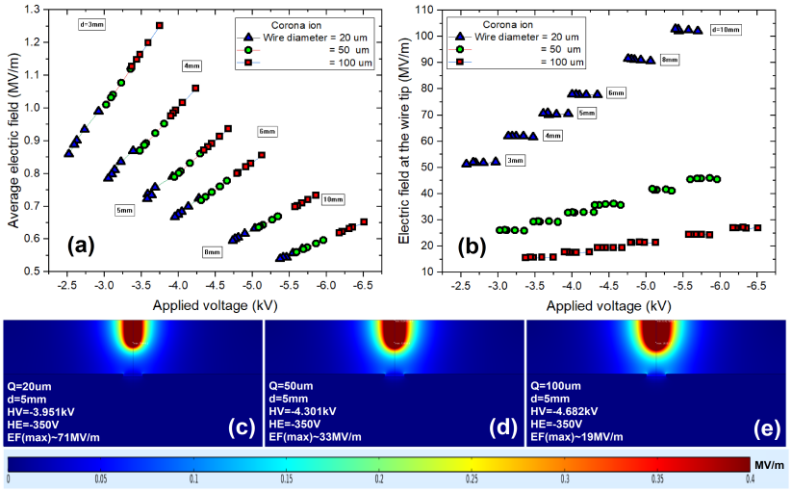

Fig. 3. Electric field strength for different diameters of the wire.

The diameter of the microwire affects the ion generation and its stability (Fig. 3) due to changes in the electric field. The average electric field between the electrodes is illustrated in Fig. 3 a) for 20, 50, and 100μm wire diameters. The experimental voltage values were used to simulate the local electric field strength at the microwire tip (Fig. 3 b). Based on Fig. 3 a), the average electric field increases with the decreasing of gap distance, whereas increased gap causes the increase of the local maximum electric

field at the wire tip (Fig. 3 b). The graphical simulation in Fig. 3 c, d, and e) is presented to validate the plotted results in Fig. 3 a) and Fig. 3 b).

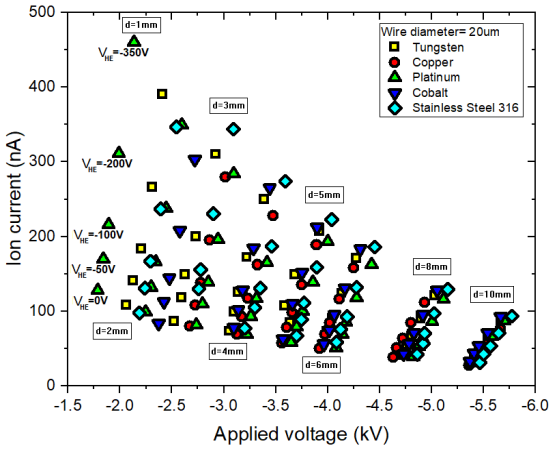

Fig. 4. Experimental data: current-voltage characteristics for different wire materials.

The effect of the material of the wire electrode on the current-voltage characteristics is presented in Fig. 4. The measured current-voltage characteristics were performed for different wire materials (tungsten, copper, platinum, cobalt, and stainless-steel), different discharge gaps and V_{HE} potentials. The diameter of all wires was 20µm. Figure 5 shows the values of the electric field strength for different wire materials and different discharge currents. The average electric field is presented in Fig. 5 a). The local electric field strength at the wire tip was calculated for the applied voltages and different wire materials (Fig. 5 b). The field strengths are illustrated in Fig 5 c, d, and e where the microwire has 20µm diameter for 1, 5, and 10mm gap distance.

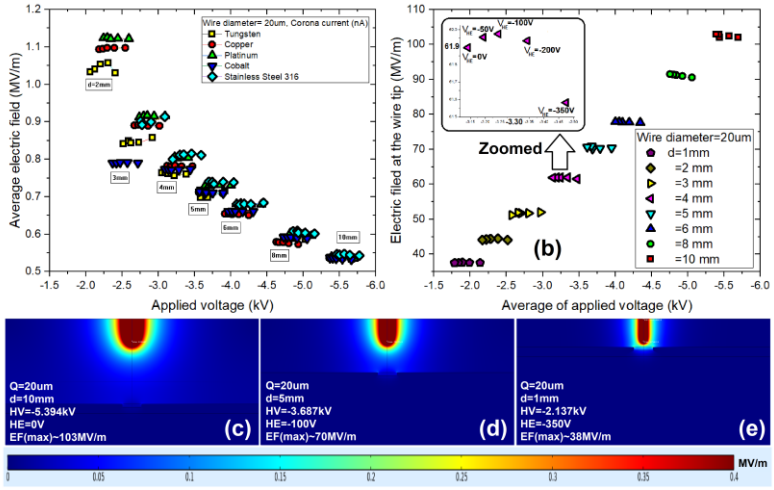

Fig. 5. The strength of the local electric field for different wire discharge gaps.

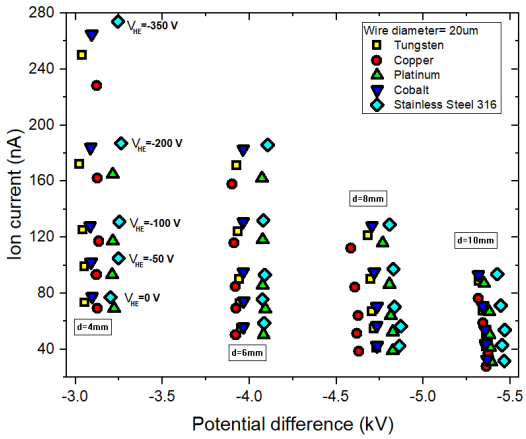

Fig. 6. Experimental I vs V plots for different wire materials.

Figure 6 shows the dependence of the ion current on the potential differences between the electrodes. The high value of relative standard deviation was observed for thick wire (100μm). These results are shown in Fig. 7.

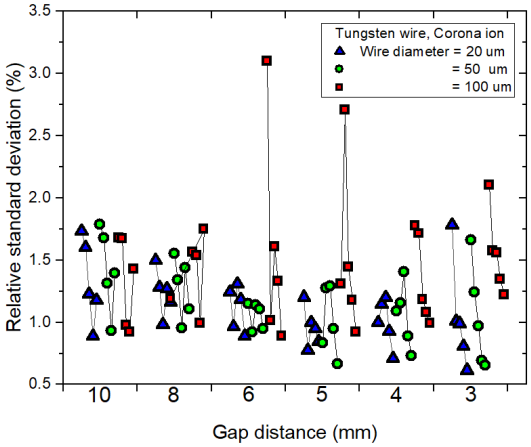

Fig. 7. Relative standard deviation (%) of the temporal stability of ion current for different diameters of the tungsten wire.

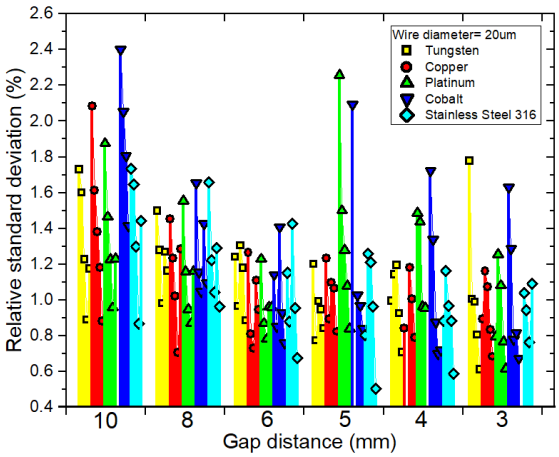

Fig. 8. Relative standard deviation (%) of signal stability of Corona ions for different wire materials.

The relative standard deviation has been calculated for ion currents (Fig. 8), which have been related to different wire materials. We found the proper gap-distance for the generation of a more stable ion signal based on the geometrical configuration of electrodes. Fig. 8 shows the more stable signals at d=5 and 6mm for most of the materials.

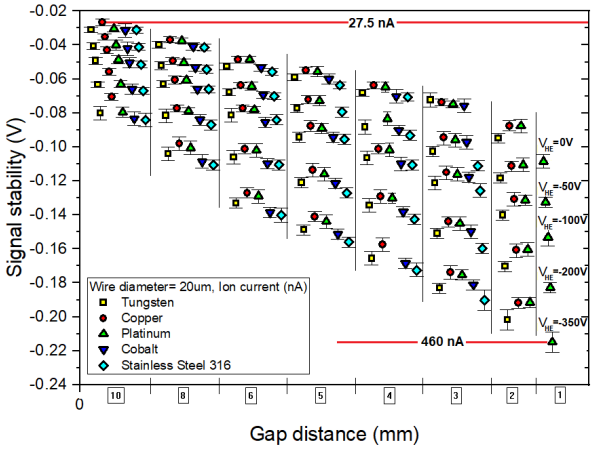

Fig. 9. Experimental data of signal stability of Corona ions for different wire materials.

The statistical analysis of the temporal stability of the ion current is presented in Fig. 9 for different wire materials and different electrode gaps. The result shows that the stability of the discharge current

was not substantially affected by the wire material. However, we see a week effect of the electrode gap for smaller gaps, the relative temporal stability of the discharge current was higher. We relate it to the strength of the electric field. In addition to the simulation of the electric fields in the ion source, we have performed simulations of the electric fields in the IMS (Fig. 10). For the functionality of the IMS, the strength of the electric field along the axis of the IMS drift tube is of great importance (Fig. 11). Figure 11 shows that the homogeneity of the electric field in the drift tube is quite good and that the inhomogeneities appear only in the ions source, shutter gride, and at the detector. However, in the future, we should further improve the homogeneity of the electric field in the IMS.

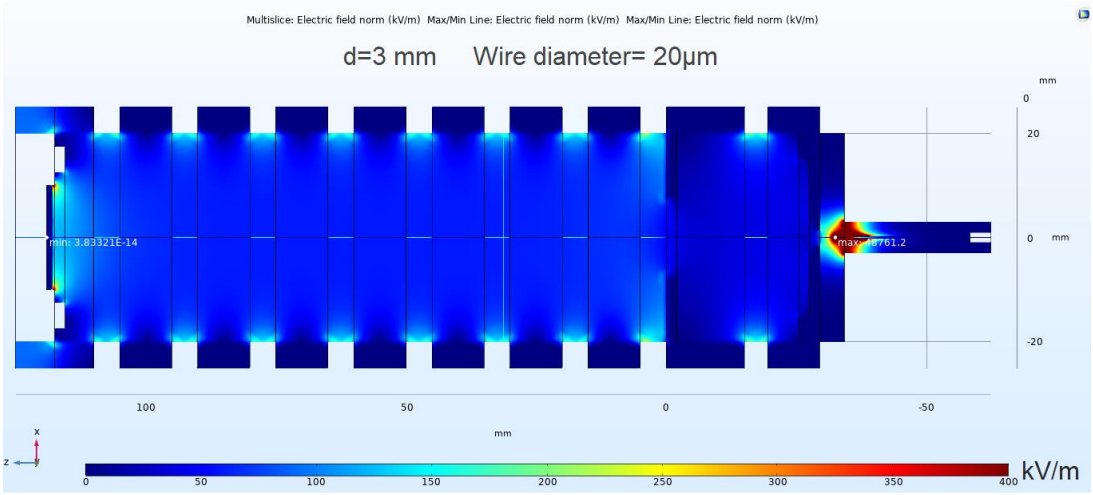

Fig. 10. Simulation of a homogeneous electric field in the IMS drift-tube.

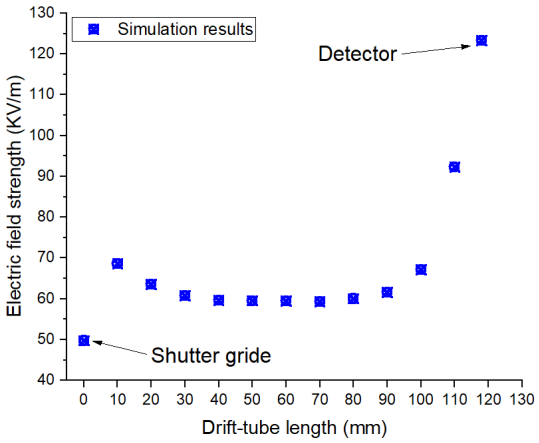

Fig. 11. Electric field strength at the axis of IMS drift-tube.

4. Conclusion

We have presented an experimental study concerning the temporal stability of the generation of the ion current by the Corona Ion Source in IMS. Different materials and diameters have been investigated for the high voltage electrode (microwire). Experimental data including the current-voltage characteristics, the average electric field between the electrodes, and the local electric fields at the tip of the wire electrode were determined. The experimental studies and simulations were carried out for the microwires (20, 50, and 100µm) diameter and different wire materials (tungsten, copper, platinum, cobalt, and stainless steel). The improved temporal stability of the ion current was observed for the smaller wire diameter (20µm). The impact of the electrode material on the temporal stability of the ion current was low. Based on the practical values of electrical parameters of the IMS, we have simulated a 2D map of the electric field in IMS and the axial dependence of the strength of the electric field.

5. References

[1] Stano M, Safonov E, Kucera M, Matejcik Š 2008 Chem. Listy 102 s1414−s1417.
[2] Sabo M, et al. 2015 Analytical Chemistry 7 14 7389–7394.
[3] Sabo M, et al. 2010 International Journal of Mass Spectrometry 293 23–27.
[4] Gravendeel B 1987 ebook: doi:10.6100/IR256688.
[5] Raizer Y P 1987 Springer Berlin.
[6] Scheffler P, Gessner C, Gericke K H 2000 Braunschweig (D).
[7] Gunzer F, Ulrich A, Baether W 2010 Int. J. Ion Mobil. Spec. 13:9–16.
[8] Kim H J, Han B, Woo C G and Kim Y J 2016 IEEE Transactions on Industry Applications pp 99.
[9] Yehia A and Mizuno A 2008 Int. J. of Plasma Environmental Sc. & Tec. Vol.2 No.1 pp 44-49.
[10] Petrov A A 2009 IEEE Transactions on plasma science Vol. 37, No. 7.
[11] Horvath G, Skalny J D, Orszagh J, Vladoiu R, Mason N J 2010 Plasma Chem Plasma Process 30:43–53.

PREPARATION OF SILVER AND GOLD NANOPARTICLES BY NOVEL PIN-HOLE DC PLASMA SOURCE

Ludmila Čechová, Zdenka Kozáková, František Krčma

Faculty of Chemistry, Brno University of Technology, Purkyňova 118/464, 612 00 Brno
E-mail: ludmila.cechova@vut.cz

Silver and gold nanoparticles were produced using the pin-hole discharge generated by dc non-pulsing high voltage directly in precursor solution. Silver nitrate solution was used as the precursor for silver nanoparticles, chloroauric acid was used as the precursor for gold nanoparticles. Effects of discharge time, precursor concentration and additives such as reduction agent (ethylene glycol) and capping agent (polyethylene glycol and sucrose) were studied. Nanoparticles were mainly analysed by UV-VIS spectrometry. The size of prepared nanoparticles was determined by dynamic light scattering with backscattering detection. To determine the stability of NPs, Zeta potential was measured by electrophoretic light scattering. Formation of silver and gold nanoparticles was than confirmed by SEM/EDS analysis. Both kinds of particles had spherical shapes.

1. Introduction

Nanoparticles (NPs) are defined as particles with size in the range from 1 to 100 nm. Properties of metallic nanoparticles are different from the bulk metals, such as the lower melting point or higher surface area, making them more attractive for different applications [1]. They can be utilized in many different applications, such as biomedical science [2], electronics [3], biotechnology [4] or drug delivery [5]. Various methods can be used to prepare metallic nanoparticles. Recently, a new technique using non-thermal plasma discharge directly in liquids was examined. Metallic nanoparticles can be generated from metallic precursor solution or sputtered from the electrode material. Different setups and plasma reactors were used to prepare metallic nanoparticles, mainly from noble metals such as copper, silver, gold or platinum. Lung et al prepared gold nanoparticles using arc discharge in water [6]. Colloidal copper nanoparticles with gelatine and ascorbic acid as the capping agent were prepared using solution plasma process [7]. Microwave induced plasma in liquid was also used for preparation of gold [8], silver and platinum [9]. This paper deals with synthesis of silver and gold nanoparticles using a special pin-hole electrode system generating plasma directly in liquid solution of a metal precursor by DC high voltage up to 1 kV [10].

2. Experimental setup

The plasma reactor, presented in Figure 1, consisted of two electrodes – the main jet electrode and second (counter) electrode [10–13]. The main jet electrode was constructed by a tungsten wire with diameter of 1.0 mm inserted into a dielectric cylindrical rod made of Macor ceramics with outer diameter of 10 mm. An orifice with the diameter of 1.2 mm was made in the ceramics along its longitudinal axis. A small gap of 1 mm was kept between the end of the wire electrode and the region around the electrode end of the dielectric rod. This configuration substantially increased electric field intensity in the gap of the dielectric rod and thus it allowed plasma ignition at relatively low applied voltage. An outer glass tube served as a holder. The second (counter) electrode was a planar plate made of aluminium with dimensions of 20x100 mm^2 [10]. The system was supplied from the specially designed dc power source giving the non-pulsing high voltage up to 3 kV in the peak. A negative polarity was applied on the main electrode, solution was grounded. Both electrodes were immersed in a vessel containing 200 ml of the precursor solution – $AgNO_3$ for silver nanoparticles and $HAuCl_4$ for gold nanoparticles. The treated solutions were sampled every 30 seconds during the discharge operation for the UV-VIS spectrometry. Absorption spectra of sampled solutions were recorded by the Helios Omega (Unicam) spectrometer in the range of 300−600 nm. Dynamic light scattering and Zeta potential measured by the Zetasizer Nano ZS (Malvern Pananalytical Ltd.) were used in order to determine size and stability of nanoparticles. Detailed photos of formed nanoparticles and EDS analysis were taken by the high resolution scanning electron microscope FEI Verios 460L (Thermo Fisher).

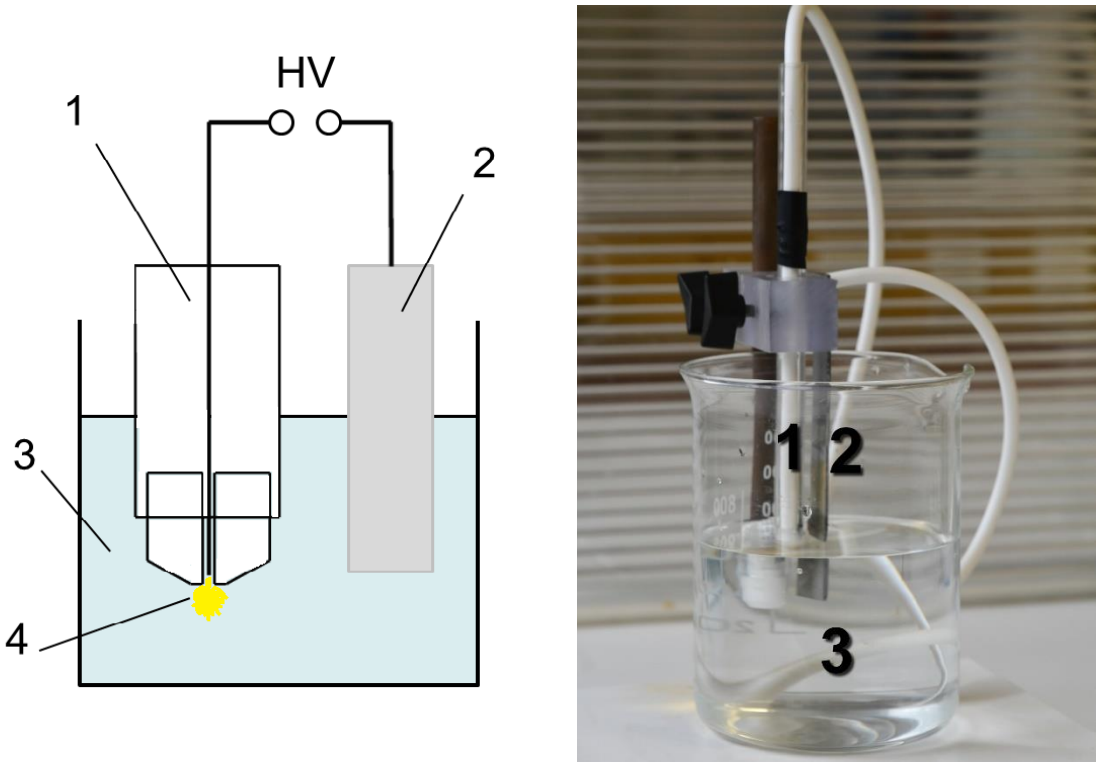

Figure 1 Experimental setup (left: scheme, right: photograph): 1 - main jet electrode, 2 - counter electrode, 3 - precursor solution, 4 – active plasma region

3. Results

Silver nitrate in the concentration of 25–200 mg l^{-1} was used as a precursor for silver nanoparticles formation. Solutions were sampled every 30 seconds during the discharge operation to determine nanoparticle formation in time. Nanoparticles were formed in the plasma region near the main jet electrode and spread into the solution. The absorbance of silver nitrate solution increased during the discharge treatment with the maximal absorption at 410 nm (Figure 2 left). The same increase of absorbance was observed while examining the effect of precursor concentration. Experiments were carried out at the mean input power of 60 W for silver nanoparticles and the discharge lasted for 2 minutes. After 2 minutes of the discharge, Ag nanoparticles had Zeta potential over 30 mV and were stable. The size of Ag NPs ranged from 10 to 1000 nm. On the SEM photograph in Figure 3 (left) we can see that nanoparticles had mainly spherical shapes.

Gold nanoparticles were prepared from the solution of chloroauric acid at the mean input power of 100 W. The time and concentration effect was also observed. According to the absorption spectra shown in Figure 2 (right), Au NPs were formed in the solution after 3 minutes of the discharge treatment. In order to determine the effect of concentration, solutions with concentration from 25 to 100 mg l^{-1} were prepared. According to data from DLS, the size of Au NPs was 10 nm on average. Au NPs prepared from the solution with the concentration of 100 mg l^{-1} had average size of 100 nm. In Figure 3 (right) we can see SEM photograph of gold nanoparticles with spherical shapes. Their Zeta potential was over 30 mV, which means that nanoparticles were stable. To stimulate the reduction process of Au NPs, ethylene glycol in the concentration of 1mM was added. Its addition decreased the mean input of power needed for the stable discharge operation to 80 W. However, ethylene glycol destabilized NPs (Zeta potential was lower than 30 mV) and they started to form larger structures and sediment. Even after the addition of the capping agent into the solution of $HAuCl_4$ and ethylene glycol (50 mg l^{-1} of sucrose or 50 mg l^{-1} of polyethylene glycol), NPs still had Zeta potential lower than 30 mV. To conclude the effect of additives, it is the best to prepare NPs from their precursor solution only, even if the power consumption is higher. With this method, only few milligrams of chemicals are needed, nanoparticles are stable on their own, and it is time efficient as it only takes 2–4 minutes to prepare them.

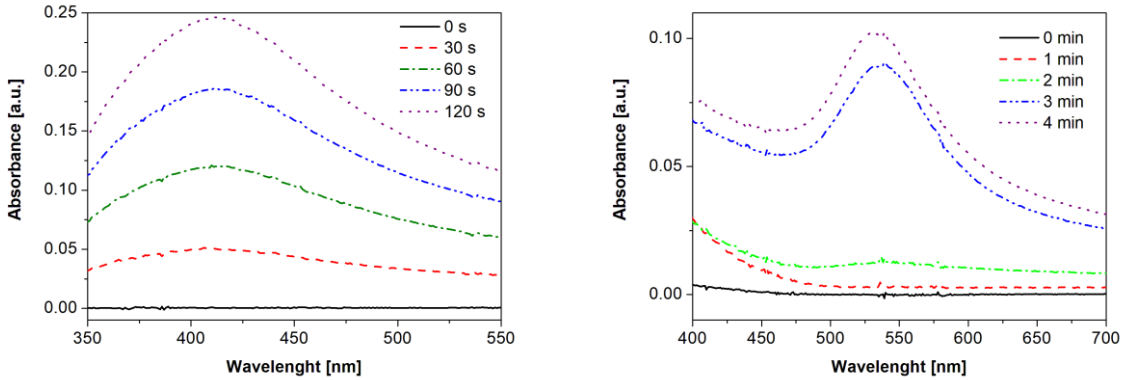

Figure 2 Left: Absorption spectra of $AgNO_3$ solution (100 mg l^{-1}) during the discharge treatment (mean input power of 60 W). Right: Absorption spectra of $HAuCl_4$ solution (100 mg l^{-1}) during the discharge treatment (mean input power of 100 W).

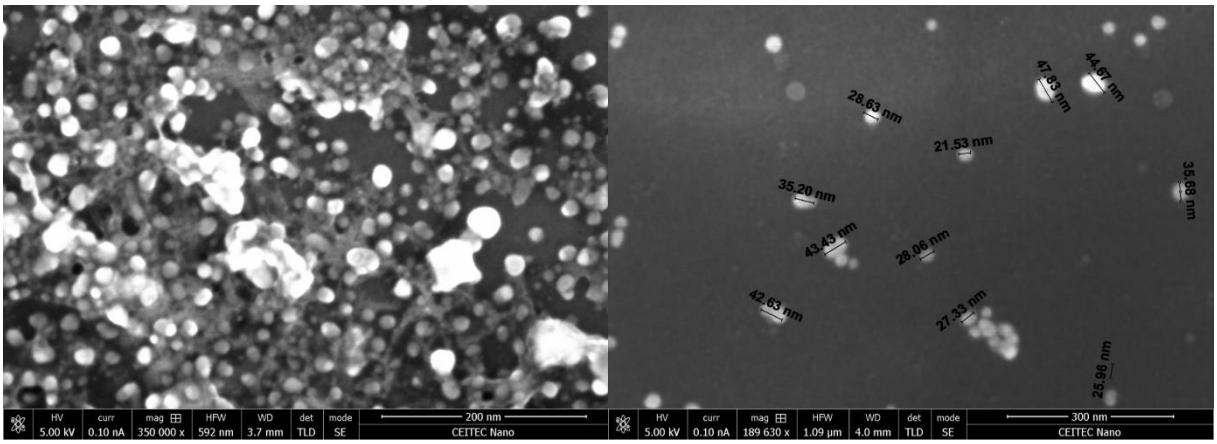

Figure 3 Left: SEM photograph of silver nanoparticles formed after the 2-minute discharge treatment (mean input power of 60 W) in $AgNO_3$ solution (100 mg l^{-1}), magnification: 350 000x. Right: SEM photograph of gold nanoparticles formed after the 4-minute discharge treatment (mean input power of 100 W) in $HAuCl_4$ solution (100 mg l^{-1}), magnification: 190 000x.

4. References

[1] Horikoshi S and Serpone N 2013 *Microwaves in Nanoparticle Synthesis: Fundamentals and Applications* 213 pages.
[2] Rajendran N K et al 2018 *Journal of Drug Delivery Science and Technology* **44** 421.
[3] Pejjai B et al 2017 *International Journal of Hydrogen Energy* **70** 1
[4] Pankhurst Q A et al 2003 *Journal of Physics D: Applied Physics* **36** R167
[5] Dobson J 2006 *Gene Therapy* **13** 283
[6] Lung J K et al 2007 *Journal of Alloys and Compounds* **434-435** 655
[7] Pootawang P et al 2013 *Nanotechnology* **24** 055604
[8] Nishimoto M et al 2017 *Materials Chemistry and Physics* **193** 7
[9] Sato S et al 2011 *Surface and Coatings technology* **206** 955
[10] Krčma F et al 2018 *Plasma Sources Science and Technology* **27** 065001
[11] Krčma F 2015 *Jet system for plasma generation in liquids* Czech Republic Patent CZ305304B6.
[12] Krčma F 2019 *Jet system for plasma generation in liquids;* European Patent EP3122161B1.
[13] Krčma F 2015 *Jet system for plasma generation in liquids;* Protected construction CZ27173.

Chairman of the session: František Krčma

MULTI-DIAGNOSTIC APPROACH TO ENERGY TRANSPORT IN AN ATMOSPHERIC PRESSURE PLASMA

Tristan Winzer[1], Judith Golda[2], Jan Benedikt[1]

[1]*Institute for Experimental and Applied Physics, Kiel University, Germany*
[2]*Plasma Interface Physics, Ruhr-University Bochum, Germany*
E-mail: winzer@physik.uni-kiel.de

In this study, we present an advancement of the well-studied µ-scale atmospheric pressure plasma jet (COST jet) using a capillary between the electrodes as a dielectric. Energy transport in this so-called capillary jet is studied combining several diagnostics with the goal to compile an energy balance, which holds information about plasma processes and possibilities for energy flow tailoring.

Atmospheric pressure plasma jets (APPJs) have gained increased interest in recent years, due to their application potential in medicine and industrial processes. These plasmas exhibit strong non-equilibrium characteristics with high electron energies at low gas temperature, especially when driven with rf-frequencies. These non-equilibrium state leads to transport processes inside the discharge. The energy is selectively coupled to the electrons by the electric rf-field. It is then dissipated via different physical processes to other species present in the plasma on diverging timescales, e.g. via drift, diffusion, elastic and inelastic collisions. To channel the energy inside the discharge into the desired processes, fundamental understanding of the influence of external parameters on the energy balance is necessary.

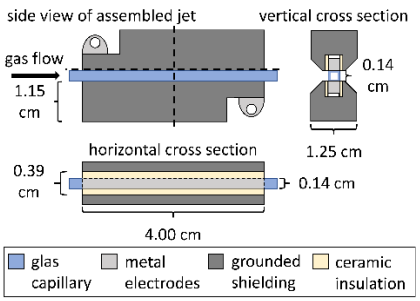

Fig. 1. Sketch of the capillary plasma jet.

APPJs typically have small dimensions and increased risk of instabilities, making diagnostics challenging. We therefore created a new setup with the same discharge geometry as the well-studied 'COST reference plasma jet' [1] but featuring a capillary with square cross-section as a dielectric at the electrodes (see figure 1). This setup was found to deliver stable plasma operation on long timescales and over a broad range of parameters, especially at high input powers. Characterization of the jet was done by electrical measurements, temperature measurements in the effluent, optical emission spectroscopy (OES) and molecular beam mass spectrometry (MBMS). Helium was used as feed gas with small admixtures of oxygen to study chemical processes. As external parameters, we chose input power and oxygen admixture as these have a large impact on electron density and energy distribution.

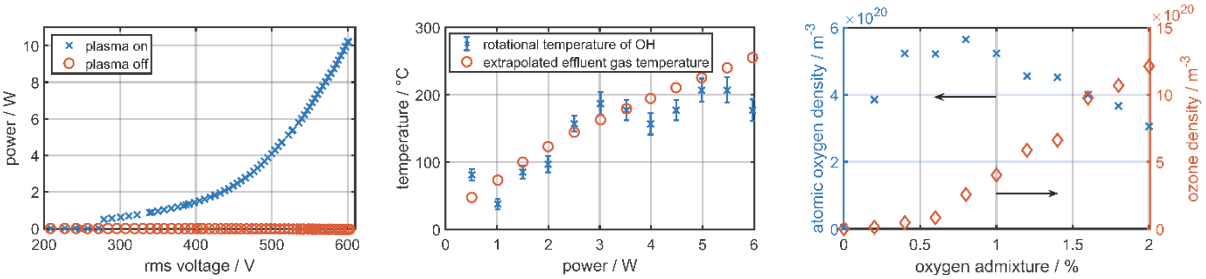

Fig. 2. Power characteristic (left), gas temperature as a function of input power at constant oxygen admixture of 0.5 % (middle) and atomic oxygen and ozone densities as a function of oxygen admixture at constant input power of 1 W (right).

Some results of the different measurement techniques are shown in figure 2. The dissipated power is always monitored to ensure the same operating conditions in all measurement series. It rises over-linearly with the applied voltage, indicating a mode-transition of the discharge around 1.5 W (figure 2, left). We found the gas temperature to increase almost linearly with the input power (figure 2, middle), while it stayed almost constant when varying the oxygen admixture. The atomic oxygen density showed a maximum around 0.6 % admixture while the ozone density did not reach a maximum in the observed admixture range (figure 2, right). We combined these results to obtain an experimental energy balance of the capillary plasma jet, which will be presented in the talk.

[1] J. Golda *et al* 2016 *J. Phys. D: Appl. Phys.* **49** 084003

SPATIAL-RESOLVED OPTICAL EMISSION SPECTROSCOPY OF THE SPOKE IN NON-REACTIVE HIPIMS

Marta Šlapanská, Michael Kroker, Jaroslav Hnilica, Peter Klein, Petr Vašina

Masaryk University, Brno, Czech Republic
E-mail: slapanska@physics.muni.cz

Spokes, also known as ionisation zones, have been observed at specific conditions in many types of magnetron sputtering discharges. This contribution shows the spatial-resolved optical emission spectroscopy of the spoke in non-reactive high power impulse magnetron sputtering discharge. Using the signals from a cylindrical probe and the fast photodiode the passing spoke was captured and its position was determined. The spatial-resolved emission of titanium atoms was investigated within the spoke for different working pressures.

1. Introduction

Over the last few years, it has been discovered that the plasma in a magnetron sputtering (MS) discharges is not always homogeneously distributed above the racetrack. Under certain conditions, the plasma is self-organised into rotating spokes [1], also known as ionisation zones [2]. They have already been observed in direct current magnetron sputtering (dcMS) [3, 4], high power impulse magnetron sputtering (HiPIMS) [1, 2, 5, 6] and radio frequency magnetron sputtering (rfMS) [7] discharges.

The spoke properties are highly dependent on the experimental conditions such as magnetic field strength, target material or the chamber geometry [8-12]. Based on the spoke shape, several groups can be distinguished: non-recognizable spokes, stochastic spokes, diffusive spokes, triangular spokes, and round spokes [13]. It has been found that the transition from the well recognizable spokes to homogeneously distributed plasma in non-reactive HiPIMS is only observed for the target materials with the second ionisation potential higher than the first ionisation potential of argon (15.76 eV), and a self-sputter yield larger than 1 [14].

The spokes usually rotate in the E × B direction in the HiPIMS discharges [1, 5, 6] with velocities of about 10 km · s^{-1}, i.e., 10% of the electron drift velocity [1, 2, 5, 6, 15]. The spoke mode number is strongly dependent on the discharge current, working gas pressure, and magnetic field strength [9, 13, 16, 17]. Both, an increase [5, 13, 17, 18] as well as a decrease [9, 11, 13, 15, 16] in the spoke mode number were observed depending on the particular experimental setup.

For an in-depth insight of the spoke phenomena in HiPIMS, it is necessary to obtain extensive data of the plasma parameters inside the spoke, preferably by non-invasive diagnostic methods. This contribution shows the spatial-resolved optical emission spectroscopy (OES) of the spoke in HiPIMS discharge. The excitation temperature of Ti atoms was determined using Boltzmann plots.

2. Experimental setup

The experimental setup can be seen in figure 1. The pulses in the non-reactive HiPIMS discharge were 100 μs long with a repetition rate of 5 Hz. The 3-inch titanium target and argon as a working gas were utilised. The experiment was run at pressures: 0.4 Pa, 1.0 Pa and 1.6 Pa to investigate both triangular and round spokes [13].

Using the signals from the cylindrical probe and the fast photodiode the passing spoke was captured and its position was determined. Both signals were synchronised with the acquisition of the optical emission spectrum by the ICCD detector with the gate time of 100 ns. The emission spectra were acquired in a single-shot regime, i.e., for each spectrum exists one set of waveforms acquired at the same time from a single HiPIMS pulse.

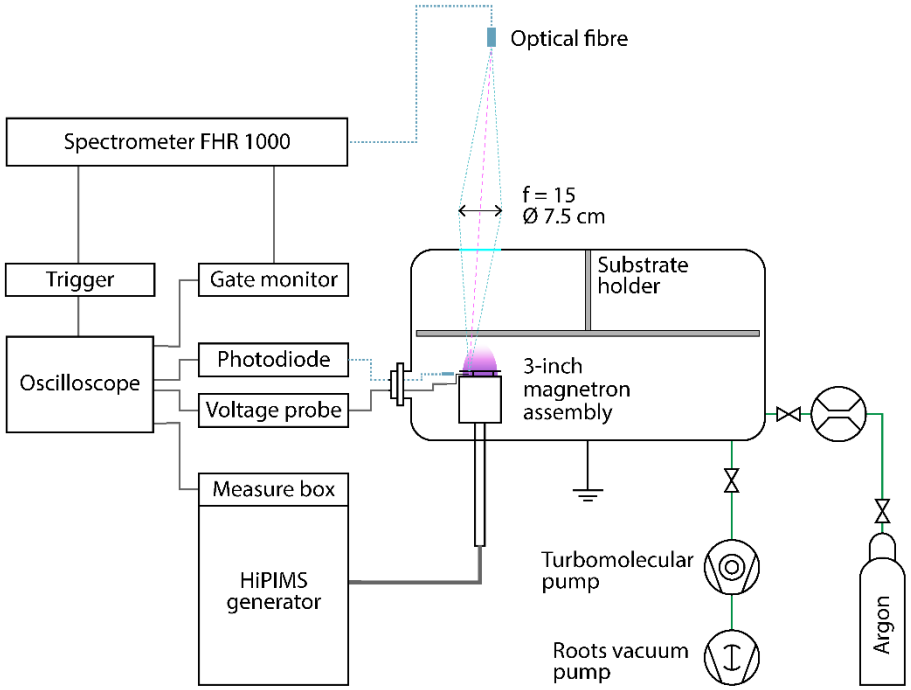

Fig. 1. Simplified scheme of the experimental setup.

3. Results

In figure 2, the intensities of the selected Ti I atom line (499.91 nm) are plotted for investigated working pressures and floating potential within the spoke. Taking into account various spoke lengths, the scale of the x-axis was normalized. Thus, 0 marks the head and 1 marks the tail of the spoke. The spoke was uniformly divided into 16 bins. Each point of the intensity evolutions in the graph in figure 2 is calculated as the mean of the integrated intensities of all spectra assigned to the appropriate bin by the time where the spectrum was captured. Characteristic evolution of titanium atom's spectral line intensities shows rather monotonous behaviour within the spoke for each measured working pressure. The floating potential of the spoke shown by the grey line in figure 2 remains stable in given discharge parameters.

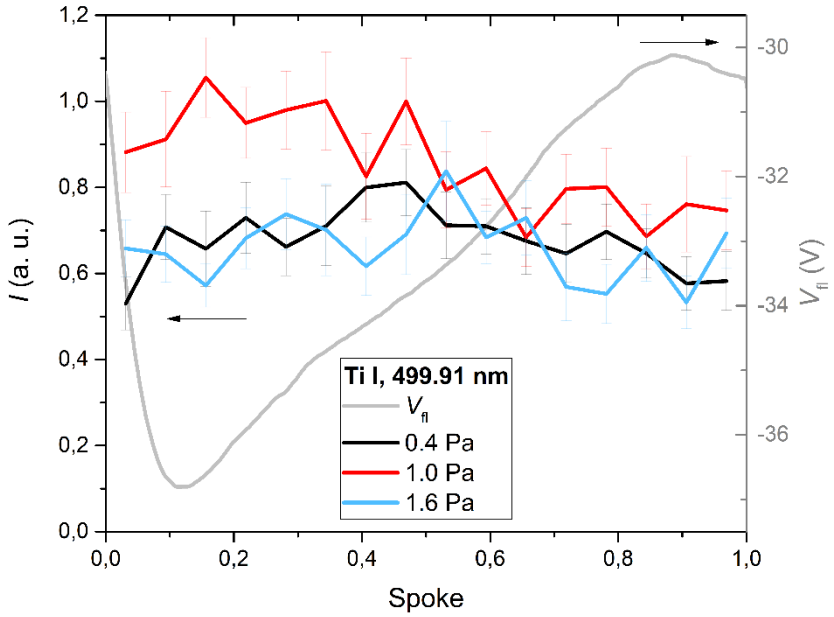

Fig. 2. The spatial-resolved evolution of Ti atom spectral line intensities within the spoke for pressures: 0.4 Pa, 1.0 Pa and 1.6 Pa in a reference to the floating potential within the spoke.

The excitation temperature of the Ti atoms was determined by the Boltzmann plot method. The typical one is shown in figure 3. The evolution of the excitation temperature within the spoke is shown in figure 4 for each investigated pressure. The excitation temperature is constant within the spoke in a margin of standard error for all used pressures. Despite the standard error of about 20%, the excitation temperature of the titanium atoms is approximately 8 000 K within the spoke for all measured pressures.

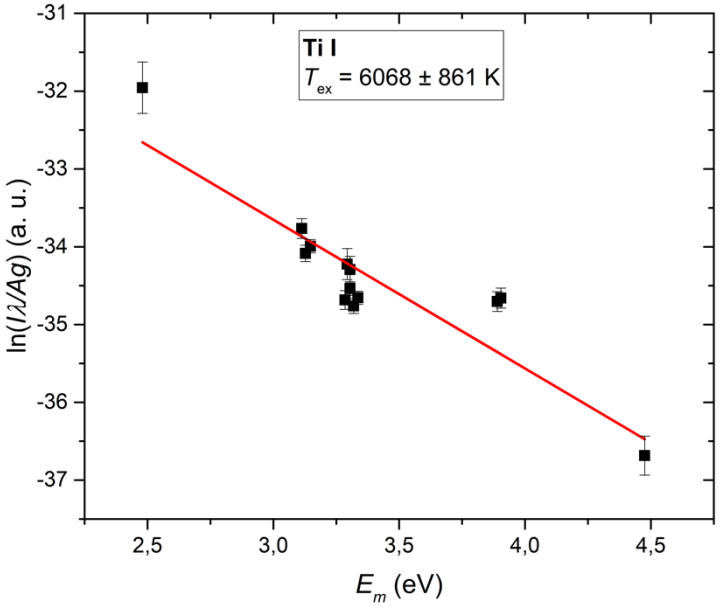

Fig. 3. Typical Boltzmann plot used for calculation of excitation temperature for the working pressure of 1.0 Pa.

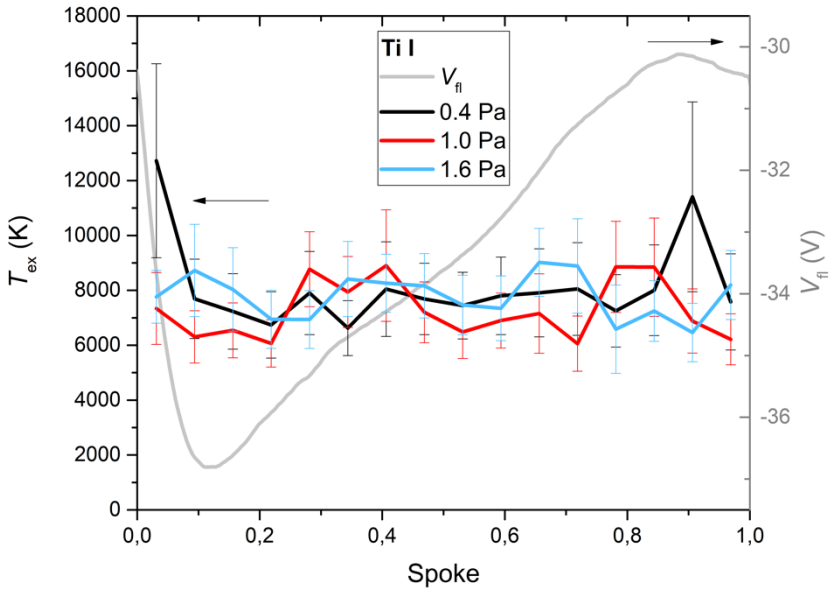

Fig. 4. The Ti I excitation temperature evolutions within the spoke for working pressures: 0.4 Pa, 1.0 Pa and 1.6 Pa in reference to the floating potential within the spoke.

4. Conclusion

The evolution of the titanium atom spectral line intensities and the floating potential within the spoke has been measured for working pressures: 0.4 Pa, 1.0 Pa and 1.6 Pa. The excitation temperature of the titanium atoms was determined by the Boltzmann plot method. The excitation temperature of the Ti atoms is approximately 8 000 K and remain constant within the spoke in a margin of standard error for all investigated pressures.

5. Acknowledgments

This research was supported by project LM2018097 funded by the Ministry of Education, Youth and Sports of the Czech Republic and project GA19-00579S funded by the Czech Science Foundation.

6. References

[1] Anders A, Ni P and Rauch A 2012 *J. Appl. Phys.* **111** 053304
[2] Anders A 2012 *Appl. Phys. Lett.* **100** 224104
[3] Anders A, Ni P and Andersson J 2014 *IEEE Trans. Plasma Sci.* **42** 2578
[4] Panjan M, Loquai S, Klemberg-Sapieha J E and Martinu L 2015 *Plasma Sources Sci. Technol.* **24** 065010
[5] Kozyrev A V, Sochugov N S, Oskomov K V, Zakharov A N and Odivanova A N 2011 *Plasma Phys. Rep.* **37** 667–73
[6] Ehiasarian A P, Hecimovic A, de los Arcos T, New R, Schulz- Von Der Gathen V, Böke M and Winter J 2012 *Appl. Phys. Lett.* **100** 114101
[7] Panjan M 2019 *J. Appl. Phys.* **125** 203303
[8] Hecimovic A, Böke M and Winter J 2014 *J. Phys. D: Appl. Phys.* **47** 102003
[9] de los Arcos T, Layes V, Gonzalvo Y A, Schulz-von der Gathen V, Hecimovic A and Winter J 2013 *J. Phys. D: Appl. Phys.* **46** 335201
[10] Poolcharuansin P, Estrin F L and Bradley J W 2015 *J. Appl. Phys.* **117** 163304
[11] Breilmann W, Eitrich A, Maszl C, Hecimovic A, Layes V, Benedikt J and von Keudell A 2015 *J. Phys. D: Appl. Phys.* **48** 295202
[12] Klein P, Lockwood Estrin F, Hnilica J, Vašina P and Bradley J W 2017 *J. Phys. D: Appl. Phys.* **50** 015209
[13] Hnilica J, Klein P, Šlapanská M, Fekete M and Vašina P 2018 *J. Phys. D: Appl. Phys.* **51** 095204
[14] Šlapanská M, Hecimovic A, Gudmundsson J T, Breilmann W, Vašina P and von Keudell A 2020 *J. Phys. D: Appl. Phys.* **53** 155201
[15] Winter J, Hecimovic A, de los Arcos T, Böke M and Schulz- Von Der Gathen V 2013 *J. Phys. D: Appl. Phys.* **46** 084007
[16] Hecimovic A, Schulz-von der Gathen V, Böke M, von Keudell A and Winter J 2015 *Plasma Sources Sci. Technol.* **24** 045005
[17] Klein P, Hnilica J, Zemánek M, Bradley J W and Vašina P 2019 *J. Phys. D: Appl. Phys.* **52** 125201
[18] Klein P, Hnilica J, Hubička Z, Čada M, Šlapanská M, Zemánek M and Vašina P 2017 *Plasma Sources Sci. Technol.* **26** 055015

SPECTROSCOPY OF ANTHRACENE IN HELIUM NANODROPLETS

Miriam Meyer[1], Paul Martini[1], Sergiy Krasnokutskiy[2], Paul Scheier[1]

[1]*Insitute for Ion Physics and Applied Physics, University of Innsbruck, Innsbruck, Austria*
[2]*Institute for Solid State Physics, University of Jena, Jena, Germany*
E-mail: miriam.meyer@uibk.ac.at

Absorption bands of anthracene cations (An^+) and hydrogenated An cations (AnH^+) have been measured in an ultracold weakly inter-acting helium (He) environment by means of mass spectrometry. Shifts of absorption band positions as a function of the number of attached messenger atoms or molecules can be deduced.

1. Introduction

Polycyclic aromatic hydrocarbons (PAHs) are promising candidates for being carriers of diffuse interstellar bands (DIBs) [1]. So far, more than 500 DIBs have been observed of which only five could unambiguously be assigned to C_{60}^+ [3]. Measuring absorption profiles of PAHs under astrophysically relevant conditions is therefore of great interest.

In this study An^+ and protonated An molecules (AnH^+) were isolated in ultracold helium nanodroplets (HNDs). In order to release the species of interest from the HNDs and make them accessible for mass spectrometry, the droplets were collided with a stainless steel surface. An^+ and AnH^+ ions with up to some tens of He atoms, respectively H_2 molecules as messenger species attached, were measured in a time-of-flight (TOF) mass spectrometer. Probing $AnHe_n^+$, respectively $AnH(H_2)_m^+$, with a pulsed tunable laser, absorption spectra were obtained by recording a decrease in the ion yield at certain masses (figures 1 and 2). This decrease is caused by He atoms or H_2 molecules boiling off after excitation with a laser photon.

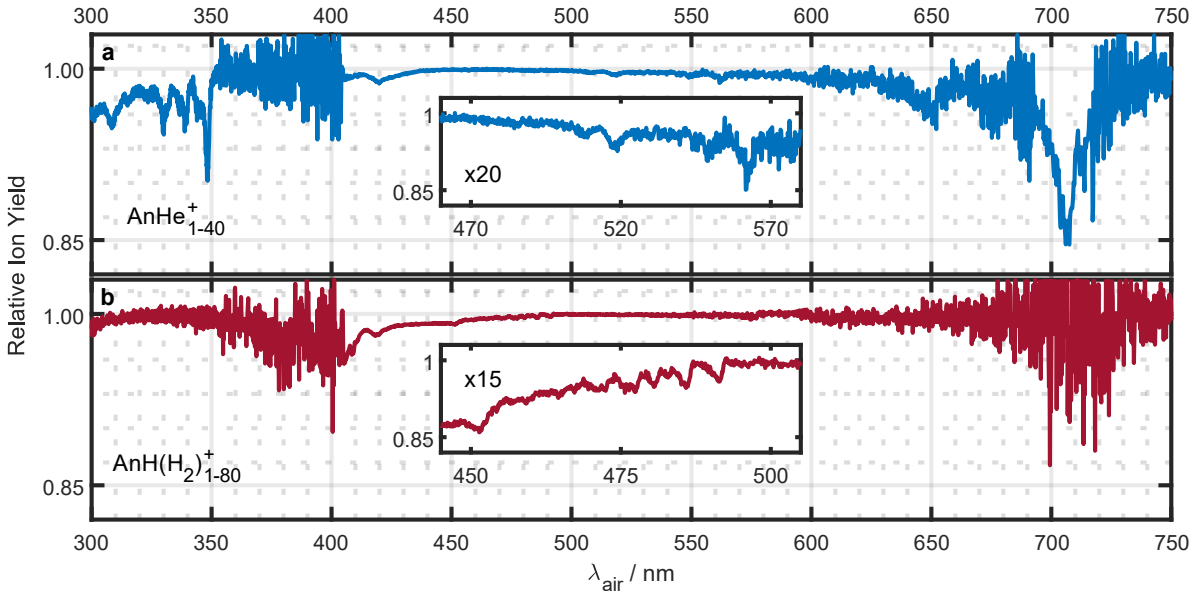

Fig. 1. Absorption spectra of He_n (a) and $(H_2)_m$ (b) tagged An^+ and AnH^+. The decrease of 40 (top), respectively 80 (bottom) mass channels was combined for a better signal-to-noise ratio, which, however, amounts to an increased width of the absorption bands.

2. Results

Several absorption bands were observed for He and H_2 tagged An^+ and AnH^+ (figure 1), which correspond well with previous measurements of An^+ in argon matrices [4] and AnH^+ in the gas phase

[5]. A shift of the absorption band position is expected from tagging species with messenger atoms or molecules [6]. This shift is small when the messenger is He or H_2 and can be deduced from our absorption spectra, as can be seen in figure 2.

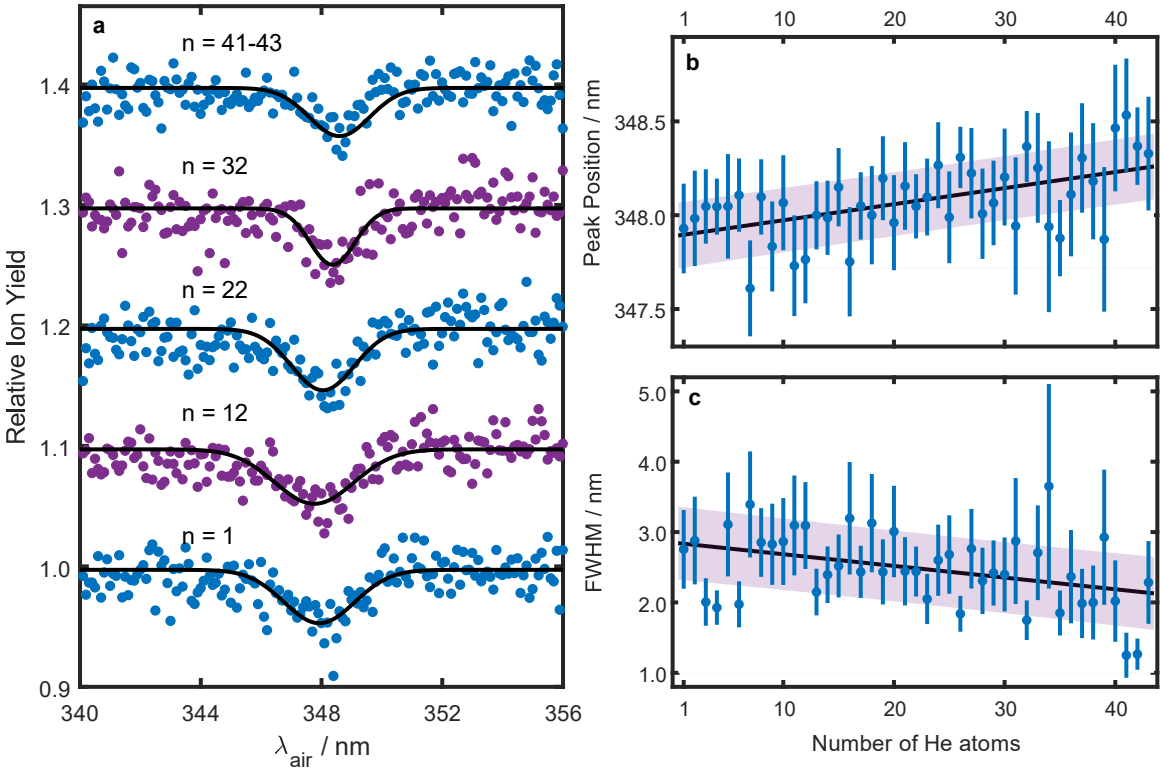

Fig. 2. Peak shift of the absorption band of An^+ at 348 nm as a function of the number of attached He atoms. (a) Band positions were determined by fitting gaussians to the decrease of the $AnHe_n^+$ signal. A selection of the relative ion yields at different mass channels with fitted curves is shown in (a). (b) The absorption band position shifts linearly up to about 40 attached He atoms, with about 0.01 nm/He atom. (c) The FWHM of the absorption band decreases linearly with an increasing number of attached He atoms.

3. References

[1] Salama, F., Galazutdinov, G. A., Krełowski, J., Allamandola, L. J., & Musaev, F. A. 1999 *The Astrophysical Journal*, *526*(1), 265.

[2] Fan, H., Hobbs, L. M., Dahlstrom, J. A., Welty, D. E., York, D. G., Rachford, B., ... & Zhao, G. 2019 *The Astrophysical Journal*, *878*(2), 151.

[3] Linnartz, H., Cami, J., Cordiner, M., Cox, N. L. J., Ehrenfreund, P., Foing, B., ... & Scheier, P. 2020 *Journal of Molecular Spectroscopy*, *367*, 111243.

[4] Szczepanski, J., Vala, M., Talbi, D., Parisel, O., & Ellinger, Y. 1993 *The Journal of chemical physics*, *98*(6), 4494-4511.

[5] Alata, I., Dedonder, C., Broquier, M., Marceca, E., & Jouvet, C. 2010 *Journal of the American Chemical Society*, *132*(49), 17483-17489.

[6] Holz, M., Campbell, E. K., Rice, C. A., & Maier, J. P. 2017 *Journal of Molecular Spectroscopy*, *332*, 22-25.

ELECTRIC FIELD MEASUREMENTS OF A KHZ DRIVEN ATMOSPHERIC PRESSURE PLASMA JET

Carla McDonnell[1], Steven White[1], Sinead Mannion[1], Tom A. Field[1], William G. Graham[1], David Riley[1]

[1]*Centre for Plasma Physics, School of Mathematics and Physics, Queen's University Belfast, University Road BT7 1NN, United Kingdom*
E-mail: cmcdonnell18@qub.ac.uk

This presentation focuses on the axial electric field strength in the plasma plume of a helium atmospheric pressure plasma jet (APPJ). A non-perturbing spectroscopic method based on the polarisation dependent Stark effect of the helium 492.2 nm line and its forbidden component was used for these measurements. This technique can be employed for a freely expanding plasma jet as well as plasma-surface interactions. For most application purposes of APPJs, the plasma jet will be interacting with a target of some sort of dielectric profile. Current research has shown the electric field to play a large role in the plasma-surface interaction. This work aims to provide a more detailed understanding of the plasma-surface interaction.

1. Plasma Jet Details

The plasma jet used in this study is similar to that of a dielectric barrier discharge (DBD). The plasma jet consists of two copper ring electrodes, each 5mm wide and 100μm thick, wrapped externally around a cylindrical quartz tube (inner diameter: 4mm outer diameter: 6mm) vertically orientated as depicted in figure 1. The centre of the powered electrode is fixed at a distance of 22.5mm from the exit nozzle of the tube and remains separated from the grounded electrode at a distance of 27.5mm. To ignite the plasma, a high voltage (1 – 12 kV) pulsed power supply (Haiden PHF-2K) with repetition rates in the 1 – 100kHz range are applied between the two electrodes and a helium gas mixture is passed through the tube. The applied voltage is measured using a Tekronix P6015A high voltage probe and two Pearson probes monitor the current in both the high voltage cable and grounded cable. The voltage pulse produced is attenuated by the probe by 1000x before being viewed via a GHz digital oscilloscope (Tektronix TDS5104). The current waveforms are also monitored by the same oscilloscope. For the work presented here, the typical voltage supplied was 6kV at a repetition frequency of 20kHz and a helium flow rate of 2 standard litres per minute, slm. The jet extends into open air at atmospheric pressure and room temperature.

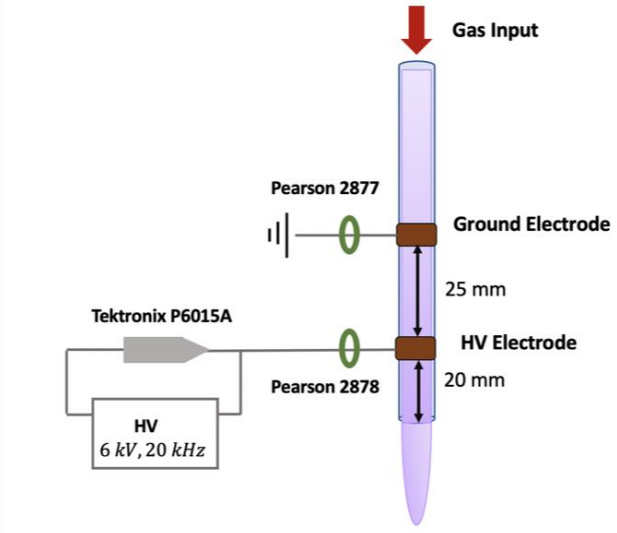

Fig. 1. Schematic of the plasma jet used in this work.

INFRARED-SPECTROMETRIC MONITORING OF THE GROWTH AND SURFACE TREATMENT OF NANOPARTICLES IN A LOW-PRESSURE PLASMA

Oguz Han Asnaz[1], Franko Greiner[1], Jan Benedikt[1]

[1]*IEAP, Kiel University, 24098 Kiel, Germany*
E-mail: asnaz@physik.uni-kiel.de

A capacitively coupled plasma is used for generating and confining carbon nanoparticles from acetylene (C_2H_2) for subsequent surface treatment with hydrogen and deuterium. The surface chemistry is then analyzed using fourier-transform infrared spectroscopy in a multi-pass setup for higher sensitivity.

Due to their unique physical, mechanical, electrical, and optical properties, nanoparticles have found a wide range of applications ranging from drug carriers in biomedicine over catalysts to batteries and solar cells in the last decades. In all of these, fine control over the particle's surface properties as well as the bulk crystallinity is required.

In this contribution, a capacitively couple plasma is used for generation, confinement, and treatment of carbon nanoparticles. Using a mixture of argon and acetylene (C_2H_2) at low plasma power, particles reach a size of about 500 nm after 90 seconds of growth. The charged particles are held in the electric field of the plasma sheath and can be confined easily for multiple hours. Afterwards, the particles are treated with hydrogen and deuterium to passivate their surface. Both the growth process and the particle treatment is monitored in-situ using Fourier-transform infrared spectroscopy (FTIR) over the course of 45 minutes. A multi-pass setup with 24 passes through the plasma chamber is used to maximize the absorption signal. This measurement allows insight into the chemical bonds on the particle surface as well as in the bulk material. Additionally, using the electrostatic particle extractor system (EPEX) created in our group [1], particle samples are extracted at multiple moments during the treatment for further SEM analysis with negligible disturbance of the plasma.

Fig. 1 shows the FTIR spectra of plasma-confined hydrocarbon nanoparticles during an etching experiment with D_2 gas admixture to the argon gas. Nanoparticle etching and the changes of the chemical groups can be observed. Additionally, the time evolution of the absorption lines is shown in Fig. 2. The same experiment has been repeated with H_2 and the differences as well as SEM images of the etched particles will be presented in the presentation.

In the future, surface modifications of silicon, metal, or metal-oxide nanoparticles generated in external plasma sources will be studied, which will allow further insight into the dynamics of surface oxidation, passivation, and thin-film deposition.

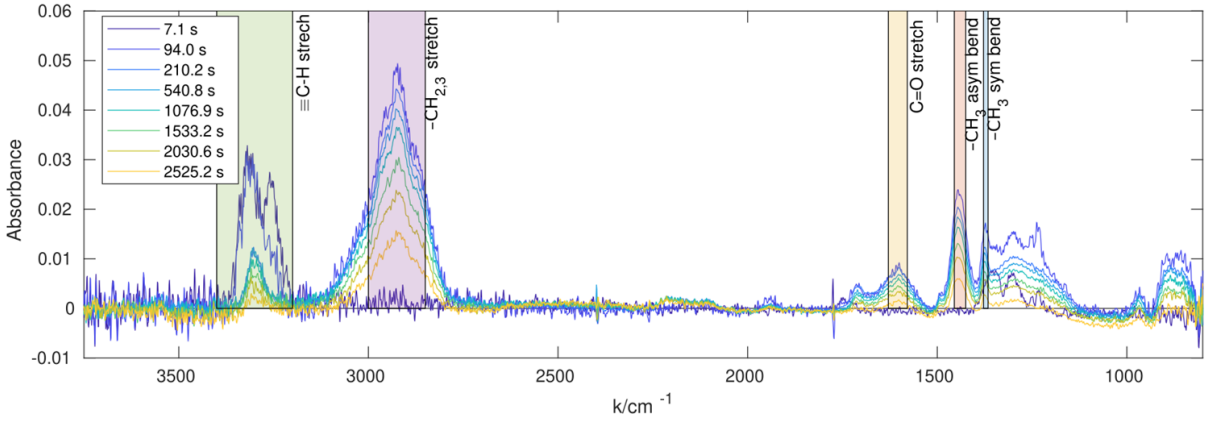

Fig. 1. Infrared absorption spectrum of a-C:H nanoparticles. The particles were generated by admixing acetylene for the first 90 seconds of the measurement. Starting at t = 210 s, deuterium was admixed to the plasma to initiate surface passivation. Regions of relevant absorption lines are labelled according to [2].

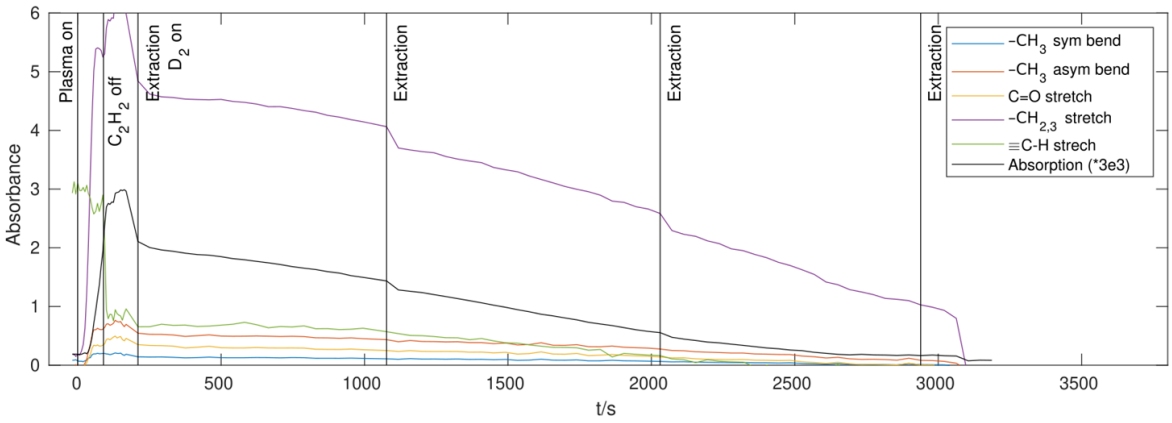

Fig. 2. Time evolution of the marked absorption lines from the spectra shown in Fig. 1. Additionally, the absorption coefficient from the Rayleigh fit is shown in black. The etching and subsequent size decrease of the particles can be seen in both the absorption coefficient and the general absorption intensities.

References

[1] M. Dworschak, O. Asnaz, and F. Greiner (2020). *Plasma Sources Sci. Technol.*, (submitted).
[2] E. Kovačević, I. Stefanović, et al. (2003). *Journal of Applied Physics*, 93(5), 2924–2930.